ESTIMATES OF EFFECTS OF RESIDUAL ACCELERATION ON USML-1 EXPERIMENTS

by

Dr. Robert J. Naumann

Professor, Materials Science

University of Alabama in Huntsville

Final Report

NAS8-36955 D. O. 105

ESTIMATES OF EFFECTS OF RESIDUAL ACCELERATION ON USML-1 EXPERIMENTS

by

Dr. Robert J. Naumann

Professor, Materials Science

University of Alabama in Huntsville

Final Report

NAS8-36955 D. O. 105

PREFACE

The purpose of this study effort was to develop analytical models to describe the effects of residual accelerations on the experiments to be carried on the first U. S. Microgravity Lab mission (USML-1) and to test the accuracy of these models by comparing the pre-flight predicted effects with the post-flight measured effects. After surveying the experiments to be performed on USML-1, it became evident that the anticipated residual accelerations during the USML-1 mission were well below the threshold for most of the primary experiments and all of the secondary (Glovebox) experiments and that the only set of experiments that could provide quantifiable effects, and thus provide a definitive test of the analytical models, were the three melt growth experiments using the Bridgman-Stockbarger type Crystal Growth Furnace (CGF). This class of experiments is by far the most sensitive to low level quasi-steady accelerations that are unavoidable on space craft operating in low earth orbit. Because of this, they have been the drivers for the acceleration requirements imposed on the Space Station. Therefore, it is appropriate that the models on which these requirements are based are tested experimentally. Also, since solidification proceeds directionally over a long period of time, the solidified ingot provides a more or less continuous record of the effects from acceleration disturbances.

The use of approximate analytical models is advantageous because of the insight they provide into the interaction of the many parameters involved in the redistribution of solute during the process. Numerical models are generally more accurate since they do not make as many simplifying assumptions, but they provide an answer for only a single point in parameter space and do not provide any indication of how the result might vary if one or more of the many input conditions were varied. Approximate analytical models provide scaling relationships that can cover a broad range of parameter space. If these scaling laws are verified by numerical computations at selected points to assure that the approximations used are still valid, they provide a very powerful tool for assessing the effects of residual accelerations on a variety of experiments without having to resort to a large number of numerical computations, and can provide a useful guide for experimenters wishing to minimize the unwanted effects from the residual accelerations.

The first section of this report is devoted to the development of analytical models to describe the buoyancy-driven flows in closed containers with a variety of shapes and orientations relative to the acceleration vector. Primary emphasis was given to fully developed flows from quasi-steady accelerations, but methods for estimating the response times were also developed to extend these models to describe the effects of transient and periodic accelerations. A powerful integral theorem was derived which enabled the extension of simple one-dimensional models, for which closed-form analytical solutions exist, to two-dimensional models which have no known analytical solutions. The range of the two-dimensional models covers the case of low Rayleigh numbers, where the density field is decoupled from flow field, to higher Rayleigh numbers where such coupling must be considered. This allows the models to be extended nearly to unit gravity for the case of low Pr fluids, or to be applied to high Pr fluids as well

as to solutal-driven convection in a reduced gravity environment. The non-linear inertial terms were ignored, so the models are limited to flows where these terms are negligible. However, this is not a serious restriction for the purposes of this study. The effects of stabilizing and destabilizing density gradients were also considered along with the effects of applying magnetic fields to help suppress unwanted flows. These various models were tested extensively against numerical computations and were found to be accurate to within a factor of 2 and in most case accurate to within a few percent.

Since USML-1 was to be a low-gravity emphasis mission, the orientation to the vehicle was chosen to orient the quasi-steady residual acceleration vector, primarily from atmospheric drag, along the furnace axis. Therefore, it was expected that the primary effect to be observed would be the radial segregation resulting from the radial thermal gradients in the furnace experiments. Therefore, the second section is devoted to modeling axisymmetrical flows and their effect on solute redistribution for a Bridgman growth system with low-level steady and time-dependent axial accelerations. This was accomplished by first using an approximate method to obtain the flow field and than using a perturbation method to get a first order correction to the concentration field. This method is applicable as long as the perturbation is small compared to the zero-order field. Again the results were tested against numerical calculations and were found to be reasonably accurate within the limits of the approximations used.

As it turned out, there were some unanticipated accelerations during the mission that caused the acceleration vector at the furnace location to be more transverse than axial. This prompted an additional, more detailed study of the flows and their effects from transverse accelerations which is developed in Section 3. Since the Bridgman type experiments generally have a density profile that falls exponentially from the growth interface, emphasis was given to modeling the flows resulting from this type of density profile rather than using the simpler assumption of a linear profile which was the basis of most of the models developed in Section 1. Also, to calculate the radial segregation at the growth interface, it is necessary to have an accurate description of the axial velocity profile. This was obtained using a novel approximation technique for the solution of the biharmonic equation that describes the stream function. A first order perturbation correction to the concentration field was then obtained as before. Again the results were verified by extensive comparison to numerical computations.

Section 4 contains the pre-flight predictions of the expected effects of the anticipated accelerations. It should be remembered that since at the time these predictions were made it was expected that axial accelerations would be the dominant disturbance and that the study in Section 3 had not been undertaken. Therefore, these estimated are base primarily on the results of Section 2 and some crude estimates of the effects of transverse accelerations based on flow models in Section 1.

Section 5 contains more accurate after-the fact predictions of the effects of transverse accelerations using the results developed in Section 3. In comparing

the two, it may be seen that the crude estimates in Section 4 were well within an order of magnitude of the more refined estimates. Unfortunately, experimental difficulties with the various experiments caused by the unanticipated transverse accelerations did not permit a definitive comparison of the models with experimental data. One of the lessons learned, however, was the extreme sensitivity of this type of experiment to quasi-steady transverse accelerations; especially for non-dilute alloy-type systems with high Schmidt numbers. Several possible methods such as density gradient stabilization and magnetic suppression were explored to help mitigate this sensitivity.

TABLE OF CONTENTS

SECTION 1

METHODS FOR ESTIMATING BUOYANCY-DRIVEN FLOWS IN CLOSED CAVITIES

1.1 INTRODUCTION

In many cases, it is desirable to be able to estimate the magnitude of natural or buoyancy-driven convective flows in a crystal growth or other solidification process in order to determine if heat and mass transport are dominated by convective or diffusive transport, to determine if flows will be steady or time-varying, or to estimate the effectiveness of the strategy for controlling unwanted flows, whether by using strong magnetic fields or by conducting the experiment in reduced gravity. Such flows can, of course be computed by solving the full set of coupled Navier-Stokes equations in 2- or 3 dimensions, but such computations require a large computer, are expensive, and often give far more information than is really needed. Furthermore, such computations only give the solution to a specific problem and do not provide the insight necessary to judge the potential effects or varying the several parameters that determine the flow field. Therefore, in order to develop a process, it is useful to have simple analytical models that are admittedly crude, but none-the-less can provide reasonably accurate predictions of the flows to be expected.

Ostrach [1] pointed out the usefulness of applying scaling analysis to estimate flows in potential experiments to at least determine if the desired effects could be realized. Using this technique, he obtained

$$\hat{v} \approx Gr(\nu/L), \qquad Gr \le 1 \text{ and } Pr \le 1; \tag{1.1}$$

$$\hat{v} \approx Gr^{1/2}(\nu/L), \qquad Gr > 1 \text{ and } Pr \le 1; \tag{1.2}$$

$$\hat{v} \approx (Gr/Pr)^{1/2}(\nu/L), \qquad Gr > 1 \text{ and } Pr > 1; \tag{1.3}$$

where $\hat{v}$ is the maximum velocity, Gr is the Grashof number ($g\,\Delta\rho/\rho\,L^3/\nu^2$), Pr is the Prandtl number (ν/κ), ν is the kinematic viscosity, κ is the thermal diffusivity, and L is some characteristic length. One of the difficulties in using these scaling relationships is determining what length scale to use. For example, should L be the length, the width, the radius, the diffusion length, etc.? Since the Grashof number depends on the cube of the length scale, this choice can make a crucial difference.

Langbein and Tiby [2] also proposed a simple criteria based on the same type of analysis that predicted what g-levels as a function of frequency would be required for different classes of proposed microgravity experiments. For an experiment in which heat transport is of primary interest, they estimate the relative perturbation due to accelerations is

$$\frac{\delta T}{T} = \frac{\hat{g}\,\beta\,\Delta T}{L\left[\omega^2 + (\nu/L)^2\right]^{1/2}\left[\omega^2 + (\kappa/L)^2\right]^{1/2}} \tag{1.4}$$

and for experiments where mass transport was of primary interest, the relative perturbation in composition is

$$\frac{\delta C}{C} = \frac{\hat{g}\,(\Delta\rho/\rho)}{L\left[\omega^2 + (\nu/L)^2\right]^{1/2}\left[\omega^2 + (D/L)^2\right]^{1/2}} \tag{1.5}$$

where $\hat{g}$ is the amplitude of the acceleration, $\beta\,\Delta T$ and $\Delta\rho/\rho$ are the maximum relative density changes and D is the diffusion coefficient. Note that for $\omega \to 0$, these expressions reduce to

$$\frac{\delta T}{T} = \frac{\hat{g}\,\beta\,\Delta T L^3}{\nu\kappa} = Ra_{thermal} \quad \text{and} \quad \frac{\delta C}{C} = \frac{\hat{g}\,(\Delta\rho/\rho)L^3}{\nu D} = Ra_{solutaol}$$

which are the thermal and solutal Rayleigh numbers, respectively.

Unfortunately, because of the difficulty in choosing the proper length scale, and because of the crudity of the scaling analysis, these models tended to over-predict the effects of residual accelerations, giving rise to unreasonable requirements for the acceleration environment as will be shown.

Clearly, a better method must be found for predicting effects of steady, transient, and periodic accelerations on various processes involving fluids. In this paper, a powerful integral theorem is developed which, through the use of simple analysis, can predict the flows resulting from steady and time-varying accelerations to well within a factor of 2, and in many cases to within a few percent.

1.2 DERIVATION OF THE INTEGRAL THEOREM

The equation of motion for an incompressible fluid can be written in the form:

$$\rho\frac{\partial \mathbf{v}}{\partial t} = \rho\,\mathbf{v}\times(\nabla\times\mathbf{v}) - \nabla\left(p + \frac{\rho v^2}{2}\right) + \mu\,\nabla^2\mathbf{v} + \rho\,\mathbf{g}. \tag{1.6}$$

Consider the flow around a streamline. Note that

$$\oint \mathbf{v}\times(\nabla\times\mathbf{v})\bullet d\mathbf{s} = \oint \mathbf{v}\times\omega\bullet d\mathbf{s} = 0$$

since the vorticity $\omega = \nabla\times\mathbf{v}$ is always perpendicular to $\mathbf{v}$, hence $\nabla\times\omega$ will always be perpendicular to $d\mathbf{s}$ if $d\mathbf{s}$ is an element of length on a streamline. Since the pressure term $(p + \rho v^2/2)$ is a single valued scalar function,

$$\oint \nabla\left(p+\frac{\rho v^2}{2}\right)\bullet \mathbf{ds} = 0$$

because the integrand is an exact differential. Therefore, integrating the equation of motion around a streamline eliminates the pressure and the inertial terms and yields a simplified expression [3]

$$\oint \rho\frac{\partial \mathbf{v}}{\partial t}\bullet \mathbf{ds} = \oint \mu\nabla^2\mathbf{v}\bullet \mathbf{ds} + \oint \rho\mathbf{g}\bullet \mathbf{ds}, \quad \text{Q.E.D.} \tag{1.7}$$

Extensive use will be made of this powerful theorem in the developing the various approximation formula for estimating maximum flows.

1.3 ONE-DIMENSIONAL MODELS

For cases in which the aspect ratio is much greater than one, it is possible to employ a one-dimensional model to estimate the flow field. Such models have the advantage of being simple enough to yield a closed form solution.

1.3.1 Vertical Slot

Consider, for example, the case of a fluid in a vertical differentially heated slot whose width is 2a and L >> a. Using the Boussinesq approximation, the density can be written as

$$\rho(x) = \rho_0\left(1-\beta\frac{\Delta T}{2}\frac{x}{a}\right)$$

where $\beta = (1/\rho_0)\partial\rho/\partial T$ and x is the distance from the center line.

Choosing a stream line that goes down at -x and up at x, integrating, and dividing through by ρ_0, Eq. (1.7) can be written as

$$\frac{\partial v(x)}{\partial t}(2L) = \nu\frac{\partial^2 v(x)}{\partial x^2}(2L) + \frac{g\beta\Delta T}{2}\frac{x}{a}(2L) \tag{1.8}$$

where g is taken as positive downward.

The boundary conditions are v(± a) = 0 (no-slip at the walls) and no net flow. Let ξ = x/a. The steady state solution is

$$\bar{v}(x) = \frac{g\beta\Delta T a^2}{12\nu}(\xi - \xi^3) = \frac{Gr\,\nu}{48\,a}(\xi - \xi^3);$$

$$\text{where} \quad Gr = \frac{g\beta\Delta T W^3}{\nu^2}; \quad W = 2a \tag{1.9}$$

which is the well known solution to the problem of free convection in a differentially heated vertical slot [4]. The maximum velocity $\hat{v}$ occurs at $\xi = 1/\sqrt{3}$ and is

$$\hat{v} = \frac{g\beta\Delta T a^2}{18\sqrt{3}\,\nu} = \frac{Gr}{72\sqrt{3}}\frac{\nu}{W}. \tag{1.10}$$

Note that this has the same functional form as the scaling analysis result, Eq. (1.1), but the maximum flow velocity is almost 2 orders of magnitude less than predicted by Eq. (1.1) if W is chosen as the length scale. Also note that there is no restriction on Gr or Pr in this model because there is no mechanism in this one-dimensional model for heat to be transported other than by conduction. The presence of ends would of course cause the flow to turn and allow for the transport of heat by convection, but this will be discussed in the next section. Also it is tacitly assumed by taking the streamline parallel to the walls that the Reynolds number $Re = \hat{v}L/\nu$ is sufficiently small so that the flow remains laminar.

The transient solution to Eq. (1.8) can be obtained by writing $v(x,t) = \bar{v}(x) + w(x,t)$ where w(x,t) satisfies

$$\frac{\partial w(x,t)}{\partial t} = \nu\frac{\partial^2 w(x,t)}{\partial x^2}. \tag{1.12}$$

This has a general solution given by

$$w(x,t) = \sum_n (A_n \sin(b_n\xi) + B_n \cos(b_n\xi))\exp(t/\tau_n)$$

where $\frac{1}{\tau_n} = b_n^2\frac{\nu}{a^2}$.

If the initial conditions are g = 0 and v(x,t) = 0 for t < 0 and g is "switched on" at t = 0, the $b_n = n\,\pi$ to match the no-slip boundary conditions and the Fourier coefficients are evaluated to give the complete solution

$$v(\xi,t) = \frac{g\beta\Delta T a^2}{12\nu}\left[(\xi - \xi^3) - \sum_n \frac{12(-1)^n}{n^3\pi^3}\sin(n\pi\xi)\exp(t/\tau_n)\right]. \tag{1.13}$$

The evolution of the velocity build-up is shown in Fig. 1.1. Note that the initial disturbance originates near the walls and the peak velocity moves toward the equilibrium position ($\xi = 1/\sqrt{3}$) as time progresses.

A simpler approximate solution for $\hat{v}(t)$ may be obtained by integrating along the streamline corresponding to the steady state value of $\hat{v}$, i. e., $\xi = \pm 1/\sqrt{3}$. Eq. (1.8) can then be approximated by

$$\frac{d\hat{v}}{dt} = -\nu\frac{\hat{v}}{\delta^2} + \frac{g\beta\Delta T}{2}\frac{1}{\sqrt{3}} \tag{1.14}$$

where δ is the width of the momentum boundary layer and the negative sign was chosen since the viscous drag opposes the acceleration. The solution to Eq. (1.14) has the form

$$\hat{v}(t) = \hat{v}(\infty)\left(1 - e^{-t/\tau}\right) \tag{1.15}$$

where $\tau = \delta^2/\nu$ and $\hat{v}(\infty) = \dfrac{g\beta\Delta T\delta^2}{2\sqrt{3}\,\nu}$.

Since for large t, the $\hat{v}(t)$ must approach the steady state value given by Eq.(1.10), δ^2 can be identified as $a^2/9$ and the approximate solution becomes

$$\hat{v}(t) = \frac{g\beta\Delta T a^2}{18\sqrt{3}\,\nu}\left(1 - e^{-t/\tau}\right). \tag{1.16}$$

Note that the time constant $\tau = \delta^2/\nu = a^2/9\nu$. is very close to the time constant $a^2/\pi^2\nu$ of the leading term in the Fourier expansion indicated by Eq. (1.13). It should be remembered that this is an approximate solution because we assumed the maximum velocity was along the streamline corresponding to $\xi = \pm 1/\sqrt{3}$, whereas in reality, the maximum velocity occurs at different places along the x-axis as was seen in Fig. 1.1. However, this discrepancy makes little difference in the buildup of the transient as may be seen in Fig. 1.2.

A closed form solution for the response of this system to periodic accelerations is also possible. Assume $g(t) = \tilde{g}e^{i\omega t}$ and $v(x,t) = \tilde{v}(x)e^{i\omega t} = \sum_n A_n \sin(n\pi\xi)e^{i\omega t}$. Putting these expressions into Eq. (1.8),

$$\sum_n \left(i\omega + \frac{n^2\pi^2\nu}{a^2}\right)A_n \sin(n\pi\xi) = \frac{\tilde{g}\beta\Delta T}{2}\xi.$$

The Fourier coefficients A_n are extracted in the usual manner which yields

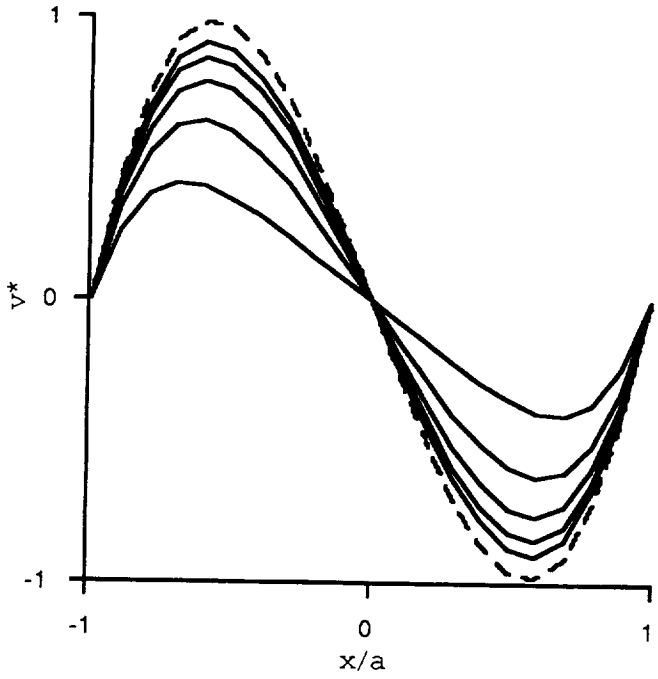

Fig. 1.1 Velocity build-up as function of time for vertical slot after g is "switched on". Curves correspond to $t^* = 0.05, 0.1, 0.15, 0.2,....$ where $t^* = t\,\nu\,/a^2$. The dashed curve corresponds to the steady state solution. Note that the velocity maxima is shifted slightly toward the edges at small values of t^*.

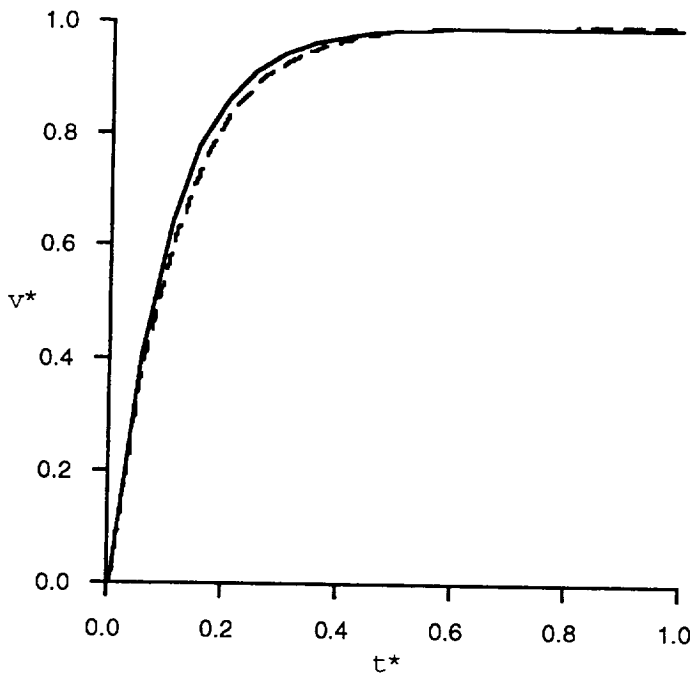

Fig. 1.2 Plot of $\hat{v}^* = \hat{v}(t^*)/\hat{v}(\infty)$ vs. $t^* = t\,\nu\,/\,a^2$. The solid line is the exact solution, Eq. (1.13), and the dashed line is the approximate solution, Eq. (1.16).

$$\tilde{v}(x) = -\frac{\tilde{g}\beta\Delta T a^2}{\nu}\sum_n \frac{(-1)^n}{n\pi\left(i\Omega + n^2\pi^2\right)}\sin(n\pi\xi) \qquad (1.17)$$

where the dimensionless frequency Ω is $\omega\, a^2 / \nu$. For $\Omega = 0$, this series reduces to the series in Eq. (1.13) with t = 0, which represents the steady state solution. Comparing the amplitude of the leading term in this series with the corresponding term in the Langbein - Tiby formula (Eq. (1.4)), note that in this expression the velocity amplitude does not diminish until ω is comparable with $\pi^2\,\nu / a^2$, whereas in the Langbein -Tiby model, this occurs at frequencies an order of magnitude or more less (depending on the choice of L). In other words, the fluid responds to disturbances much more rapidly than predicted by the Langbein - Tiby model. This is compensated somewhat because the Langbein-Tiby model over-predicts the steady state response.

Again a simplified approximate solution can be obtained for this system. Choosing the stream line at $\xi = \pm 1/\sqrt{3}$ where the steady state velocity amplitude is maximum as the path of integration, Eq. (1.13) can be written in terms of maximum velocity amplitude as

$$\frac{d\tilde{v}}{dt} = -\nu\frac{\tilde{v}}{\delta^2} + \frac{\tilde{g}\beta\Delta T}{2}\frac{1}{\sqrt{3}}$$

which, after the transient dies out, has a solution given by

$$\tilde{v} = \frac{\tilde{g}\beta\Delta T\delta^2}{2\sqrt{3}\,\nu}\frac{1}{\left(i\omega\delta^2/\nu + 1\right)}.$$

Requiring that this reduce to the steady state solution (Eq. (1.10)) as $\omega \to 0$, we identify $\delta^2 = a^2 / 9$ as before, and finally

$$\tilde{v} = \frac{\tilde{g}\beta\Delta T a^2}{2\sqrt{3}\,\nu}\frac{1}{\left(i\Omega + 9\right)}. \qquad (1.18)$$

Comparing this to the leading term of Eq. (1.17), they are seen to numerically very similar. Figure 1.3 compares these two expressions. The slight deviation at the higher frequencies results from the fact that the approximate calculation assumed the maximum velocity always occurs at $\xi = 1/\sqrt{3}$, which we see from Fig. 1.4 is not the case at the higher frequencies. The velocity amplitude obtained from the Langbein -Tiby model is also shown for comparison with L taken as 2 a. As discussed previously, this model seriously over-estimated the steady state velocity, and under-estimates the response time which can be seen in the figure.

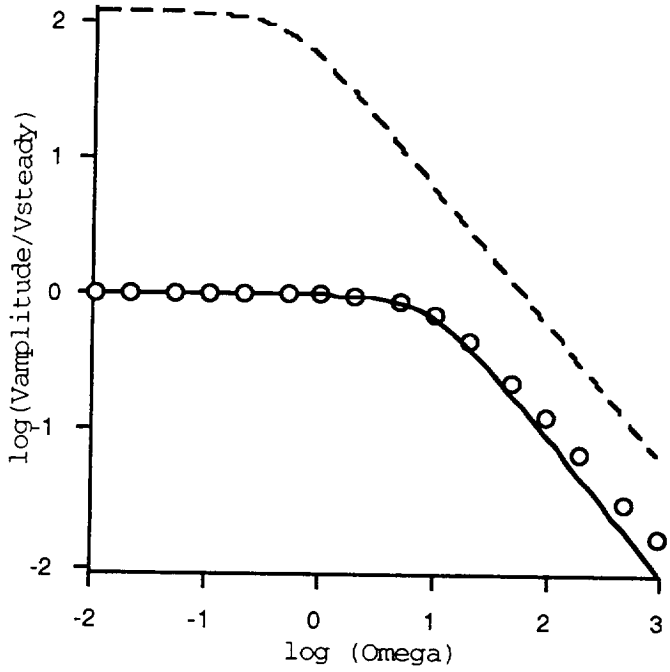

Fig. 1.3 Log-log plot of the ratio of maximum velocity amplitude to steady state velocity vs. dimensionless frequency $\Omega = \omega a^2 / n$ for fluid in a vertical differentially heated slot. Circles represent the exact solution (Eq. (1.17)); the solid line the approximate solution (Eq.(1.18)), and the dashed line the prediction from the Langbein - Tiby model.

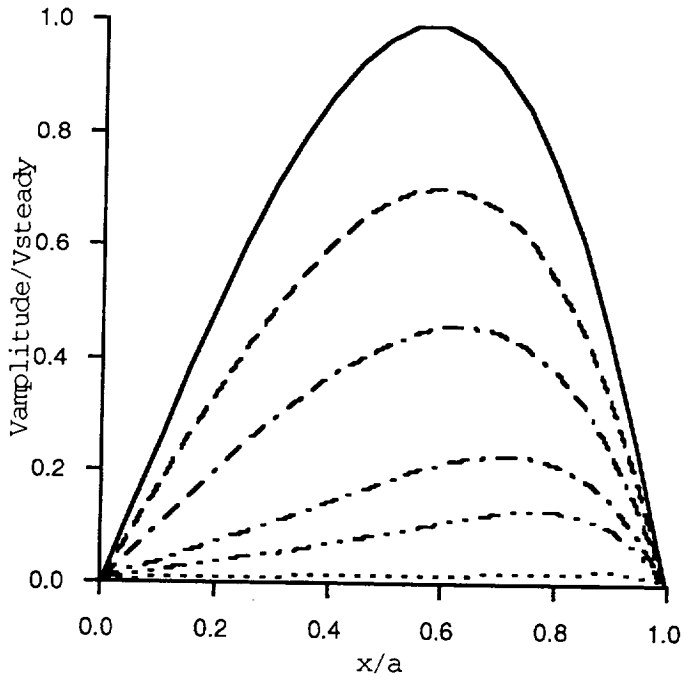

Fig. 1.4 Velocity amplitude scaled by steady state velocity as a function of the dimensionless frequency Ω for the case of a vertical differentially heated slot. Value for Ω from the top down are 0, 10, 20,50,100,1000.

1.3.2 Horizontal Slot

Next consider the flow in a long horizontal slot with length L and width W = 2 a that is differentially heated at the end walls. A linear thermal gradient is assumed so that the density function may be written

$$\rho(x) = \rho_0(1-\beta\Delta T x/L).$$

This, of course, assumes the convective flows do not transport sufficient heat to disturb the linear gradient. The criteria for this will be discussed later.

Since L>>a, the viscous drag contributions from the end walls can be ignored. Choosing an integration path along $\pm$ y and proceeding as before, Eq. (1.7) can be written as,

$$\frac{\partial u(y)}{\partial t}(2L) = \nu\frac{\partial^2 u(y)}{\partial y^2}(2L) + g\beta\Delta T(2y)\,.$$

Using the previous boundary conditions (no slip a the walls and no net flow), the second order ordinary differential equation for u has the steady state solution

$$\bar{u}(y) = \frac{g\beta\Delta T a^3}{6\nu L}(\eta-\eta^3) \text{ where } \eta = \frac{y}{a}.$$

Again $\hat{u}$ occurs when $\eta = 1/\sqrt{3}$, which gives

$$\hat{u} = \frac{g\beta\Delta T a^3}{9\sqrt{3}\,\nu L} = \frac{Gr}{72\sqrt{3}}\left(\frac{\nu}{L}\right)\,. \tag{1.19}$$

This is similar to the result for the vertical slot except ν/W is replaced by ν/L Unlike the vertical slot, there is a mechanism whereby heat is transferred in a one-dimensional model for the horizontal slot and the above formulation is valid only so long as this transport does not significantly affect the isotherms. Otherwise the assumption that the density field is independent of the flow field is no longer valid.

The transport of heat can be characterized by the thermal Peclet number defined as

$$Pe_{Thermal} = \frac{\hat{u}L}{\kappa} \tag{1.20}$$

which may be thought of as the ratio of heat transported by convection to heat transferred by conduction. For the assumption that the temperature field is

undisturbed by the flow to be valid, the $Pe_{Thermal} << 1$. Putting Eq. (1.19) into this definition, we have

$$Pe_{Thermal} = \frac{GrPr}{72\sqrt{3}} = \frac{Ra_{Thermal}}{72\sqrt{3}}$$

where the Gr and Ra are defined in terms of the thermal gradient. Therefore, Eq. (1.19) is restricted to cases in which

$$GrPr = \frac{g\beta\Delta T W^3}{\nu\kappa} << O(10^2). \qquad (1.21)$$

(A similar restriction applies to a finite vertical slot except that $Pe_{Thermal}$ would be given by $Pe_{Thermal} = \hat{u}W/\kappa$. Since $\hat{u}$ is not found in the one-dimensional model for the vertical slot, the discussion on limits of applicability for this case must be deferred to the next section.)

Examining the Langbein-Tiby model for temperature perturbations due to steady state convective flows, Eq. (1.4), it may be seen that, except for the numerical factor, the $\delta T/T$ corresponds to the thermal Peclet number if the L is taken as the width (or smallest dimension) of the system.

Because of the similarity of the equations governing the flows in the horizontal and vertical systems, the response time of fluid in a horizontal slot will be the same as for the vertical slot. Therefore, Eq. (1.13), (1.15), (1.17), and (1.18) will apply to the case of a horizontal slot if the driving term is multiplied by W/L.

1.4 TWO DIMENSIONAL CONFIGURATIONS

Dressler [5] considered the flow in a vertical circular cell with a linear horizontal temperature distribution and obtained a transient and steady state solution in the that is valid for small Rayleigh numbers. Assuming v(r,0) = 0 for all r, his solution is given by

$$v_\theta(r,t) = \frac{g\beta\Delta T a^2}{32\,\nu}\left\{(\zeta-\zeta^3)+16\sum_{n=1}^{\infty}\frac{J_1(\lambda_n\zeta)}{\lambda_n^3 J_0(\lambda_n)}\exp\left(-\lambda_n^2\frac{\nu}{a^2}t\right)\right\} \qquad (1.20)$$

where λ_n are the zeros of J_1 and $\zeta = r/a$.

The dominant, or most persistent term, in the series is the n=1 term which has a time constant given by $a^2/\lambda_1^2\nu$. Since $\lambda_1 = 3.8317$, this time constant is 0.0681 a^2/ν.

This result can easily be derived using the integral condition stated in Eq.(1.7). For steady state the left hand side is zero. Assuming small enough Ra such that

the temperature field is not disturbed by the flow, the streamlines will be concentric circles about the origin. The viscous drag term becomes

$$\mu \oint \nabla^2 \mathbf{v} \bullet d\mathbf{s} = \mu \left(v'' + \frac{v'}{r} - \frac{v}{r^2} \right) 2\pi r$$

where the primes denote partial differentiation with respect to r.

Writing $\mathbf{g} \bullet d\mathbf{s} = g \cos\theta \, r \, d\theta$ and the density function as

$$\rho(r,\theta) = \rho_0 \left(1 - \beta \frac{\Delta T}{2} \frac{r}{a} \cos\theta \right)$$

the buoyancy term becomes

$$\oint \rho \, g \bullet d\mathbf{s} = g \int_0^{2\pi} \left(\rho_0 \, r \cos\theta - \beta \frac{\Delta T}{2} \frac{r^2}{a} \cos^2\theta \right) d\theta = -\frac{\pi g \beta \Delta T \, r^2}{2a}.$$

Putting these two integrals into Eq. (1.7), the differential equation for the velocity is

$$\frac{1}{\nu} \frac{\partial v_\theta}{\partial t} = v_\theta'' + \frac{v_\theta'}{r} - \frac{v_\theta}{r^2} - \frac{g \beta \Delta T}{4 \nu} \frac{r}{a} \qquad (1.21)$$

where primes represent partial differentiation with respect to r. The boundary conditions are "no slip" at the walls and antisymmetry about r = 0. Letting $\zeta = r/a$, the steady state solution can be written

$$\bar{v}_\theta(r) = \frac{g \beta \Delta T a^2}{32 \nu} (\zeta - \zeta^3).$$

which is identical to Dressler's steady state result. The maximum steady velocity occurs at $\zeta = 1/3^{1/2}$, which becomes

$$\hat{v}_\theta = \frac{g \beta \Delta T a^2}{48\sqrt{3} \, \nu} = \frac{Gr}{192\sqrt{3}} \left(\frac{\nu}{W} \right) \qquad (1.22)$$

Again the range of validity of this result is determined by the requirement that the thermal transport by convection be small enough so that the thermal gradient is approximately uniform which is required for the assumed density function to be valid. This requires the thermal diffusion length, $\delta_{Thermal} = \kappa / \hat{v}_\theta >> a$ or for the thermal Peclet number $Pe_{Thermal} = \hat{v}_\theta \, a / \kappa << 1$. From the above result, we see

that this requires $Gr\,\nu/\kappa = Ra_{Thermal} << 384\sqrt{3} = 665$. Dressler compares his result to a numerical computation carried out by Robertson and Spradley [6] for a differentially heated square in which it is shown that v_{max} is virtually independent of Rayleigh number up to $Ra \approx 1000$ and only falls off by 20% at Ra = 6500. For small Prandtl number fluids, say Pr ~ 0.01, this model should be reasonably valid up to Gr ~ 10^5-10^6.

An approximation for the transient can be made as before by assuming a solution of the form $\bar{v}_\theta(t) = \bar{v}_\theta\left(1-e^{-t/\tau}\right)$. Putting this into Eq. (1.21), the steady state portion of the solution cancels out leaving

$$\frac{1}{\tau}\frac{g\Delta T a^2}{32\nu}\left(\zeta-\zeta^3\right) = \frac{g\Delta T}{4}\zeta.$$

From this, we find the time constant is given by

$$\tau = \frac{a^2}{8\nu}\left(1-\zeta^2\right)$$

where ζ is the radius of the contour chosen for the integration path.

Fig. 1.5 shows the velocity profiles at various times as the velocity transient builds up to its steady state. For steady state, $\zeta = 1/\sqrt{3}$ gives the maximum velocity and would produce $\tau = a^2/12\,\nu = 0.083\,a^2/\nu$ which is somewhat longer than the dominant term in the exact solution. As can be seen in Fig. 1.5, during the early stages of the transient, the maximum velocity occurs nearer to perimeter ($\hat{\zeta} \approx 1$). Of course, taking $\zeta = 1$ would result in $\tau = 0$ since v_θ is zero around the perimeter. Selecting a ζ half way between $1/\sqrt{3}$ and 1 gives $\tau = 0.047\,a^2/\nu$. Fig. 1.6 compares the build-up of velocity predicted by these approximations with the exact solution. The latter estimate is seen to be a better approximation for the initial rise time where the higher order terms in Eq. (1.20) are important, whereas some average value such as $0.065\,a^2/\nu$ gives a better overall fit.

Eq. (1.21) can also be solved for periodic accelerations. Let $g(t)=\hat{g}e^{i\omega t}$. After a transient, the velocity will take the form $v(r,t)=\hat{v}(r)e^{i\omega t}$.

$$\left[r^2\frac{d^2\hat{v}}{dr^2}+r\frac{d\hat{v}}{dr}-\left(1+\frac{i\omega r^2}{\nu}\right)\hat{v}\right]+\frac{g\Delta\rho r^3}{2a\nu}=0.$$

It is convenient to express the solution as a Fourier-Bessel series,

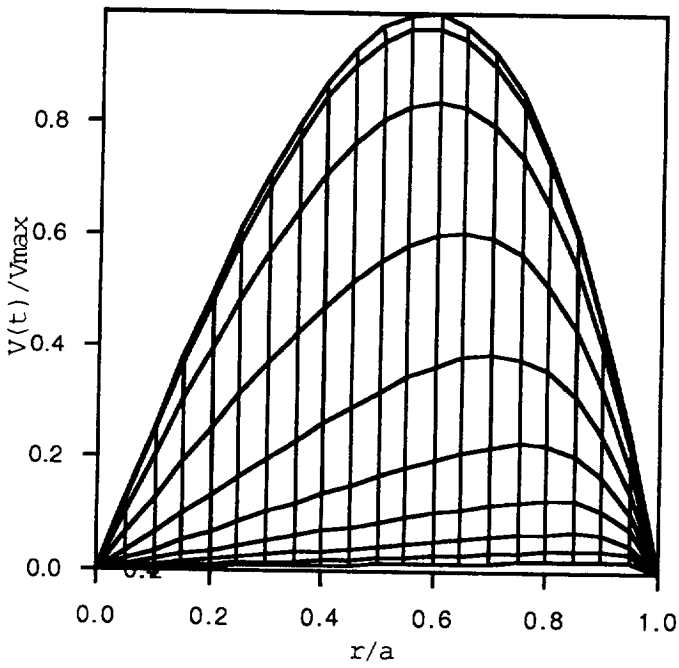

Fig. 1.5 Velocity build-up in Dessler's' solution. Contours represent $t^* = 10^{-3}$ to $10^{-0.3}$ in intervals of $10^{-.3}$.

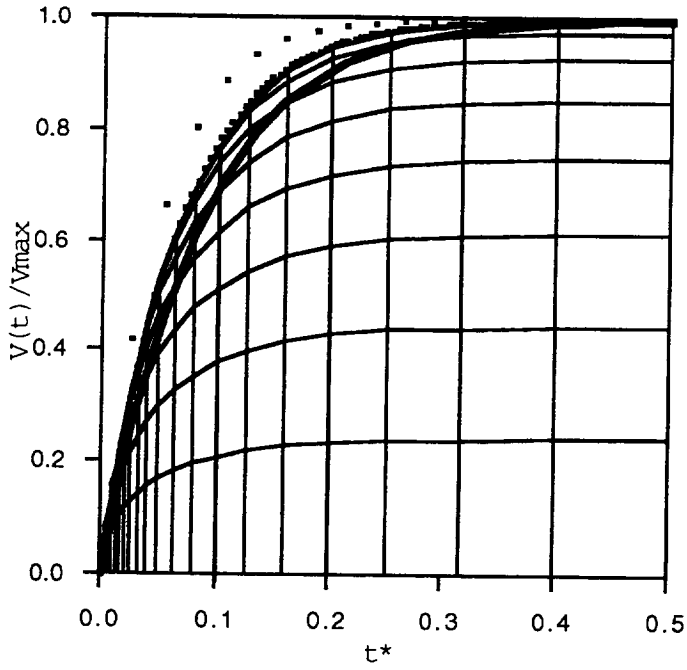

Fig. 1.6 Build-up of maximum velocity with time from Dressler's solution (wire frame plot). Heavy line represents approximate solution with integration path taken around $\zeta = 1/3^{1/2}$. Points represent the approximate solution with integration path taken at $\zeta = 0.788$. The dotted line represents the approximate solution with a time constant taken as an average of the two extreme cases.

$$\hat{v}(r) = -\frac{g(\Delta\rho/\rho)a^2}{\nu}\sum_{n=1}^{\infty}\frac{J_1(\lambda_n\zeta)}{\lambda_n J_0(\lambda_n)}\frac{1}{\left[\lambda_n^2 + i\Omega\right]} \tag{1.23}$$

where Ω is the dimensionless frequency, $\omega a^2/\nu$. This choice of representation automatically enforces the no slip boundary condition at r=a. Note that in the limit $\Omega << \lambda_n^2$, the solution reduces to

$$\hat{v}(r) = -\frac{g(\Delta\rho/\rho)a^2}{\nu}\sum_{n=1}^{\infty}\frac{J_1(\lambda_n\zeta)}{\lambda_n^3 J_0(\lambda_n)}$$

which is a series representation of Dressler's steady state solution. On the other hand, if $\Omega >> \lambda_n^2$, then

$$\hat{v}(r) = i\frac{\hat{g}(\Delta\rho/\rho)a^2}{\nu\Omega}\sum_{n=1}^{\infty}\frac{J_1(\lambda_n\zeta)}{\lambda_n J_0(\lambda_n)}$$

where it is seen that the amplitude of the velocity is inversely proportional to the frequency. Fig. 1.7 shows the velocity amplitude as a function of r for various values of Ω. The drop in amplitude does not become significant until ω approaches the reciprocal of the time constant for the transient case, $\lambda_1^2\nu/a^2$. It is also interesting to note that for very high frequencies, the peak amplitude occurs closer to r = a. This is similar to the initial build up of the flow field for the transient case shown by Dressler.

1.4.1 Square or Rectangular Box

The 2-dimensional flow problem in a square or rectangular box may be formulated by replacing u and v in the x- and y-momentum equations (Eq. (1.6)) by $u = -\frac{\partial\psi}{\partial y}$ and $v = \frac{\partial\psi}{\partial x}$ to satisfy the continuity equation, cross differentiating, and subtracting to eliminate the pressure terms. The result is a single 4th-order partial differential equation for the stream function ψ. Neglecting the inertial terms, this equation becomes

$$\frac{\partial^4\psi}{\partial x^4} + 2\frac{\partial^4\psi}{\partial x^2\partial y^2} + \frac{\partial^4\psi}{\partial y^4} + \frac{g_y}{\mu}\frac{\partial\rho}{\partial x} - \frac{g_x}{\mu}\frac{\partial\rho}{\partial y} = 0 \tag{1.24}$$

where g_x and g_y are the components of the gravity vector and $\rho(x,y)$ is the density of the fluid. The boundary conditions require that ψ and its normal derivative vanish at each wall to enforce the no-slip condition.

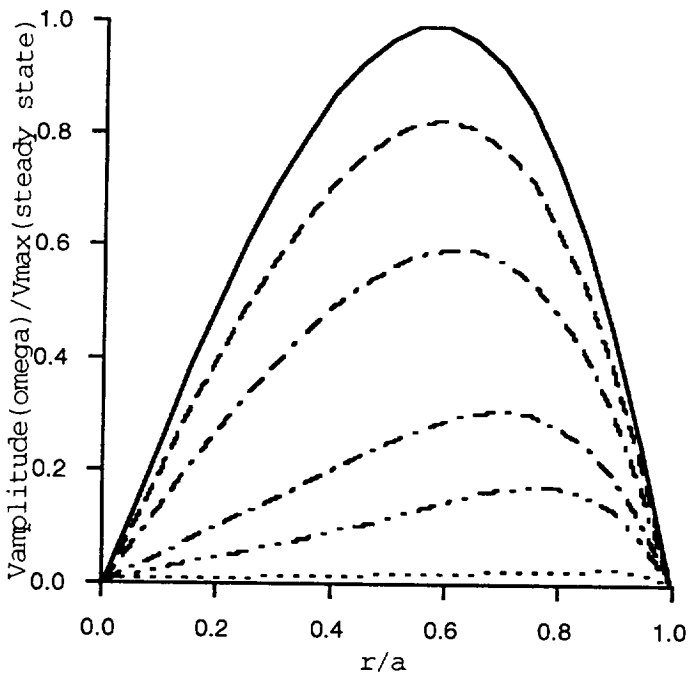

Fig. 1.7 Velocity amplitudes from periodic disturbances with various dimensionless frequencies Ω normalized by maximum steady state velocity for the case of a differentially heated vertical circular cavity. Value for Ω from the top down are 0, 10, 20,50,100,1000.

Unfortunately this biharmonic equation has no known analytical solution. If the aspect ratio is very large or very small, either the x- or y-derivatives may be ignored to give the 1-dimensional solutions described previously. While these solutions accurately describe the core flows, they cannot describe the flows near the ends.

Cormack, Leal, and Imberger (CLI) carried out an extensive theoretical [7], numerical [8], and experimental [9] study of flows in this type of system. In their analytical approach, they break the model into two parts: a core region in which the flow is parallel and dominated by viscous effects; and end regions which turn the flow. For the core region, they expand the stream function, the temperature field, and the vorticity as a power series of the aspect ratio W/L, and find the solution for the stream function in the core region has the form

$$\psi = (C_1 + C_2\, W/L + C_3 (W/L)^2 + \ldots)(\tilde{y}^4 - 2\tilde{y}^3 + \tilde{y}^2)$$

where $\tilde{y}$ = y/W and the C's are functions of the Grashof number which must be determined by matching the core solution to the solution for the end regions. The problem is equivalent to the classical problem of finding the displacement of a hyrodstatically loaded rectangular elastic membrane with clamped edges, the difficulties of which are well-known. Unfortunately the solutions for the end regions must be carried to order 3 to get non-trivial solutions. CLI use Laplace transform theory techniques and obtain a solution as an expansion in Papkowich-Fadle eigenfunctions. The determination of these eigenfunctions must be done numerically, which, as it turns out, is actually more difficult than solving the flow equations numerically. Therefore, it is not possible to obtain a simple analytical expression for the stream function or the velocity profile in the end regions. They did, however, obtain values for the C's in the above equation so that the velocity field in the core region can be written,

$$u(y) = \frac{Gr}{12}\frac{\nu}{L}\left(1 - 3.48 \times 10^{-6}\, Gr^2 Pr^2 (W/L)^3 + \ldots.\right)\left[2\tilde{y}^3 - 3\tilde{y}^2 + \tilde{y}\right].$$

The temperature field in the core region is given by

$$\frac{T - T_c}{T_h - T_c} = \frac{x}{L} + \frac{GrPr}{1440}\frac{W}{L}\left(12\tilde{y}^5 - 30\tilde{y}^4 + 20\tilde{y}^3 - 1\right) + O\left(Gr^2\right).$$

We see that the velocity will have its maximum value at $\tilde{y} = (3 \pm \sqrt{3}\ )/6$ which gives a maximum velocity of

$$\hat{u} = \frac{g\beta \Delta T W^3}{72\sqrt{3}\ \nu L}\left(1 - 3.48 \times 10^{-6}\, Gr^2 Pr^2 (W/L)^3 + \ldots.\right)$$

which is the same result obtained by Eq. (1.19) for L >> W . It is interesting to note from this expansion that for W = L, the velocity is linear with Gr so long as Ra = Gr Pr << 536. This is the same order of magnitude we estimated earlier from the thermal Peclet number. Furthermore, from the CLI equation for temperature, one can deduce that the perturbation due to convective flow would be

$$\frac{\delta T}{T} = \frac{GrPr(W/L)}{1440} = \frac{g\beta\Delta T W^4}{1440\nu\kappa L}$$

which has the same functional form as the Langbein-Tiby model in the steady state limit, but numerically is diminished by more than 3 orders of magnitude.

Bejan and Tien [10] obtained an approximation to the flow in a long horizontal cylindrical tube of length L and radius a with differentially heated end walls. Their first order solution can be written

$$u(\eta) = \frac{g\beta\Delta T a^3}{8\nu L}\left(\eta^3 - \eta\right)\sin\theta$$

where η is r/a and θ is the angular position relative to the horizontal plane. Again the maximum velocity will occur at $\theta = \pi/2$ and $\eta = 3^{-1/2}$ and can be written

$$\hat{u} = \frac{g\beta\Delta T a^3}{12\sqrt{3}\,\nu L} = \frac{g\beta\Delta T\, W^3}{96\sqrt{3}\,\nu L}.$$

The flow profile in the vertical plane is quite similar to that in a horizontal slot except the velocity is 25% lower because of the additional drag from the cylindrical walls. Even so, it may be seen that the simplistic model of flow in a horizontal slot gives reasonably accurate estimates to the more complicated problem of flow in a cylindrical.

Batchelor [11] considered the flow and heat transfer in a thin vertical slot (L>>W). He expands the stream function and the temperature as a power series in terms of Rayleigh numbers. For the first order term, valid for small Ra and L ≈ W , he uses an approximate stream function which he attributes to Grashof (no reference given) which can be written,

$$\psi(x,y) \approx \frac{g\beta(\Delta T/L)W^4}{\nu}\frac{2}{3}\left\{\frac{(x/L)^2(1-x/L)^2(y/W)^2(1-y/W)^2}{(1+W^4/L^4)}\right\}; \quad (1.25)$$

where L is taken along the horizontal or x-axis.

For the case of a square, the velocity may be found from

$$u = \frac{\partial \psi}{\partial y} = \frac{2}{3} Gr \frac{\nu}{L} (x/L)^2 (1-x/L)^2 \left[2(y/W)^3 - 3(y/W)^2 + y/W \right]. \qquad (1.26)$$

The maximum u will occur at x = L/2 and $y = (3 \pm \sqrt{3}\ )W/6$ which becomes

$$\hat{u} = \frac{Gr}{144\sqrt{3}} \frac{\nu}{W}. \qquad (1.27)$$

This model, even though it is not an exact solution to the biharmonic equation, produces streamlines and velocities that agree reasonably well with numerical computations for small Rayleigh numbers as can be seen in Fig. 1.8.

In order to apply of the integral theorem to flows in square or rectangular cavities, one is tempted to use the functional form of Eq. (1.25) to evaluate the derivatives in the viscous term. However, this leads to an inconsistency as will be shown. For example, if one chooses the perimeter of a square cavity as the streamline for the path of integration, the contribution from one side is

$$\int_0^L \nabla^2 \mathbf{v} \bullet d\mathbf{s} = \int_0^L \left(\frac{\partial^2 u}{\partial x^2} + \frac{\partial^2 u}{\partial y^2} \right)_{y=0} dx \ .$$

It is convenient to combine Eq. (1.25) and (1.26) and write

$$u = \frac{288}{\sqrt{3}} \hat{u} (x/L)^2 (1-x/L)^2 \left[2(y/W)^3 - 3(y/W)^2 + y/W \right] \qquad (1.28)$$

The contribution from the $\partial^2 u/\partial x^2$ term vanishes since u is identically zero everywhere along the path. The contribution from the second term yields

$$\int_0^L \frac{\partial^2 u}{\partial y^2} dx = \frac{288}{\sqrt{3}} \frac{1}{30} \left(\frac{-6}{W^2} \right) L \hat{u}.$$

For L = W, the other 3 walls will give the same contribution since $\hat{u}$ and $\hat{v}$ are equal in magnitude. The driving force is given by

$$\oint \rho_0 (1 - \beta \Delta T x/L) \mathbf{g} \bullet d\mathbf{s} = \rho_0 \beta \Delta T \, L. \qquad (1.29)$$

Equating the terms gives a maximum velocity

$$\hat{u} = \frac{15}{8} \frac{g \beta \Delta T W^2}{144\sqrt{3}\,\nu} = \frac{15}{8} \frac{Gr}{144\sqrt{3}} \frac{\nu}{W}.$$

This is inconsistent with the maximum velocity obtained from the velocity function Eq. (1.27), which is indicative of the fact that, even though the velocity function in

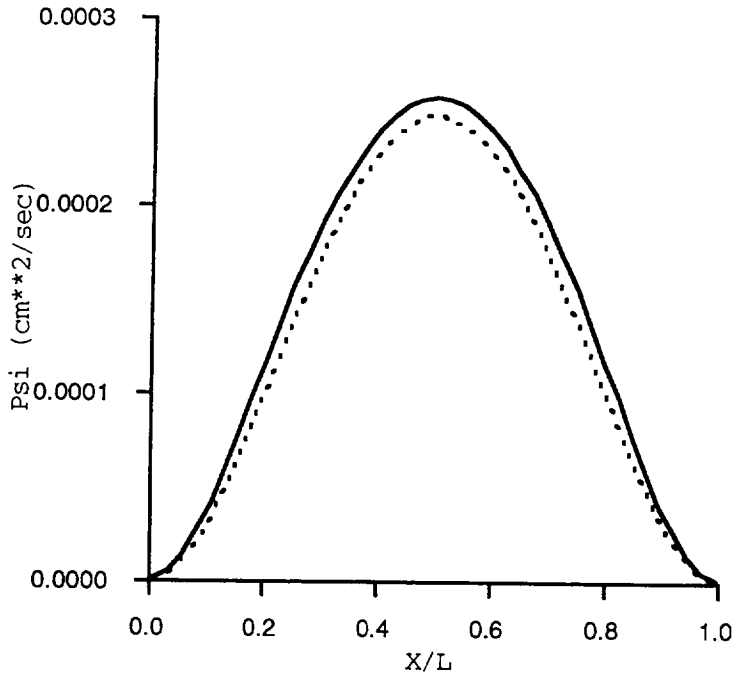

Fig. 1.8 Comparison of stream function computed from Eq. (1.25) (dotted curve) with numerical computation for L = W. The quantity $g \beta \Delta T/\nu$ was taken as 0.1915.

Eq. (1.26) gives reasonable results, it does not exactly satisfy the momentum equation. Or for that matter, neither does the stream function given in Eq. (1.25) exactly satisfy the biharmonic equation as can be verified by differentiation. This can be seen in Fig. 1.9 and 1.9A which compares the stream function computed numerically with Eq. (1.25) in the vicinity of y = 0. Even though the agreement is close, the third derivative of Ψ computed numerically is slightly more than twice that obtained from differentiating Eq.(1.25), which would explain the over-prediction of the velocity by almost a factor of 2. As it turns out, the damping term computed by differentiating Eq. (1.25) at x = L/2 is a very good approximation for the average damping along the integration path. Therefore,

$$\int_0^L \nabla^2 \mathbf{v} \bullet d\mathbf{s} \approx \left\langle \left(\frac{\partial^2 u}{\partial y^2}\right)_{y=0} \right\rangle L = \left(\frac{\partial^2 u}{\partial y^2}\right)_{\substack{x=1/2 \\ y=0}} L = \frac{18}{\sqrt{3}}\left(\frac{-6}{W^2}\right) L\, \hat{u}\,.$$

Each of the other 3 walls will give the same contribution, hence the maximum velocity becomes

$$\hat{u} = \frac{g\beta \Delta T W^2}{144\sqrt{3}\,\nu} = \frac{Gr}{144\sqrt{3}}\frac{\nu}{W}$$

which agrees with Eq. (1.27).

As was pointed out by Batchelor, extension of this model to rectangular configurations quickly breaks down as the aspect ratio departs from unity because the vertical flow field is unrealistically spread over half the length of the channel. This is seen in Fig. 1.10-1.12 which compares the x-dependence of the stream function along the center line computed from Eq. (1.25) with the numerical results.

Experience from the numerical modeling suggests a model for rectangular configurations in which the end flows turn within the region L/2 for $W < L \leq 2\,W$, and within W for $L > 2\,W$, assuming that L is taken along the horizontal or x-axis. Using this model, Eq. (1.25) can be differentiated to obtain the maximum horizontal and vertical velocities for $L < 2\,W$ which yields

$$u = -\frac{\partial \Psi}{\partial y}\Big)_{x=L/2} = \frac{Gr}{12}\frac{\nu}{L}\left\{\frac{y/W - 3(y/W)^2 + 2(y/W)^3}{1 + W^4/L^4}\right\} \qquad (1.29)$$

from which

$$\hat{u} = \frac{Gr}{72\sqrt{3}}\frac{\nu}{L}\left(\frac{1}{1+W^4/L^4}\right) \qquad 2\,L > W \qquad (1.30)$$

and

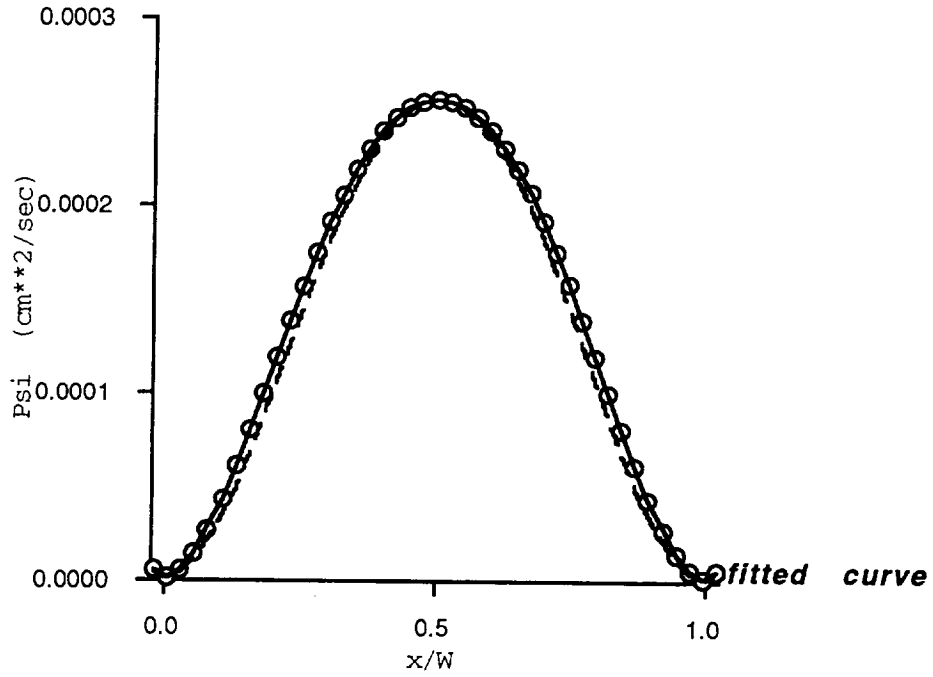

Fig . 1.9 Shape of the stream function computed numerically compared to Eq. (1.25) (dashed line) normalized to give the same peak value. The numerical values (circles) were fit with an 8th degree polynomial (solid line) which was differentiated at x = 0 to obtain $\Psi'''(0) = 0.10972$, slightly more than twice the value 0.0496 from Eq. (1.25) even after it was normalized to give the same peak value.

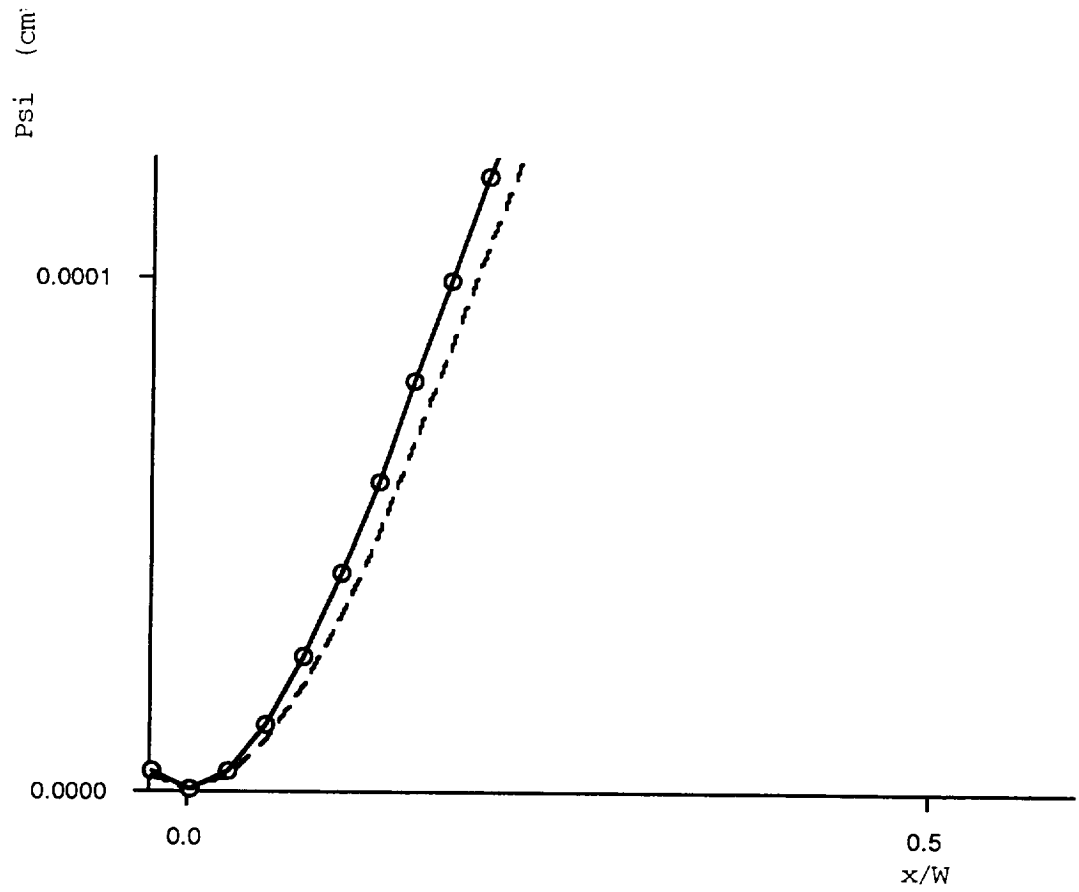

Fig.1.9A Magnified view of the previous figure showing the discrepancy between Batchelor's approximate model in the region of x = 0

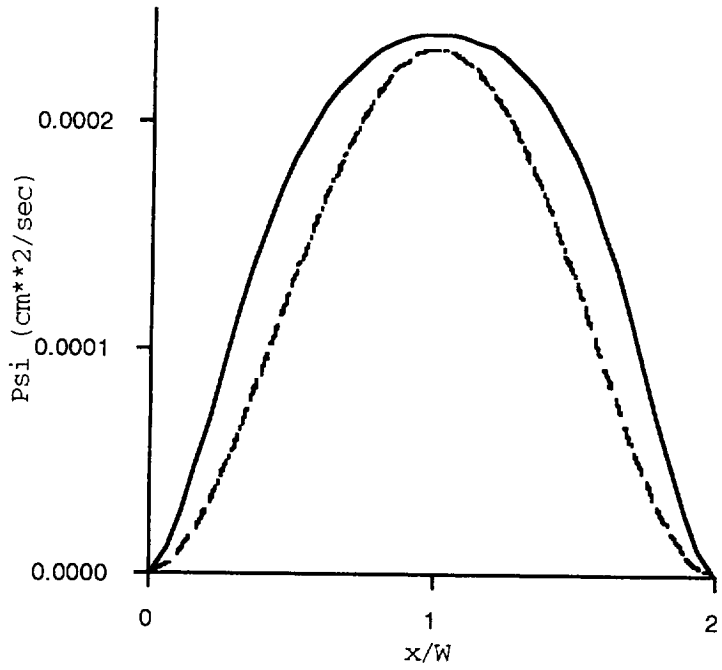

Fig. 1.10 Comparison of stream function computed from Batchelor's approximate model (dashed curve) with numerical computation for L = 2 W.

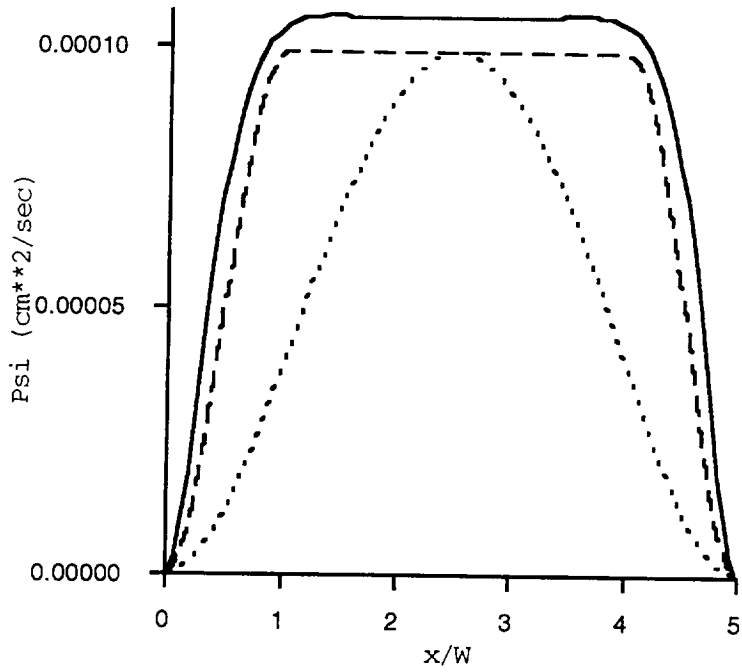

Fig. 1.11 Comparison of stream function computed from Batchelor's approximate model (dotted curve) and from Eq. (1.33) (dashed curve) with numerical computation (solid line) for L = 5W.

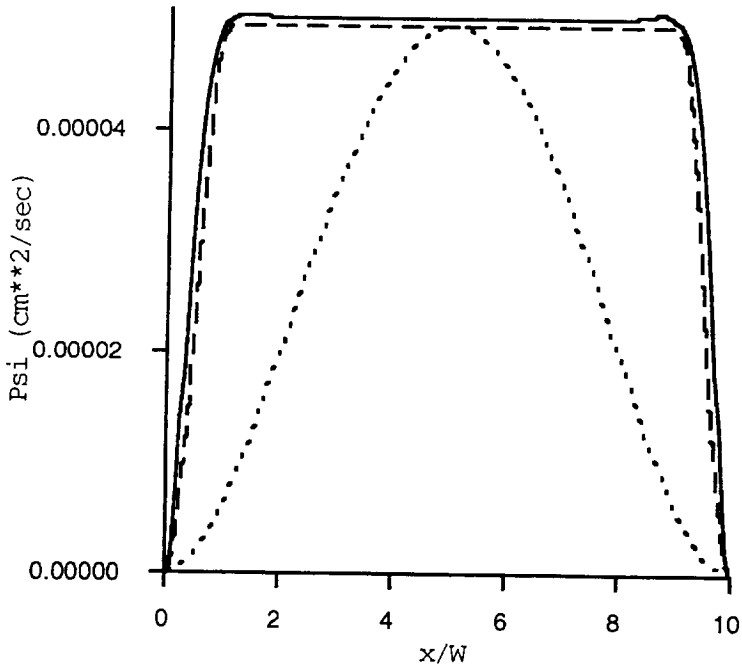

Fig. 1.12 Comparison of stream function computed from Batchelor's approximate model (dotted curve) and from Eq. (1.33) (dashed curve) with numerical computation (solid line) for L = 10W.

$$v = \frac{\partial \Psi}{\partial x}\Big)_{y=W/2} = \frac{Gr}{12}\frac{\nu}{L}\frac{W}{L}\left\{\frac{x/L - 3(x/L)^2 + 2(x/L)^3}{1+W^4/L^4}\right\} \qquad (1.31)$$

from which

$$\hat{v} = \frac{Gr}{72\sqrt{3}}\frac{\nu}{L}\frac{W}{L}\left(\frac{1}{1+W^4/L^4}\right) \qquad L < 2\,W. \qquad (1.32)$$

Since the magnitude of the stream function peak is predicted with reasonable accuracy by Eq. (1.25) as was seen in Fig. 1.10-1.12, Eq. (1.29) will give a good approximation for the maximum horizontal velocity for all L > W/2. In fact, for L >> W, this simply reduces to the one-dimensional result for the horizontal slot given by Eq. (1.19). Similarly, if L < W, Eq. (1.30) gives a good approximation for the maximum vertical velocity as can be seen by multiplying the top and bottom by L^4/W^4. This gives the same form as Eq. (1.29) except L and W are interchanged. This reduces to the one-dimensional vertical slot Eq. (1.10) in the limit L << W if the length scale in the Gr is taken as the smallest dimension - in this case L.

To obtain a reasonable estimate for $\hat{v}$ for L > 2 W, we introduce a stream function for the end region that peaks at W using a form similar to Eq. (1.25),

$$\Psi(x,1/2) \approx \frac{g\beta(\Delta T/L)W^4}{\nu}\frac{1}{24}\left\{\frac{(x/2W)^2(1-x/2W)^2}{(1+W^4/L^4)}\right\} \qquad (1.33).$$

This can be differentiated to give

$$\hat{v} = \frac{Gr}{144\sqrt{3}}\frac{\nu}{L}\left(\frac{1}{1+W^4/L^4}\right), \qquad L > 2\,W \qquad (1.34)$$

Similarly to obtain $\hat{u}$ for W > 2 L, we introduce a stream function that peaks at L

$$\Psi(1/2,y) \approx \frac{g\beta(\Delta T/L)L^4}{\nu}\frac{1}{24}\left\{\frac{(y/2L)^2(1-y/2L)^2}{(1+L^4/W^4)}\right\} \qquad (1.35)$$

which can be differentiated to give

$$\hat{u} = \frac{Gr}{144\sqrt{3}}\frac{\nu}{L}\frac{W}{L}\left(\frac{1}{1+W^4/L^4}\right) = \frac{Gr^*}{144\sqrt{3}}\frac{\nu}{L}\left(\frac{1}{1+L^4/W^4}\right), \quad W > 2\,L \qquad (1.36)$$

where $Gr^* = g\,\beta\,\Delta T\,L^3/\nu^2$.

To obtain an approximation for the time constant for response to transient accelerations, the integral theorem may be used. Choose horizontal streamline along ± a' relative to the center line and vertical streamlines along ± b' and use the average values for viscous damping terms as described previously. Thus Eq. (1.7) may be written

$$\int_{-b'}^{b'} \langle|\dot{u}|\rangle_{y=a'}\, dx + \int_{-a'}^{a'} \langle|\dot{v}|\rangle_{x=b'}\, dy + \nu\left[\int_{-b'}^{b'} \left\langle\left|\frac{\partial^2 u}{\partial y^2}\right|\right\rangle_{y=a'} dx + \int_{-a'}^{a'} \left\langle\left|\frac{\partial^2 v}{\partial x^2}\right|\right\rangle_{x=b'} dy\right]$$
$$= \frac{1}{2}\oint\left(1-\beta\Delta T\frac{x}{L}\right)\mathbf{g}\bullet d\mathbf{s}$$

To enforce the continuity equation, derivatives of the stream function will be used in lieu of velocity functions. Inserting these and performing the indicated integrations, we obtain

$$\left\langle\frac{\partial\dot{\Psi}}{\partial y}\right\rangle_{y=a'} + \frac{W'}{L'}\left\langle\frac{\partial\dot{\Psi}}{\partial x}\right\rangle_{x=b'} + \nu\left[\left\langle\frac{\partial^3\dot{\Psi}}{\partial y^3}\right\rangle_{y=a'} + \frac{W'}{L'}\left\langle\frac{\partial\dot{\Psi}}{\partial x}\right\rangle_{x=b'}\right]$$
$$= \frac{g\beta\Delta T}{2}\frac{W'}{L'}$$

For L ≈ W, the derivatives of Ψ may be obtained from Eq. (1.25). Assume $\Psi = \overline{\Psi}(1 - e^{-t/\tau})$ where $\overline{\Psi}$ is the steady state solution to the above equation. Inserting this function, the time constant may be obtained as

$$\tau = \frac{W^2}{\nu}\left\{\frac{\left(2\hat{y}^3-3\hat{y}^2+\hat{y}\right)+(W/L)(W'/L')\left(2\hat{x}^3-3\hat{x}^2+\hat{x}\right)}{\left(12\hat{y}-6\right)+(W/L)^3(W'/L')\left(12\hat{x}-6\right)}\right\} \qquad (1.38)$$

where W' = 2 a', L' = 2 b', and $\hat{x}$ and $\hat{y}$ are the values of x/L and y/W respectively for which the velocity is maximum. For L ≈ W it is reasonable to assume that L' and W' stand in the same ratio as L and W. For steady state, the maximum velocity is obtained for $\hat{x} = \hat{y} = \left(3-\sqrt{3}\right)/6$. Putting this into the above, we obtain

$$\tau = \frac{W^2}{\nu}\left\{\frac{1+(W/L)^2}{36\left[1+(W/L)^4\right]}\right\} \qquad (1.39)$$

For W = L, this reduces to $\tau = W^2/36\,\nu = a^2/9\,\nu$, the same as for the one-dimensional case. If L >> W, or W >> L, this also reduces to the one-dimensional case with the shortest dimension as the length scale.

The maximum horizontal and vertical velocities computed from the above model are compared with numerical results for a variety of different shapes in Table 1. Also Fig. 1.10-1.12 compares the model stream function along the center line with numerical results. It can be seen that the model is quite accurate for square or large L/W ratios but is somewhat less accurate for the intermediate cases. This is to be expected considering the crudity of the approximation that describes the turning points in the flow. However, even in the worst cases the model is off by only 20%.

1.5 FLOWS AT LARGE RAYLEIGH NUMBERS

Thus far we have considered cases where the Ra was small enough so that the isotherms were unperturbed by the flow. Let us now expand the approximation method to the case of large Rayleigh numbers where the heat transfer is dominated by the convective flow in the thermal boundary layer. For the time being we ignore the horizontal and concentrate on the vertical flow. The heat transfer equation must also be solved with the flow equation. For the case at hand the terms of interest are

$$v(x)\frac{\partial T}{\partial y} = \kappa\frac{\partial^2 T}{\partial x^2} .$$

Approximate $\frac{\partial T}{\partial y} \approx \frac{\Delta T}{W}$ and $\frac{\partial^2 T}{\partial x^2} \approx \frac{\Delta T}{\delta_T^2}$ where δ_T is the thermal length or the distance over which the temperature changes significantly due to convective flow. If this length is long compared to L/2, heat transport is dominated by conduction; if the thermal length is short compared to L/2, convective heat transfer dominates. Putting these back into the heat transfer equation, the δ_T may be estimated as

$$\frac{1}{\delta_T^2} \approx \frac{\hat{v}}{\kappa W} . \tag{1.40}$$

The viscous damping integral may be written

$$\oint \nabla^2 v \bullet ds = 2\int_0^W \left\langle \frac{\partial^3 \Psi(x,1/2)}{\partial x^3} \right\rangle_{x=0} dy + 2\int_0^L \left\langle \frac{\partial^3 \Psi(1/2,y)}{\partial y^3} \right\rangle_{y=0} dx \tag{1.41}$$

We assume the flow field is contained in some thermal boundary layer b, which is proportional to δ_T, and can be expressed as

$$v(x) = \frac{3\sqrt{3}}{2}\hat{v}\left(2\chi - 3\chi^2 + \chi^3\right); \quad \chi = x/b .$$

Table 1.1.

L (cm)	W (cm)	$g \beta \Delta T / \nu$ ($cm^{-1}sec^{-1}$)	$\hat{u}_{comp}$ (cm\sec)	$\hat{v}_{comp}$ (cm/sec)	$\hat{u}_{est}$ (cm/sec)	$\hat{v}_{est}$ (cm/sec)
1	1	0.1915	7.94×10^{-4}	7.94×10^{-4}	7.68×10^{-4}	7.68×10^{-4}
2	1	0.1915	7.27×10^{-4}	4.50×10^{-4}	7.22×10^{-4}	3.61×10^{-4}
5	1	0.1915	3.26×10^{-4}	1.64×10^{-4}	3.00×10^{-4}	1.50×10^{-4}
10	1	0.1915	1.56×10^{-4}	9.68×10^{-5}	1.54×10^{-4}	7.58×10^{-5}
5	5	0.0050	4.96×10^{-4}	4.96×10^{-4}	5.01×10^{-4}	5.01×10^{-4}
1	5	0.0050	2.50×10^{-5}	4.05×10^{-5}	1.96×10^{-5}	3.91×10^{-5}
10	10	2.83×10^{-5}	1.13×10^{-5}	1.13×10^{-5}	1.14×10^{-5}	1.14×10^{-5}
2	10	2.83×10^{-5}	5.19×10^{-7}	9.79×10^{-7}	4.43×10^{-7}	8.86×10^{-7}
10	2	2.83×10^{-4}	1.81×10^{-6}	1.04×10^{-6}	1.77×10^{-6}	8.86×10^{-7}

Comparison of numerical computations of maximum horizontal and vertical flow velocities with approximates for small Rayleigh Numbers. L is taken to be perpendicular to the g-vector.

The stream function as a function of x may be obtained by integrating this expression,

$$\Psi(x,1/2) = 4\hat{\Psi}\left(\chi^2 - \chi^3 + \chi^4/4\right) \text{ where } \hat{\Psi} = \frac{3\sqrt{3}}{8}\hat{v}b. \tag{1.42}$$

Putting this into Eq. (1.40), we get

$$\frac{1}{\delta_T^2} = \frac{8\hat{\Psi}}{3\sqrt{3}\,b\kappa W}.$$

We relate b to δ_T by $b = \gamma\,\delta_T$ where γ is a constant of proportionality to be determined. Putting this in the above expression we get

$$\frac{1}{b} = \frac{8\hat{\Psi}}{3\sqrt{3}\;\kappa W\gamma^2} \tag{1.43}$$

Differentiating the stream function Eq. (1.42), we obtain

$$\left.\frac{\partial^3\Psi(x)}{\partial x^3}\right)_{x=0} = -\frac{24\hat{\Psi}}{b^3}\,. \tag{1.44}$$

which, with the help of Eq. (1.43), can now be written as,

$$\left.\frac{\partial^3\Psi(x)}{\partial x^3}\right)_{x=0} = -\frac{24\cdot 8^3}{\left(3\sqrt{3}\right)^3\gamma^6}\frac{\hat{\Psi}^4}{(\kappa W)^3}\,. \tag{1.45}$$

Ignoring the other terms for the time being and assuming this term represents the average along the path of the integration as before, the maximum stream function can be obtained by integrating Eq. (1.41) and equating it to the driving term which is still given by Eq. (1.29)

$$\frac{24\cdot 8^3}{\left(3\sqrt{3}\right)^3\gamma^6}\frac{\hat{\Psi}^4}{(\kappa W)^3} = \frac{g\beta\Delta T}{2\nu}$$

from which

$$\hat{\Psi} = \frac{3}{8}\left(\frac{\sqrt{3}}{6}\right)^{1/4}\gamma^{3/2}\left(\frac{g\beta\Delta T\,W^3\kappa^3}{\nu}\right)^{1/4} = 0.275\,\gamma^{3/2}\,(GrPr)^{1/4}\,\kappa\,. \tag{1.46}$$

The maximum velocity may be obtained from the relation

$$\hat{v} = \frac{8\hat{\Psi}}{3\sqrt{3}}\frac{1}{b} = \left(\frac{8}{3\sqrt{3}}\right)^2 \frac{\hat{\Psi}^2}{\kappa W \gamma^2} = \frac{1}{3}\left(\frac{\sqrt{3}}{6}\right)^{1/2} \gamma \left(\frac{Gr}{Pr}\right)^{1/2} \frac{\nu}{W}. \tag{1.47}$$

A series of numerical computations were carried out with large Ra so that the flow would be dominated by the thermal boundary layer at the walls and the maximum stream function and maximum vertical velocity was correlated with the above results (see Table 1.2). The choice of γ is determined by attempting to obtain a consistent model for both the maximum velocity and the maximum stream function. The velocity data would argue for a value of ~1.3 whereas the stream function data would argue for ~1.7. Therefore, a compromise choice of 1.5 is taken. The fact that different values of γ are required to correlate the different quantities reflects the inability to describe the flow field by a simple one-dimensional expression representing some average flow. However, the fact that the range of γ needed to correlate the velocity and stream function data is relatively narrow does indicate that despite the crudity of the model, it does seem to have useful predictive capabilities.

Now an interpolation equation for the transition between low and high Ra can be developed. Assume some sort of effective boundary layer in which the flows along the vertical faces are contained. This effective boundary layer should approach b at large Rayleigh numbers when flows are dominated by the thermal boundary layer and should approach L/2 (or W, whichever is smaller) for smaller values of Ra where the isotherms are not carried by the flow. There are several ways of representing a function with these properties. For example, one could define

$$\frac{1}{\delta_{eff}} = \left(\frac{1}{b} + \frac{2}{L}\right); \quad L < 2W, \tag{1.48}$$

or one could just as easily define

$$\frac{1}{\delta_{eff}^3} = \frac{1}{b^3} + \left(\frac{2}{L}\right)^3; \quad L < 2W, \tag{1.49}$$

or something in between.

We first choose the form of Eq. (1.48). Now Eq. (1.44) becomes

$$\left.\frac{\partial^3 \Psi(x)}{\partial x^3}\right)_{x=0} = -\frac{24\hat{\Psi}}{\delta_{eff}^3} = -24\hat{\Psi}\left(\frac{1}{b} + \frac{2}{L}\right)^3.$$

Using Eq. (1.43) for 1/b, this becomes

Table 1.2

Table 1.2. κ (cm^2/sec)	ν (cm^2/sec)	Pr	Gr	Ra	$\hat{\Psi}_{comp}$ (cm^2/sec)	$\hat{v}_{comp}$ (cm/sec)	γ_1	γ_2
0.001	0.010	10	625000	6250000	0.031	0.117	1.70	1.31
0.001	0.010	10	62500	625000	0.018	0.0378	1.73	1.34
0.001	0.010	10	6250	62500	0.010	0.0116	1.70	1.30
0.001	0.010	10	625	6250	0.004	0.0030	1.41	1.05
0.010	0.010	1	625000	625000	0.162	0.349	1.64	1.23
0.100	0.010	0.1	625000	62500	0.718	0.850	1.40	0.95
1.000	0.010	0.01	625000	6250	3.530	2.20	1.28	0.78

Computations at large Ra used to determine the factor γ. Maximum vertical velocities and stream functions were computed numerically for a 5 cm x 5 cm chamber with a Gr = 6.25 x 10^5 with different values of κ and ν. The γ_1 is the parameter needed to reconcile Eq. (1.46) with the numerically computed maximum stream function and γ_2 is that needed to reconcile Eq. (1.47) with the numerically computed $\hat{v}$.

$$\left.\frac{\partial^3\Psi(x)}{\partial x^3}\right)_{x=0} = -\frac{24\hat{\Psi}}{\delta_{eff}^3} = -24\hat{\Psi}\left(\frac{8\hat{\Psi}}{3\sqrt{3}\,\kappa W\gamma^2}+\frac{2}{L}\right)^3. \qquad L<2W$$

The y-derivative can be expressed as

$$\left.\frac{\partial^3\Psi(y)}{\partial y^3}\right)_{y=0} = -24\hat{\Psi}\left(\frac{2}{W}\right)^3 .$$

Taking these two derivatives as the average terms in Eq. (1.41) and equating the viscous term to the driving term using $\gamma = 3/2$, a 4th order polynomial for Ψ is obtained, i.e.,

$$\hat{\Psi}\left(\frac{8\cdot 2\,\hat{\Psi}}{9\cdot 3\sqrt{3}\,\kappa}+\frac{W}{L}\right)^3+\hat{\Psi}\frac{L}{W} = \frac{g\beta\Delta T W^3}{2^3\,48\nu}$$

or

$$\hat{\Psi}\left(\frac{16\,\hat{\Psi}}{27\sqrt{3}\,\kappa}+\frac{W}{L}\right)^3+\hat{\Psi}\frac{L}{W} = \frac{g\beta\Delta T W^3}{384\nu} . \tag{1.50}$$

Had we chosen the for of Eq. (1.49), this would be

$$\hat{\Psi}\left[\left(\frac{16}{27\sqrt{3}}\frac{\hat{\Psi}}{\kappa}\right)^3+\left(\frac{W}{L}\right)^3\right]+\hat{\Psi}\frac{L}{W} = \frac{Gr\nu}{384} \tag{1.51}$$

These relations hold for $L < 2W$. For $L > 2W$, replace the W/L term by 1/2.

Note that for $W = L$ and $\Psi << \kappa$, these reduces to

$$\hat{\Psi} = \frac{g\beta\Delta T(W/2)^3}{96\nu}$$

which is the maximum value for Eq. (1.25) with $W = L$. For $\Psi >> \kappa$, Eq.(1.46) is recovered.

Having found the maximum stream function, the maximum horizontal and vertical velocities may be determined from,

$$\hat{u} = \frac{8\hat{\Psi}}{3\sqrt{3}}\frac{1}{a};\quad \hat{v} = \frac{8\hat{\Psi}}{3\sqrt{3}}\frac{1}{\delta_{eff}} = \frac{8\hat{\Psi}}{3\sqrt{3}}\left(\frac{32\hat{\Psi}}{27\sqrt{3}\,\kappa W}+\frac{2}{L}\right). \tag{1.53}$$

Again, for L > W/2, substitute 1 for 2/L.

This model was tested against a series of numerical computations for W = L over a wide range of Ra and κ and the results are shown in Fig. 1.13-1.15. According to Eq. (1.50) or (1.51), the dimensionless quantity obtained by dividing the stream function by κ should be a function only of Gr Pr = Ra and the aspect ratio. Similarly, the horizontal and vertical velocities can be expressed in terms of thermal Peclet numbers ($\hat{u}$ or $\hat{v}$ times W/κ) which again should be functions only of Gr Pr and the aspect ratio.

As may be seen in Fig. 1.16, the stream function determined from Eq. (1.51) seems to give better agreement with the numerical results for Pr > 1, whereas Eq. (1.50) seems to give better agreement for Pr <1. A similar trend is seen in the comparison of vertical velocities in Fig. 1.14, although the model slightly over-predicts the velocity for the small Pr cases at large Ra. Actually, there was a convergence problem with the numerical computations for Pr = 0.01 at high Ra, hence the velocity data for these points may not be accurate. Furthermore, the Reynolds numbers for these flows are $O(10^3)$ which means that they may be nearing a bifrucation point where the flow is no longer laminar. The weakest feature of the model appears to be the prediction of horizontal velocity for Pr > 1 at high Ra as may be seen in Fig. 1.15. This comes from the assumption that the y-dependence of the horizontal was still give by Eq. (1.29) for large Gr Pr, which is probably reasonably valid for L >> W, but not for L ≈ W.

1.6 EFFECTS OF AXIAL DENSITY GRADIENTS

Thus far, it has been assumed that the g-vector was always perpendicular to the density gradient. However, most systems of interest will have a thermal of solutal density gradient along the axis of symmetry and the g-vector can have both axial and transverse components. Therefore, it is necessary to investigate the possible effects of an axial stabilizing or destabilizing density gradient on the flows produced by a transverse acceleration.

Consider a two-dimensional chamber with length L and width W oriented nearly along the g-vector but with a slight tilt. Take the x-axis along the length and the y-axis in the transverse direction so that the g-vector can be resolved into components g_x and g_y with $g_x >> g_y$. Assume a linear thermal gradient is imposed along the x-axis.

As stated previously, neglecting inertial effects, the steady state flow can be described by Eq. (1.24)

$$\nabla^4\Psi = \frac{g_y\beta}{\nu}\frac{\partial T}{\partial x} - \frac{g_x\beta}{\nu}\frac{\partial T}{\partial y}.$$

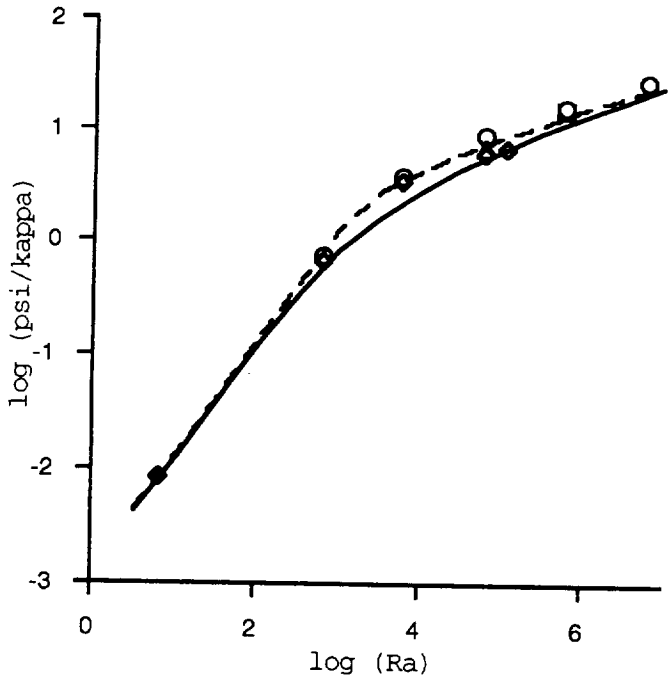

Fig 1.13. Maximum stream function normalized by the thermal diffusivity vs. Ra for different Prandtl numbers. Symbols represent Pr = .01 (diamonds), Pr = 0.1 (triangle), Pr =1.0 (square), Pr = 10 (circles). The solid and dashed line represent two different interpolation schemes in the approximate model (see text).

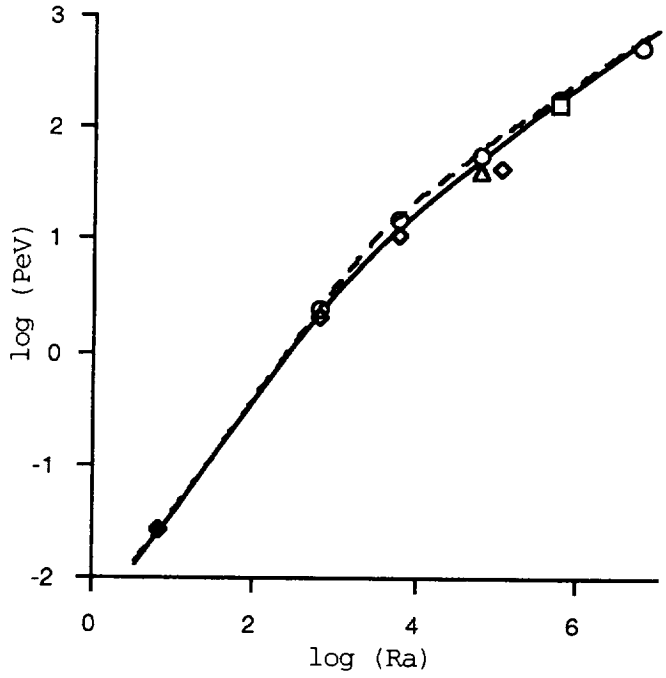

Fig 1.14. Vertical Thermal Peclet number vs. Ra for different Prandtl numbers. Symbols represent Pr = .01 (diamonds), Pr = 0.1 (triangle), Pr =1.0 (square), Pr = 10 (circles). The solid and dashed line represent two different interpolation schemes in the approximate model (see text).

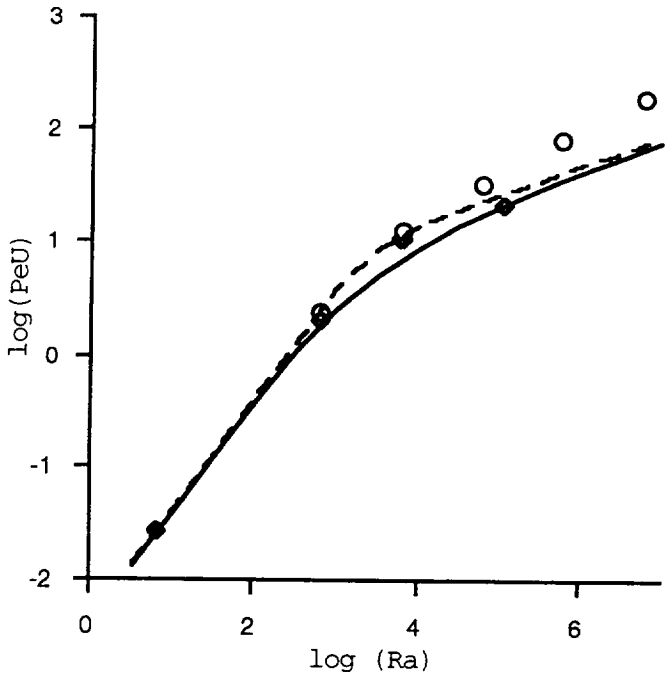

Fig 1.15. Horizontal thermal Peclet number vs. Ra for different Prandtl numbers. Symbols represent Pr = .01 (diamonds), Pr = 10 (circles). The solid and dashed line represent two different interpolation schemes in the approximate model (see text).

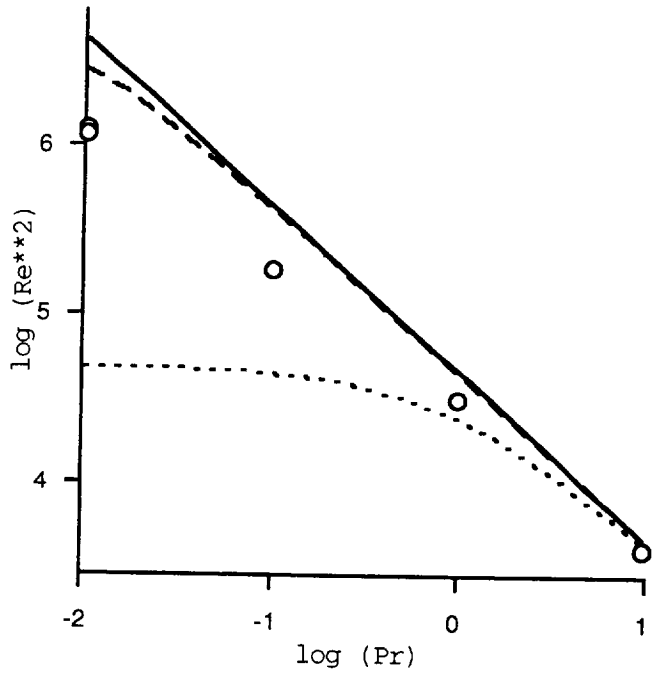

Fig. 1.16 Plot of the Reynolds number squared vs. Pr for constant Gr = 6.25 x 10^5. The solid line represents the scaling law $Re^2 \sim Gr/Pr$, the dashed line represents the predictions based on Eq. (1.53), and the dotted line represents scaling based on Goldstein's approximate solution for a free heated vertical wall in which $Re^2 \sim Gr/(Pr + 20/21)$. Both scaling laws were adjusted to converge at Pr =10.

This formulation assumes that $\beta = (1/\rho)\partial\rho/\partial T < 0$ and g_x and g_y are taken as positive in the x- and y-directions respectively (or that $\beta = -(1/\rho)\partial\rho/\partial T > 0$ and the accelerations are taken as positive along the positive coordinate directions).

The heat flow is described by

$$u\frac{\partial T}{\partial x} + v\frac{\partial T}{\partial y} = \kappa\left(\frac{\partial^2 T}{\partial x^2} + \frac{\partial^2 T}{\partial y^2}\right). \tag{1.54}$$

Since the core flow is essentially one-dimensional, Eq. (1.24) reduces to

$$\nabla^4\Psi \rightarrow \frac{\partial^4\Psi}{\partial y^4} = \frac{\partial^3 u}{\partial y^3} = \frac{g_y\beta}{\nu}\frac{\partial T}{\partial x} - \frac{g_x\beta}{\nu}\frac{\partial T}{\partial y}. \tag{1.55}$$

Assume the temperature field can be described by

$$T(x,y) = \frac{\Delta T}{L}x + \tilde{T}(y) \tag{1.56}$$

which allows Eq. (1.54) to be reduced to

$$u\frac{\Delta T}{L} = \kappa\left(\frac{\partial^2\tilde{T}}{\partial y^2}\right). \tag{1.57}$$

Introduce a dimensionless length $\eta = y/a$ where $a = W/2$. Eq. (1.55) and (1.57) can be written

$$u'''(\eta) = -\frac{g_x\beta\tilde{T}'a^2}{\nu} + \frac{g_y\beta(\Delta T/L)a^3}{\nu} \tag{1.58}$$

and

$$u(\Delta T/L)a^2 = \kappa\tilde{T}'' \tag{1.59}$$

where the prime denotes differentiation with respect to η. Differentiating Eq. (1.58 again and using Eq. (1.59) to eliminate $\tilde{T}''$ gives

$$u^{IV}(\eta) = -\frac{g_x\beta(\Delta T/L)a^4}{\kappa\nu}u(\eta) = -Ra\ u(\eta). \tag{1.60}$$

The solution to this equation is

$$u(\eta) = C_1\sinh(K\eta) + C_2\cosh(K\eta) + C_3\sin(K\eta) + C_4\cos(K\eta) \tag{1.70}$$

where $K = (-Ra)^{1/4}$. Conservation of flow requires $\int_{-1}^{1} u(\eta)\,d\eta = 0$ which eliminates the even terms; hence, $C_2 = C_4 = 0$. The "no slip" boundary condition at the walls requires

$$C_1 \sinh(K) + C_3 \sin(K) = 0. \tag{1.70}$$

Putting the velocity function $u(\eta)$ from Eq. (1.70) back into the heat transfer equation, Eq. (1.59), yields

$$\left(C_1 \sinh(K\eta) + C_3 \sin(K\eta)\right)\frac{\Delta T a^2}{L} = \kappa \tilde{T}''. \tag{1.72}$$

Integrating twice gives

$$\tilde{T}(\eta) = \frac{\Delta T a^2}{L\kappa}\left(\frac{C_1}{K^2}\sinh(K\eta) - \frac{C_3}{K^2}\sin(K\eta) + C_5\,\eta\right). \tag{1.73}$$

Putting the first integral of Eq. (1.72) back into Eq. (1.58), we obtain

$$\begin{aligned} u'''(\eta) &= \frac{g_y \beta}{\nu}\frac{\Delta T a^3}{L} - \frac{g_x \beta}{\nu\kappa}\frac{\Delta T a^4}{L}\left(\frac{C_1}{K}\cosh(K\eta) - \frac{C_3}{K}\cos(K\eta) + C_5\right) \\ &= C_1 K^3 \cosh(K\eta) - C_3 K^3 \cos(K\eta) \end{aligned} \tag{1.74}$$

which allows C_5 to be identified as

$$C_5 = \frac{g_y}{g_x}\frac{\kappa}{a}. \tag{1.75}$$

This allows the temperature to be written as

$$\tilde{T}(\eta) = \frac{\Delta T a^2}{L\kappa}\left(\frac{C_1}{K^2}\sinh(K\eta) - \frac{C_3}{K^2}\sin(K\eta) + \frac{g_y}{g_x}\frac{\kappa}{a}\eta\right). \tag{1.76}$$

The remaining coefficient must be determined from the thermal boundary condition at the walls. For insulating walls, $\tilde{T}'(\pm 1) = 0$. Differentiating Eq. (1.76), we obtain

$$C_1 \cosh(K) - C_3 \cos(K) = K\frac{g_y}{g_x}\frac{\kappa}{a} \tag{1.77}$$

which together with Eq. (1.71) allows the determination of C_1 and C_3. The final result can be written

$$u(\eta) = K\frac{g_y}{g_x}\frac{\kappa}{a}\left(\frac{-\sin(K)\sinh(K\eta)+\sinh(K)\sin(K\eta)}{\sin(K)\cosh(K)+\cos(K)\sinh(K)}\right) \tag{1.78}$$

and

$$T(\eta) = \frac{\Delta T}{L}\left\{x-\frac{g_y}{g_x}\frac{a}{K}\left(\frac{\sin(K)\sinh(K\eta)+\sinh(K)\sin(K\eta)}{\sin(K)\cosh(K)+\cos(K)\sinh(K)}-K\eta\right)\right\} \tag{1.79}$$

For a stabilizing gradient, the Ra is > 0, which means that K is complex, i.e.,

$$K = (-1)^{1/4}Ra^{1/4} = \left(\frac{\sqrt{2}}{2}+i\frac{\sqrt{2}}{2}\right)Ra^{1/4} = \gamma(1+i). \tag{1.80}$$

Putting this back into Eq. (1.78, we get

$$U(\eta) = 2\gamma\frac{g_y}{g_x}\frac{\kappa}{a}\left[\frac{\cos(\gamma)\sinh(\gamma)\sin(\gamma\eta)\cosh(\gamma\eta)-\sin(\gamma)\cosh(\gamma)\cos(\gamma\eta)\sinh(\gamma\eta)}{\sin(\gamma)\cos(\gamma)+\sinh(\gamma)\cosh(\gamma)}\right]$$

(1.79)

This may be put into a more recognizable form by expanding about γ and then replacing γ with $\sqrt{2}Ra^{1/4}/2$ to get

$$U(\eta) = \frac{g_y\beta(\Delta T/L)a^3}{\nu}\left[\frac{1}{6}(\eta^3-\eta)-\frac{Ra}{5040}(\eta^7-7\eta^5+35\eta^3-29\eta)+O(Ra^3)\right] \tag{1.80}$$

The first term in the series represents the core flow in a horizontal slot and the second term represents the first order correction from the stabilizing gradient characterized by Ra. However, note that the correction is minuscule for small values of Ra for which this expansion is valid.

Similarly, the temperature perturbation may be written

$$\tilde{T}(\eta) = -\frac{\Delta T}{L}\frac{g_y}{g_x}\frac{a}{\gamma}\left(\frac{\sin(\gamma)\cosh(\gamma)\sin(\gamma\eta)\cosh(\gamma\eta)+\cos(\gamma)\sinh(\gamma)\cos(\gamma\eta)\sinh(\gamma\eta)}{\sin(\gamma)\cos(\gamma)+\sinh(\gamma)\cosh(\eta)}-\gamma\eta\right)$$

(1.81)

Expanding about γ and replacing γ with $\sqrt{2}Ra^{1/4}/2$ as before

$$\tilde{T}(\eta) = \Delta T \frac{a}{L} \frac{g_y \beta (\Delta T/) a^4}{1080 \kappa \nu} \left(9\eta^5 - 30\eta^3 + 45\eta\right) + O\left(Ra^2\right). \qquad (1.82)$$

(Note: This is identical to the result of Cormack, Leal, and Imberger discussed in Section 1.4.1 as may be seen by setting y = 0 and W = 2 a in their expression and comparing it to the above expression with $\eta = 0$.)

Since the coefficient of Eq. (1.78) can also be written as

$$\frac{g_y}{g_x}\frac{\kappa}{a} = \frac{g_y \beta (\Delta T/L) a^3}{Ra(x)\nu} = \frac{9\sqrt{3}\,\hat{u}_0}{Ra(x)},$$

where $\hat{u}_0$ is the maximum velocity that would be attained in the absence of the effect of the x-component of acceleration which can be obtained from Eq. (1.80), it can be seen that the ratio

$$\frac{u(\eta)}{\hat{u}_0} = \frac{9\sqrt{3}K}{Ra(x)}\left(\frac{-\sin(K)\sinh(K\eta) + \sinh(K)\sin(K\eta)}{\sin(K)\cosh(K) + \cos(K)\sinh(K)}\right) \qquad (1.83)$$

is a function of Ra(x) only. Fig. 1.17 shows this velocity ratio for various stabilizing and destabilizing values of the Ra.

Similarly, since the maximum temperature perturbation from the y-acceleration driven flow form Eq. (1.82) is seen to be $\hat{\tilde{T}}_0 = \frac{Ra(y)\Delta T W}{45\,L}$, the temperature perturbation can be normalized to

$$\frac{T(\eta)}{\hat{\tilde{T}}_0} = \left(-\frac{45}{Ra(x)}\frac{1}{K}\left(\frac{\sin(K)\sinh(K\eta) + \sinh(K)\sin(K\eta)}{\sin(K)\cosh(K) + \cos(K)\sinh(K)} - K\eta\right)\right) \qquad (1.84)$$

which is also a function of Ra(x) only. Fig. 1.18 shows how this ratio varies with various stabilizing and destabilizing values of Ra.

Notice that the velocity and temperature perturbation decreases slowly with increasing Ra > 0, but increases rapidly as Ra < 0. This is seen more vividly in Fig. 1.19. In fact there is a singularity at K = 2.365 when the denominator of Eq. (1.79) and (1.81) goes to zero. This corresponds to Ra(x) = -31.285, which presumably is the critical Ra for this configuration. Inspection of the corresponding equations for Ra > 0 where $K = \gamma(1+i)$ shows no singularities. The normalized effect of an axial acceleration can be represented empirically by $|Ra_c|/(|Ra_c|+Ra(x))$ as may be seen in Fig. 1.19 From this, it is apparent that the stabilizing Ra(x) must be substantially greater than $|Ra_c|$ in order to be effective.

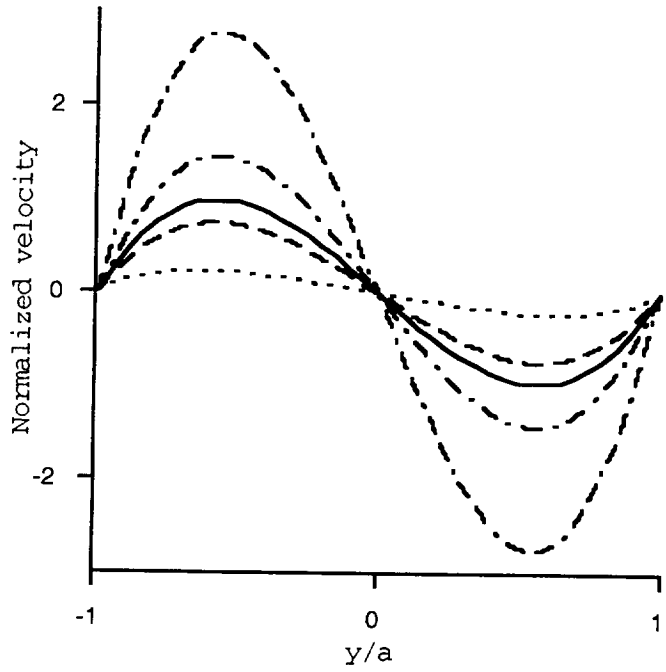

Fig. 1.17 Core velocity for different axial accelerations normalized by maximum core velocity with no axial acceleration (Ra=0). Solid line corresponds to Ra = 0; dot-dashed line to Ra = -10; dash-dash-dot line to Ra = -20; dashed line to Ra = 10; dotted line to Ra = 100. Here $Ra = \frac{g_x \beta (\Delta T / L) a^4}{\kappa \nu}$.

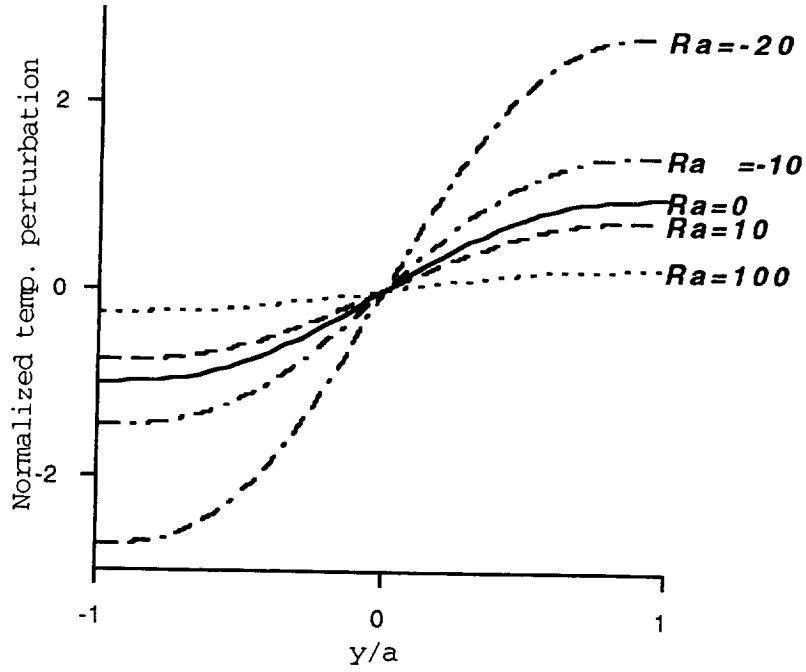

Fig. 1.18 Temperature perturbation for different axial acceleration normalized by the maximum perturbation for no axial acceleration (Ra=0). Here

$$Ra = \frac{g_x \beta (\Delta T / L) a^4}{\kappa \nu}.$$

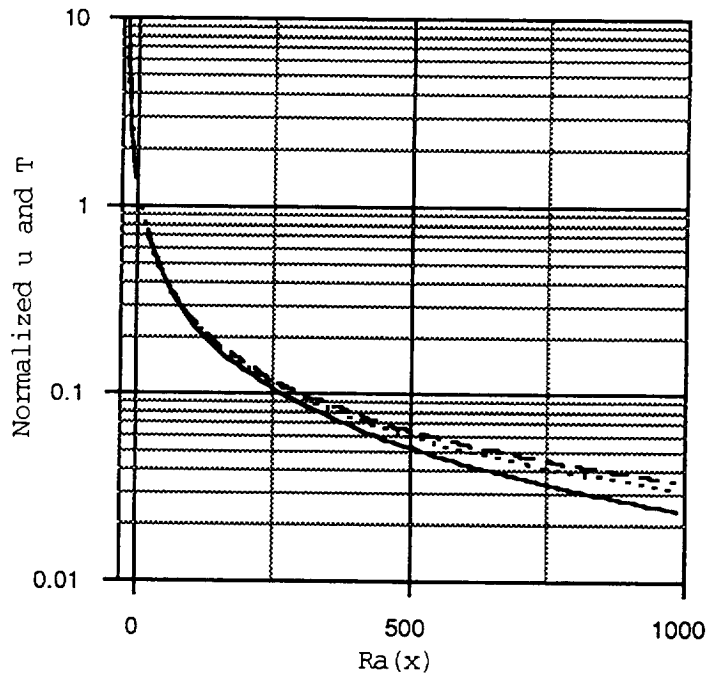

Fig. 1.19 Normalized velocity taken at $\eta = -1/3^{1/2}$ (solid line) and normalized temperature perturbation (taken at $\eta = 1$) as a function of Ra(x). The dotted line is the empirical function $|Ra_{cl}|/(Ra+|Ra_{cl}|)$. Here $Ra = g_x \beta (\Delta T / L) a^4 / \kappa \nu$ and $Ra_c = -31.285$. In terms of the more conventional definition $Ra = g_x \beta (\Delta T / L) W^4 / \kappa \nu$, $Ra_c = -500.56$.

Therefore, it does not appear to be practical to attempt to use an axial acceleration to stabilize microgravity experiments involving dilute systems with low Pr fluids against unwanted low-level transverse accelerations because the Gr(x) required to achieve a large enough Ra(x) to be effective would no longer qualify as a microgravity experiment. There is still considerable benefit to be derived by attempting to orienting the furnace axis along the residual acceleration vector, if for no reason other than to reduce the more critical quasi-steady transverse accelerations.

Non -dilute systems in which the solutal gradient is much larger than the thermal gradient can also be analyzed with this model by substituting compositional change ΔC for ΔT, $\Delta\rho/\rho$ for $\beta\Delta T$, the diffusion coefficient D for κ, and the Schmidt number Sc for the Prandtl number Pr. Thus the thermal Ra, which Gr Pr becomes the solutal Ra which is Gr Sc. Since Sc are generally much larger than Pr for systems of interest, considerably more benefit might be realized by applying a small stabilizing axial acceleration to reduce the effects form uncontrollable transverse accelerations.

The analysis can also be applied to a vertical Bridgman system with a slight tilt in unit gravity. Here the Ra ~ $O(10^4\text{-}10^5)$ and the result is shown in Fig. 1.20 and Fig. 1.21. As the stabilizing field is increased, the residual flow is more or less confined to the vicinity of the walls and the temperature perturbation, when added to the linear unperturbed gradient, forces the resulting isotherms (or iso-concentrates) to be essentially horizontal with respect to the resultant g-vector.

1.7 EFFECTS OF MAGNETIC FIELDS

Unwanted flows in solidification process are often reduced to tolerable levels on earth by the application of strong magnetic fields, either axially of transversely to the melt. Similar benefits can be achieved in microgravity experiments as will be shown. To analyze these effects, it is important to have a more accurate description of the flow in the end regions than could be obtained by the crude assumption suggested earlier in Section 1.41. For configurations in which L >> W (here L is taken as the longest dimension), we have shown that for pure viscous damping the flow in the core region is given by a simple cubic function of the form $\eta^3 - \eta$ where η is the distance from the centerline normalized by a, the half width. If we assume this relation holds over the entire length, we can approximate the stream function by

$$\Psi(\xi,\eta) = \Phi(\xi)\left(\eta^4 - 2\eta^2 + 1\right) \tag{1.85}$$

where ξ is the distance along longest dimension normalized by the half-width, a.

Inserting this into Eq. (1.24) and performing the necessary differentiations along the center line ($\eta = 0$), one obtains an ordinary fourth-order differential equation of the form

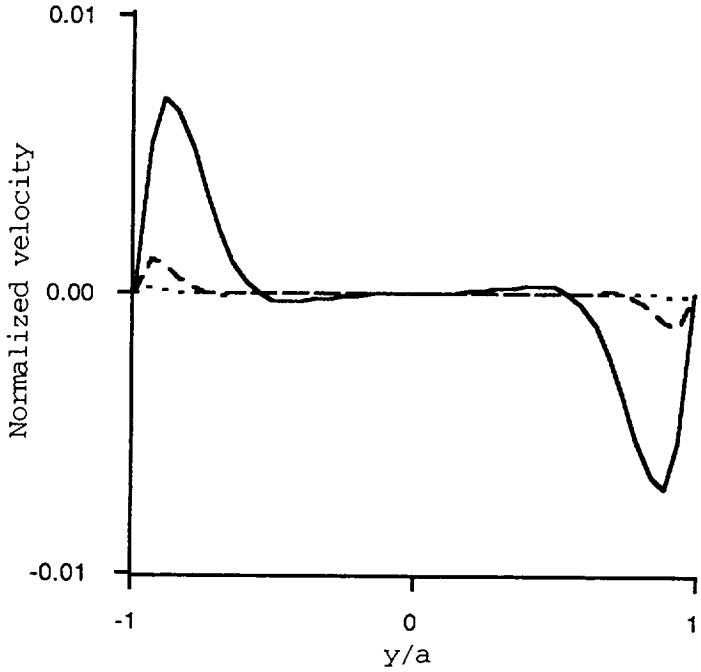

Fig. 1.20 Normalized velocities For Ra = 10^4 (solid line), 10^5 (dashed line), and 10^6 (dotted line). Note that as the Ra increases, the residual flow tends to essentially creep along the walls.

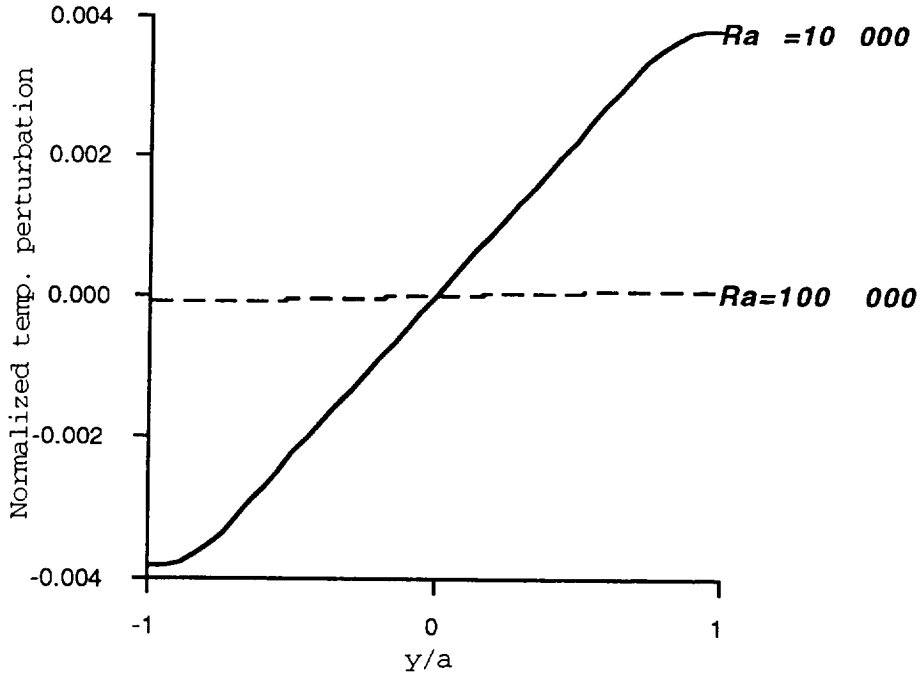

Fig. 1.21 Normalized temperature plot for large Ra. Note the perturbation is nearly a straight line except at the walls. When this perturbation is added to the added to the linear unperturbed gradient, it forces the isotherms to be essentially perpendicular to the resultant g-field.

$$\Phi'''' - b^2\Phi'' + c^4\Phi = G \tag{1.86}$$

where b and c are constants. The G is identified as

$$G = \frac{a^4}{\mu}\left(-g_y\frac{\partial\rho}{\partial x} + g_x\frac{\partial\rho}{\partial y}\right). \tag{1.87}$$

Using Laplace transforms with initial conditions $\Phi(0) = \Phi'(0) = 0$, the solution may be written

$$\Phi(\xi) = \frac{G}{R_1^2 R_2^2} + \frac{G}{R_1^2 - R_2^2}\left[C_1\left(\cosh(R_1\xi) - \cosh(R_2\xi)\right) + \right.$$
$$\left. + C_2\left(\frac{1}{R_1}\sinh(R_1\xi) - \frac{1}{R_2}\sinh(R_2\xi)\right) + \left(\frac{1}{R_1^2}\cosh(R_1\xi) - \frac{1}{R_2^2}\cosh(R_2\xi)\right)\right] \tag{1.88}$$

and

$$\Phi'(\xi) = \frac{G}{R_1^2 - R_2^2}\left[C_1\left(R_1\sinh(R_1\xi) - R_2\sinh(R_2\xi)\right) + C_2\left(\cosh(R_1\xi) - \cosh(R_2\xi)\right) + \right.$$
$$\left. + \left(\frac{1}{R_1}\sinh(R_1\xi) - \frac{1}{R_2}\sinh(R_2\xi)\right)\right] \tag{1.89}$$

where R1 and R2 are the roots of the indicial equation

$$R^4 - b^2R^2 + c^4 = 0 \tag{1.90}$$

given by

$$R_1 = \frac{1}{2}\sqrt{b^2 + 2c^2} + \frac{1}{2}\sqrt{b^2 - 2c^2} \quad \text{and} \quad R_2 = \frac{1}{2}\sqrt{b^2 + 2c^2} - \frac{1}{2}\sqrt{b^2 - 2c^2}. \tag{1.91}$$

If $2c^2 > b^2$, which will generally be the case, the roots will be complex.

The coefficients C1 and C2 are determined by the remaining boundary conditions, i.e. $\Phi(L/a) = \Phi'(L/a) = 0$.

The coefficients may be evaluated from

$$C_1 = \frac{-B_1A_{22} + B_2A_{12}}{A_{11}A_{22} - A_{21}A_{12}} \quad \text{and} \quad C_2 = \frac{-B_2A_{11} + B_1A_{21}}{A_{11}A_{22} - A_{21}A_{12}}$$

where

$$A_{11} = \cosh(R_1 L/a) - \cosh(R_2 L/a)$$

$$A_{12} = \frac{1}{R_1}\sinh(R_1 L/a) - \frac{1}{R_2}\sinh(R_2 L/a)$$

$$A_{21} = R_1 \sinh(R_1 L/a) - R_2 \sinh(R_2 L/a)$$

$$A_{22} = \cosh(R_1 L/a) - \cosh(R_2 L/a)$$

$$B_1 = \frac{1}{R_2^{\,2}} - \frac{1}{R_1^{\,2}} + \frac{1}{R_1^{\,2}}\cosh(R_1 L/a) - \frac{1}{R_2^{\,2}}\cosh(R_2 L/a)$$

$$B_2 = \frac{1}{R_1}\sinh(R_1 L/a) - \frac{1}{R_2}\sinh(R_2 L/a)$$

If $\Phi(\xi)$ is more or less constant away from the end regions, the solution may be simplified considerably by using the semi-infinite approximation; i.e., Φ and Φ' must remain finite as $x \to \infty$. To enforce this condition, the hyperbolic functions with their complex arguments were expanded into real and imaginary parts and the coefficients C1 and C2 were chosen so that the positive exponential terms vanished. Writing the complex roots $R_1 = \alpha + i\,\beta$ and $R_2 = \alpha - i\,\beta$ so that $\alpha = (R_1 + R_2)/2$ and $\beta = i\,(R_1 - R_2)/2$, the resulting expression is obtained;

$$\Phi(\xi) = G\frac{\left[1-\left(\frac{\alpha}{\beta}\sin(\beta\xi)+\cos(\beta\xi)\right)e^{-\alpha\xi}\right]}{\alpha^4+2\alpha^2\beta^2+\beta^4} = \frac{G}{c^4}\left[1-\left(\frac{\alpha}{\beta}\sin(\beta\xi)+\cos(\beta\xi)\right)e^{-\alpha\xi}\right]. \tag{1.92}$$

In cases involving large aspect ratios and where the semi-infinite approximation is not appropriate, it is more convenient to take the origin at the center of the slot and require that $\Phi(L/2) = \Phi'(L/2) = \Phi(-L/2) = \Phi'(-L/2) = 0$. Now the solution can be written

$$\Phi(\xi) = \frac{G}{R_1^{\,2}R_2^{\,2}} + \frac{G}{R_1^{\,2}-R_2^{\,2}}\left\{\left(C_1+C_2R_1^{\,2}+\frac{1}{R_1^{\,2}}\right)\cosh(R_1\xi) - \left(C_1+C_2R_2^{\,2}+\frac{1}{R_2^{\,2}}\right)\cosh(R_2\xi)\right\} \tag{1.93}$$

$$\Phi'(\xi) = \frac{G}{R_1^{\,2}-R_2^{\,2}}\left\{\left(C_1R_1+C_2R_1^{\,3}+\frac{1}{R_1}\right)\sinh(R_1\xi) - \left(C_1R_2+C_2R_2^{\,3}+\frac{1}{R_2}\right)\sinh(R_2\xi)\right\} \tag{1.94}$$

Again the coefficients must be found from

$$C_1 = \frac{B_1 A_{22} - B_2 A_{12}}{A_{11} A_{22} - A_{21} A_{12}} \text{ and } C_2 = \frac{-B_1 A_{21} + B_2 A_{11}}{A_{11} A_{22} - A_{21} A_{12}}$$

where now

$$A_{11} = \cosh(R_1 L/2a) - \cosh(R_2 L/2a)$$

$$A_{12} = R_1^2 \cosh(R_1 L/2a) - R_2^2 \cosh(R_2 L/2a)$$

$$A_{21} = R_1 \sinh(R_1 L/2a) - R_2 \sinh(R_2 L/2a)$$

$$A_{22} = R_1^3 \sinh(R_1 L/2a) - R_2^3 \sinh(R_2 L/2a)$$

$$B_1 = \frac{1}{R_1^2} - \frac{1}{R_2^2} - \frac{1}{R_1^2}\cosh(R_1 L/2a) + \frac{1}{R_2^2}\cosh(R_2 L/2a)$$

$$B_2 = -\frac{1}{R_1}\sinh(R_1 L/2a) + \frac{1}{R_2}\sinh(R_2 L/2a)$$

Having found the stream function as a function of ξ and η, the u and v may be found by

$$u(\xi,\eta) = -\frac{1}{a}\frac{\partial \Psi(\xi,\eta)}{\partial \eta} \text{ and } v(\xi,\eta) = \frac{1}{a}\frac{\partial \Psi(\xi,\eta)}{\partial \xi}.$$

1.7.1 No Magnetic Field

To test the validity of this method for obtaining an approximate solution to the biharmonic equation, the method will first be applied to two cases involving viscous dissipation terms; one in which the aspect ratio is unity, and the second in which the aspect ratio is large. Putting the stream function given by Eq. (1.85) into Eq. (1.24), we can identify $b^2 = 8$ and $c^4 = 24$. Therefore, $R_1 = 2.109 + i\ 0.6704$ and $R_2 = 2.109 - i\ 0.6704$.

Case 1 - Square cell with differentially heated sides.

W = L = 10 cm, $\Delta T = 10$ °C, $\beta = 10^{-5}$/deg, g = 980 x10^{-6}, $\nu = 3.46 \times 10^{-3}$ cm^2/sec g II to L. $\partial\rho/\partial y = \beta \Delta T / W$, G = 0.00177.

The results are shown below:

	Approximate result	Numerical result
$\hat{\Psi}$	2.90 x10^{-5} cm^2/sec	3.58 x10^{-5} cm^2/sec
$\hat{u}$	8.93 x10^{-6} cm/sec	1.12 x10^{-5} cm/sec
$\hat{v}$	9.02 x10^{-6} cm/sec	1.12 x10^{-5} cm/sec

The approximate solution gives only fair results for the case of L = W since the assumption that the stream function has the same functional form over the entire length obviously breaks down in the corner regions. The maximum stream function is low by 19%, as is the maximum vertical velocity $\hat{v}$. The maximum horizontal velocity $\hat{u}$, is low by 20%.

Case 2 - Vertical slot with differentially heated side walls.

W = 2 cm, L = 10 cm, ΔT = 10 °C, $\beta = 10^{-5}$/deg, g = 980 x10^{-6}, $\nu = 3.46\text{x}10^{-3}$ cm^2/sec, g II to L. $\partial\rho/\partial y = \beta\Delta T/W$ and G = 1.416x10^{-5}. The results are now:

	Approximate result	Numerical result
$\hat{\Psi}$	5.90 x10^{-7} cm^2/sec	5.99x10^{-7}cm^2/sec
$\hat{u}$	9.08 x10^{-7} cm/sec	9.16 x10^{-7} cm/sec
$\hat{v}$	4.96 x10^{-7} cm/sec	5.60 x10^{-7} cm/sec

The maximum value of the stream function is in excellent agreement as is the maximum vertical velocity, $\hat{u}$. There is some disagreement in the maximum horizontal velocity, $\hat{v}$, which can be attributed to the approximations used to obtain the $\Phi(x)$. However the approximation is only off by 11%.

The accuracy of the approximation can be assessed by examining the residual field shown in Fig. 1.22 . The normalized residuals were obtained by inserting the assumed solution back into Eq. (1.24), performing the indicated differentiations to evaluate the left-hand side at each point, and normalizing the result by dividing by the driving term. As can be seen, the only regions in which the approximation is in serious error is in the corners. This does not seem to significantly affect the overall accuracy based on comparison with numerical results (although the residuals obtained from numerical computations show a similar pattern), but it does explain why the approximate solution is more accurate for the larger aspect ratios.

1.7.2 Effect of Strong Magnetic Fields

The body force on an element of fluid in a magnetic field can be written

$$\mathbf{F} = \sigma\mathbf{B}\times(\mathbf{B}\times\mathbf{v}) = \sigma\left[(\mathbf{B}\bullet\mathbf{v})-(\mathbf{B}\bullet\mathbf{B})\mathbf{v}\right].$$

In two-dimensions this becomes

$$F_x = \sigma\left[-B_y^2 v_x + B_x B_y v_y\right]$$
$$F_y = \sigma\left[-B_x^2 v_y + B_x B_y v_x\right]$$

Adding this contribution to the body force terms in the momentum equation,

$$-\frac{\partial p}{\partial x} + \mu\frac{\partial^2 u}{\partial x^2} + \mu\frac{\partial^2 u}{\partial y^2} + \rho g_x - \sigma u B_y^2 + \sigma v B_x B_y = 0$$
$$-\frac{\partial p}{\partial y} + \mu\frac{\partial^2 v}{\partial x^2} + \mu\frac{\partial^2 v}{\partial y^2} + \rho g_y - \sigma v B_x^2 + \sigma u B_x B_y = 0$$

Introducing the stream function, cross differentiating, and subtracting to eliminate the pressure terms as was done in deriving Eq. (1.24), we get

$$\mu\left(\frac{\partial^4\Psi}{\partial x^4} + 2\frac{\partial^4\Psi}{\partial x^2\partial y^2} + \frac{\partial^4\Psi}{\partial y^4}\right) + \frac{\partial\rho}{\partial x}g_y - \frac{\partial\rho}{\partial y}g_x - \sigma\left(\frac{\partial^2\Psi}{\partial x^2}B_x^2 + \frac{\partial^2\Psi}{\partial y^2}B_y^2 + 2\frac{\partial^2\Psi}{\partial x\partial y}B_x B_y\right) = 0$$

Case 3 - Vertical slot with differentially heated side walls and a strong vertical magnetic field. Let the temperature distribution be given by $\Delta Tx/W$. Introducing scaled coordinates $\xi = x/a$ and $\eta = y/a$ (**g** taken along the negative x-axis) and using the Boussinesq approximation, the equation for the stream function becomes

$$\frac{\partial^4\Psi}{\partial\xi^4} + 2\frac{\partial^4\Psi}{\partial\xi^2\partial\eta^2} + \frac{\partial^4\Psi}{\partial\eta^4} - \frac{\beta\Delta T}{W}\frac{g_x a^4}{\nu} - Ha^2\frac{\partial^2\Psi}{\partial^2\xi} = 0 \qquad (1.96)$$

where the Hartmann number is defined as

$$Ha^2 = \frac{\sigma B_x^2 a^2}{\rho_0 \nu}.$$

Since the magnetic field does not interact with flow in the vertical direction, we can assume the core flow will have the same form as before, hence $\Psi(\xi,\eta)$ can be written in the form $\Phi(\xi)(\eta^4 - 2\eta^2 - 1)$. Putting this back into Eq. (1.96) and performing the required differentiation, we identify $b^2 = 8+Ha^2$ and $c^2 = 24^{1/2}$. If $Ha^2 >> 1$, both R_1 and R_2 will be real, but $R_1 >> 1$ while $R_2 << 1$. This can cause some computational difficulty in determining the coefficients using the method prescribed above because of the large exponential values involved. Therefore some algebraic manipulation is required. Since $R_2 << 1$, Eq. (1.93) and (1.94) can be expanded about $R_2 = 0$ to obtain

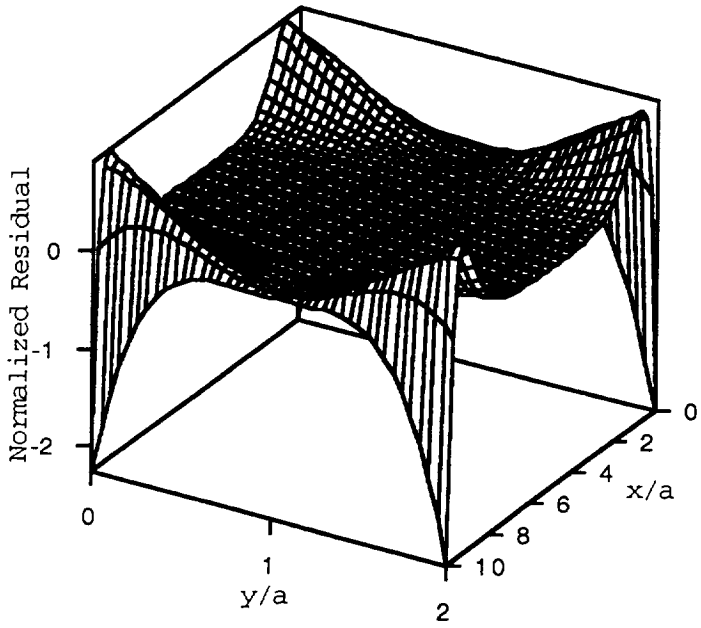

Fig. 1.22 Plot of stream function residuals for Case 2. The approximate solution is reasonably good over the bulk of the field, but does break down in the corners.

$$\Phi(\xi) = \frac{G}{R_1^2}\left[\left(\frac{\xi^2}{2}+1\right)+C_1-\left(C_1+C_2R_1^2+\frac{1}{R_1^2}\right)\cosh(R_1\xi)\right]+O(R_2) \quad (1.97)$$

$$\Phi'(\xi) = \frac{G}{R_1^2}\left[\xi-\left(C_1+C_2R_1^2+\frac{1}{R_1^2}\right)R_1\sinh(R_1\xi)\right]+O(R_2) \quad (1.98)$$

where G is given by

$$G = -\frac{\beta\Delta T}{W}\frac{g_x a^4}{\nu} = \frac{Gr\nu}{16}.$$

The coefficients C_1 and C_2 are determined by requiring $\Phi(\xi_0) = \Phi'(\xi_0) = 0$ at $\xi_0 =$ L /2 a. This yields

$$\Phi(\xi) = \frac{G}{2R_1^3}\left[\frac{R_1\left(\xi_0^2-\xi^2\right)\sinh(R_1\xi_0)+2\xi_0\left(\cosh(R_1\xi)-\cosh(R_1\xi_0)\right)}{\sinh(R_1\xi_0)}\right] \quad (1.99)$$

and

$$\Phi'(\xi) = \frac{G}{R_1^2}\left[\frac{\xi_0\sinh(R_1\xi)-\xi\sinh(R_1\xi_0)}{\sinh(R_1\xi_0)}\right] \quad (1.100)$$

where $R_1 = Ha + \sqrt{24}/Ha + O(Ha^{-2}) \approx Ha$, $Ha >> 1$.

The horizontal velocity (in this case flow in the y-direction) is obtained from

$$v(\xi,\eta) = \frac{\partial\Psi}{\partial x} = \frac{1}{a}\Phi'\left(\eta^4-2\eta^2+1\right) \quad (1.101)$$

and the vertical velocity (in this case flow in the x-direction) is

$$u(\xi,\eta) = -\frac{\partial\Psi}{\partial y} = \frac{4}{a}\Phi\left(\eta-\eta^3\right) \quad (1.102)$$

For W = 2 cm, L 10 cm, G = 14.16, Ha =$2860^{1/2}$, the results are :

	Approximate result	Numerical result
$\hat{\Psi}$	0.0620 cm²/sec	0.0660 cm²/sec
$\hat{u}$	0.0953 cm/sec	0.115 cm/sec
$\hat{v}$	0.0248 cm/sec	0.0256 cm/sec

The stream function is shown in Fig. 1.23. The effect of the vertical field is to round off the stream function along the centerline as can be seen better in the profile along $\eta = 0$ shown in Fig. 1.24. Note that the stream function appears to approach the end walls at a finite slope, even though its derivative is zero at the wall. The effect of this is seen in the velocity profile shown in Fig. 1.25 which shows the maximum velocity occurring almost adjacent to the end wall.

From Eq. (1.99), it may be seen that for $R_1 >> \xi_0$, the stream function will have a maximum value of

$$\hat{\Psi} = \frac{G}{2\,Ha^2}\left(\frac{L}{W}\right)^2 = \frac{Gr\,\nu}{32Ha^2}\left(\frac{L}{W}\right)^2 = \frac{\rho_0 g\beta\Delta T W}{8\sigma B^2}\left(\frac{L}{W}\right)^2. \tag{1.104}$$

The maximum vertical velocity is obtained from Eq. (1.102)

$$\hat{u} = \frac{8}{3\sqrt{3}}\frac{\hat{\Psi}}{a} = \frac{Gr}{6\sqrt{3}\,Ha^2}\frac{\nu}{W}\left(\frac{L}{W}\right)^2 = \frac{2\rho_0 g\beta\Delta T}{3\sqrt{3}\,\sigma B^2}\left(\frac{L}{W}\right)^2. \tag{1.105}$$

Differentiating Eq. (1.100), we see that the maximum velocity horizontal velocity occurs at $\eta = 0$ and when $\cosh(R_1\xi) = \sinh(R_1\xi_0)/R_1\xi_0$ or $\xi = \xi_0 - \ln(R_1\xi_0)/R_1\xi_0$. The maximum horizontal velocity can be estimated by extrapolating the slope of the velocity curve to the end which gives

$$\hat{v} = \frac{1}{a^2}\frac{G}{R_2^2}\frac{L}{2} = \frac{Gr}{8Ha^2}\frac{L}{W}\frac{\nu}{W} = \frac{\rho_0 g\beta\Delta T}{2\sigma B^2}\left(\frac{L}{W}\right). \tag{1.105}$$

This last result can also be obtained from the integral theorem. Taking a stream line just inside the walls, the driving term, $\oint \rho\,\mathbf{g}\bullet d\mathbf{s} \approx \rho_0\,\beta\Delta T\,g_x L$. For large Ha, the viscous damping term is negligible compared to the magnetic damping term given by $\oint \sigma B_x^2\,\hat{\mathbf{v}}\bullet d\mathbf{s} \approx \sigma B_x^2\,\hat{v}\,2W$. Equating and solving for $\hat{v}$, gives Eq. (1.105).

Note that both the horizontal and vertical velocity is independent of length scale for $Ha >> 1$.

This formulation is also applicable to the case of a horizontal field applied to a horizontal slot with a linear thermal gradient along the length L. This configuration would roughly describe a Bridgman furnace with an axial field subjected to transverse accelerations. In this case

$$G = \frac{g_y\,\beta\Delta T a^4}{\nu L} = \frac{Gr\,\nu}{16}\frac{W}{L}$$

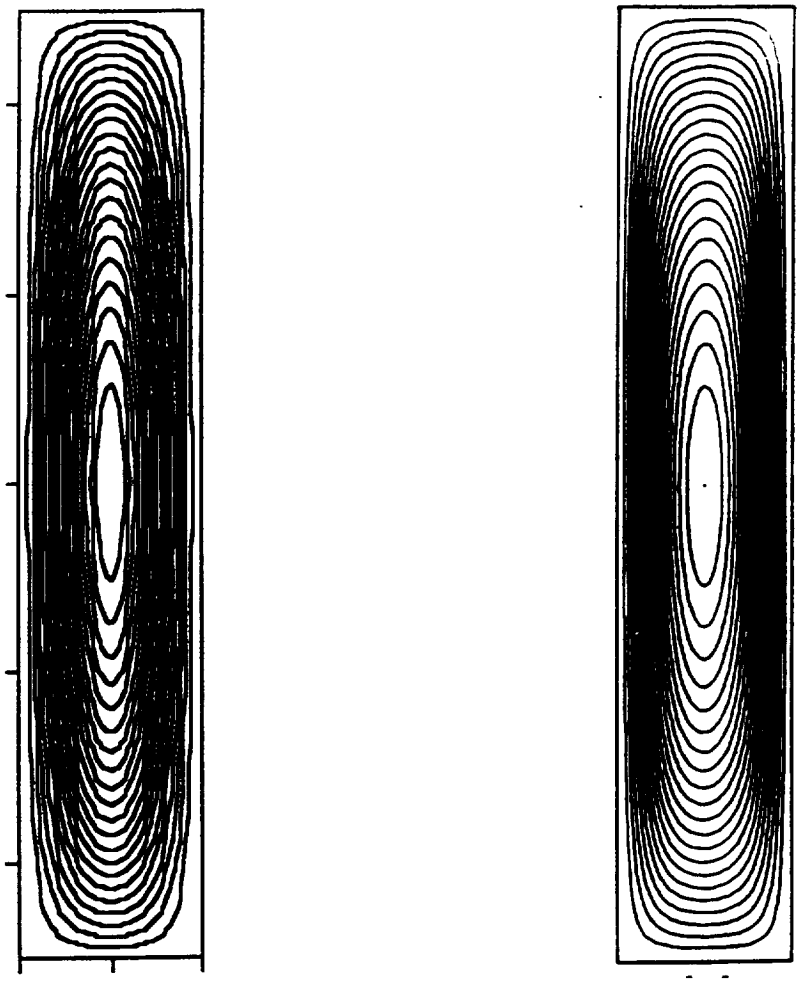

Fig. 1.23. Streamlines for Case 3 in which a strong magnetic field is applied vertically. The approximate result is on the left and the numerical result is on the right

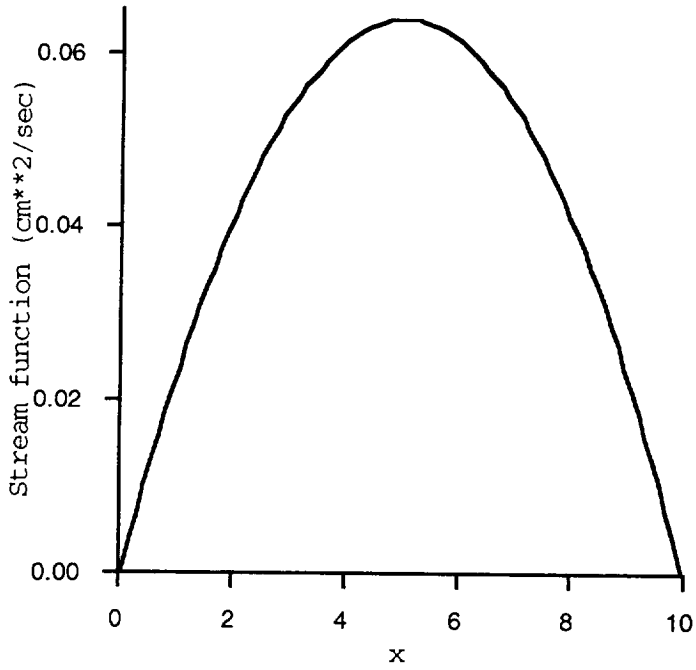

Fig. 1.24. Stream function along $\eta = 0$ for Case 3.

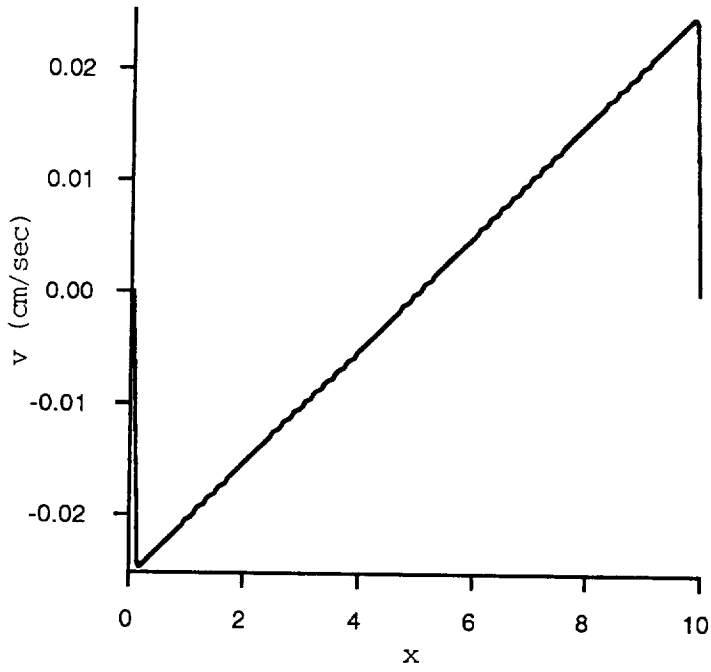

Fig. 1.25 Horizontal velocity profile along $\eta = 0$ for Case 3.

and the above results would be multiplied by W/L which accounts for the reduced thermal gradient which is now $\Delta T/L$ instead of $\Delta T/W$. In this case, $\hat{u}$ is the maximum horizontal velocity and $\hat{v}$ is the maximum vertical velocity.

Case 4 - Narrow vertical slot with differentially heated side walls and a strong horizontal field magnetic field. The stream function equation, Eq. 1.95) simplifies to

$$\mu\left(\frac{\partial^4\Psi}{\partial x^4}+2\frac{\partial^4\Psi}{\partial x^2\partial y^2}+\frac{\partial^4\Psi}{\partial y^4}\right)-\frac{\partial\rho}{\partial y}gx-\sigma\frac{\partial^2\Psi}{\partial y^2}B_y{}^2=0.$$

Let the temperature distribution be given by $\Delta Tx/W$. Introducing scaled coordinates $\xi = x/a$ and $\eta = y/a$, taking **g** along the negative x -axis and using the Boussinesq approximation as before, this becomes

$$\frac{\partial^4\Psi}{\partial\xi^4}+2\frac{\partial^4\Psi}{\partial\xi^2\partial\eta^2}+\frac{\partial^4\Psi}{\partial\eta^4}-\frac{\beta\Delta T}{W}\frac{g_x a^4}{\nu}-Ha^2\frac{\partial^2\Psi}{\partial^2\eta}=0 \qquad (1.106)$$

where the square of the Hartmann number is

$$Ha^2=\frac{\sigma B_y{}^2a^2}{\rho_0\nu}$$

For an infinite vertical slot, the ξ-derivatives may be ignored and the η dependence of the stream function is given by

$$\frac{\partial^4\psi}{\partial\eta^4}-Ha^2\frac{\partial^2\psi}{\partial\eta^2}=G \text{ where } G=-\frac{\beta\Delta T}{W}\frac{ga^4}{\nu}. \qquad (1.107)$$

With the usual B. C., $\psi(\pm1)=\psi'(\pm1)=0$, the solution is

$$\psi(\eta)=G\left[\frac{\cosh(Ha\,\eta)-\cosh(Ha)}{Ha^3\sinh(Ha)}-\frac{\eta^2-1}{2Ha^2}\right]. \qquad (1.108)$$

Now an approximate solution for $\Psi(\xi,\eta)$ is assumed to be of the form $\Psi(\xi,\eta)=\phi(\xi)\psi(\eta)$ so that the equation for the stream function may be written

$$\phi\frac{\partial^4\psi}{\partial\eta^4}\Big)_{\eta=0}+2\frac{\partial^2\phi}{\partial\xi^2}\frac{\partial^2\psi}{\partial\eta^2}\Big)_{\eta=0}+\frac{\partial^4\phi}{\partial\xi^4}\psi_{(\eta=0)}-Ha^2\phi\frac{\partial^2\psi}{\partial\eta^2}\Big)_{\eta=0}=G. \qquad (1.109)$$

Evaluating the derivatives of ψ at $\eta = 0$ and rearranging we get

$$\phi'''' \left[\frac{1-\cosh(Ha)}{Ha^3 \sinh(Ha)} + \frac{1}{2Ha^2}\right] + 2\,\phi'' \left[\frac{1}{Ha \sinh(Ha)} - \frac{1}{Ha^2}\right] + [1]\phi = 1 \qquad (1.110)$$

If Ha >>1, this equation can be simplified by retaining only the highest order terms in Ha,

$$\phi'''' \left[\frac{1}{2\,Ha^2}\right] + 2\,\phi'' \left[-\frac{1}{Ha^2}\right] + [1]\phi = 1$$

or

$$\phi'''' - 4\,\phi'' + \left[2Ha^2\right]\phi = 2Ha^2 \,. \qquad (1.111)$$

This has the same form as Eq. (1.86) with $b^2 = 4$, $c^4 = 2\,Ha^2$, and $G = 2\,Ha^2$. Thus the solution can be written as the product of Eq. (1.108) and either Eq. (1.88) or Eq. (1.93) in which

$$R_1 = \frac{\sqrt{4+2(2Ha^2)}}{2} + \frac{\sqrt{4-2(2Ha^2)}}{2}$$

$$R_2 = \frac{\sqrt{4+2(2Ha^2)}}{2} - \frac{\sqrt{4-2(2Ha^2)}}{2}.$$

For W = 2 cm, L 10 cm, G = 14.16, Ha $=2860^{1/2}$, the comparison of the above approximate calculation and the numerical results are shown.

	Approximate result	Numerical result
$\hat{\Psi}$	0.00248 cm^2/sec	0.00249 cm^2/sec
$\hat{u}$	0.00493 cm/sec	0.00496 cm/sec
$\hat{v}$	0.00947 cm/sec	0.00935 cm/sec

Here the agreement is quite good, the difference being only a few percent.

The stream function is shown in Fig. 1.26. Note that the flow is rectalinear along most of the length of the ampoule and that the turning points are pushed very close to the ends. Since all of the change in the stream function takes place over a very short distance in the x-direction, it is possible to the much simpler semi-infinite formulation to obtain the same results. From Eq. (1.92), we can write the ξ-dependent part of the stream function as

$$\phi(\xi) = 1 - \left(\frac{\alpha}{\beta}\sin(\beta\xi) + \cos(\beta\xi)\right) e^{-\alpha\xi}$$

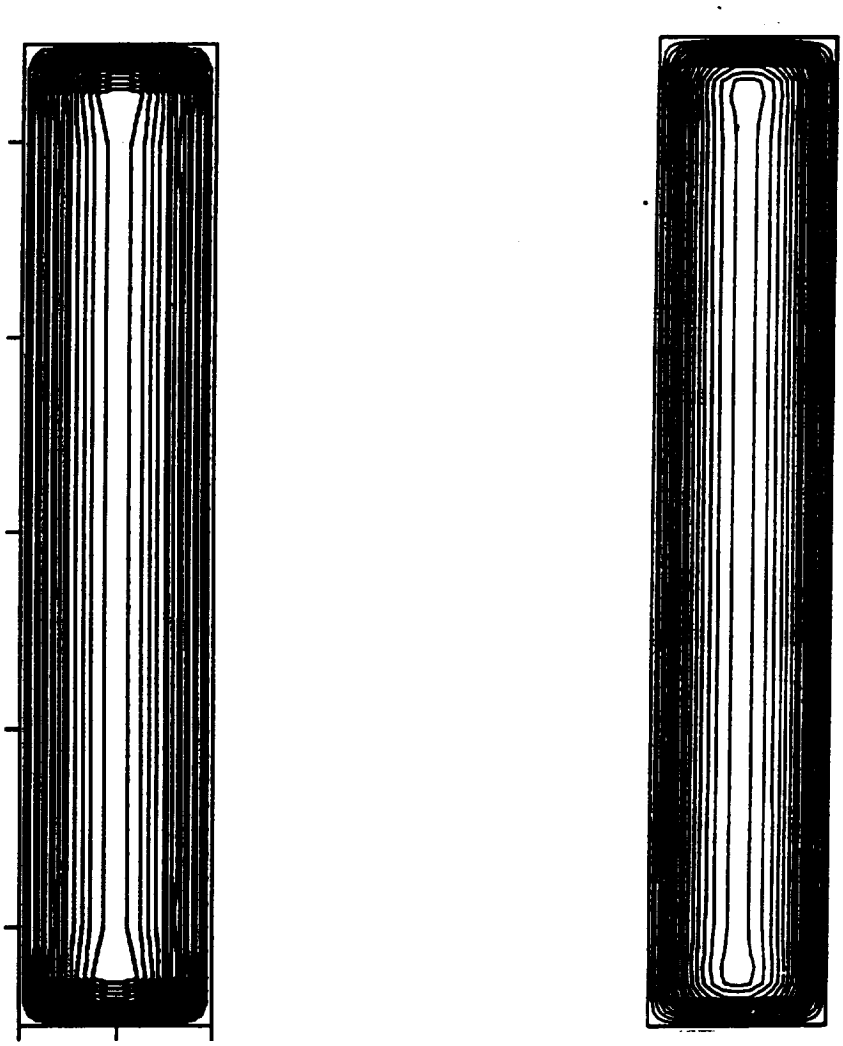

Fig. 1.26 Streamlines for Case 4 in which a strong horizontal field is applied to a vertical slot with differentially heated side walls. The approximate result is on the left and the numerical result is on the right

where α = Re(R1) and β = Im(R1). When $\xi > 1/\alpha$, this function quickly approaches 1. The magnitude of the stream function then is determined by $\psi(\eta)$ given by Eq. (1.108). Since this function has a maximum at $\eta = 0$, the maximum value of Ψ is

$$\hat{\Psi} = G\left[\frac{1-\cosh(Ha)}{Ha^3\sinh(Ha)} + \frac{1}{2Ha^2}\right] \xrightarrow[Ha>>1]{} \frac{G}{2Ha^2} = \frac{Gr\nu}{32Ha^2} = \frac{\rho_0 g\beta\Delta T W}{8\sigma B^2}. \quad (1.112)$$

Actually, the peak value of Ψ is slightly higher than this because of the small over-shoot when the pre-exponential factor goes negative before it is killed by the exponential term. This is reflected in the slight bulging of the stream function at the turning point. This effect is also seen in the numerical computations.

The horizontal velocity along $\eta = 0$ is given by

$$v(\xi,0) = -\frac{\partial\Psi}{\partial x} = -\frac{G}{a}\left[\frac{1-\cosh(Ha)}{Ha^3\sinh(Ha)} + \frac{1}{2Ha^2}\right]\left[\frac{\alpha^2+\beta^2}{\beta}\sin(b\xi)e^{-\alpha\xi}\right]. \quad (1.113)$$

For Ha >> 1, $\alpha \approx \beta \approx Ha^{/2}/2^{1/4}$ and the last term reaches a maximum value of 0.622 α at $\alpha\,\xi \approx 0.7$. Therefore, the maximum v near the ends is

$$\begin{aligned}\hat{v} &= \frac{G}{2aHa^2}0.622\alpha = \frac{G}{Ha^{3/2}W}0.523 = 0.0322\frac{Gr\nu}{Ha^{3/2}} \\ &= 0.0925\rho_0\beta\Delta T\left(\frac{\rho_0^3 W^2}{\nu\sigma^3 B^6}\right)^{1/4}\end{aligned} \quad (1.114)$$

The maximum vertical velocity along the side walls away from the ends is obtained by differentiating $\psi(\eta)$ to obtain

$$u = \frac{G}{aHa^2}\left[\frac{\sinh(Ha\,\eta)}{\sinh(Ha)} - \eta\right]. \quad (1.115)$$

Again the maximum will occur just inside $\eta = 1$ and can be estimated by extrapolating the slope of Eq. (1.115) to $\eta = 1$ which yields

$$\hat{u} = \frac{G}{aHa^2} = \frac{Gr\nu}{8Ha^2} = \frac{\rho_0 g\beta\Delta T}{2\sigma B^2}. \quad (1.116)$$

This result can also be easily obtained using the integral theorem by equating the driving term, $\rho_0 g_x \beta \Delta T L$ to the magnetic damping term, $\sigma B_y^2 \hat{u}(2L)$ and solving for $\hat{u}$ scales as $W^{1/2}$.

1.8 SUMMARY

Methods for approximating buoyancy-driven flows in various geometries have been developed which are applicable over a wide range of Gr, Pr, and aspect ratio; limited only by the requirement that the Re be sufficiently low (typically Re $\leq$ 3000) so that the flows remain laminar. The most general result from Eq. (1.53) can be expressed for L < 2 W in the form

$$\hat{u} = \frac{16}{3\sqrt{3}}\frac{\hat{\Psi}}{W};\quad \hat{v} = \frac{8\hat{\Psi}}{3\sqrt{3}}\frac{1}{\delta_{eff}} = \frac{8}{3\sqrt{3}}\frac{\hat{\Psi}}{W}\left(\frac{32}{27\sqrt{3}}\frac{\hat{\Psi}}{\kappa}+\frac{2W}{L}\right), \tag{1.117}$$

where

$$\frac{\hat{\Psi}}{\kappa}\left[\left(\frac{16}{27\sqrt{3}}\frac{\hat{\Psi}}{\kappa}\right)^3+\left(\frac{W}{L}\right)^3\right]+\frac{\hat{\Psi}}{\kappa}\frac{L}{W} = \frac{GrPr}{384} \qquad \text{for Pr} > 1$$

$$\frac{\hat{\Psi}}{\kappa}\left[\left(\frac{16}{27\sqrt{3}}\frac{\hat{\Psi}}{\kappa}\right)+\left(\frac{W}{L}\right)\right]^3+\frac{\hat{\Psi}}{\kappa}\frac{L}{W} = \frac{GrPr}{384} \qquad \text{for Pr} < 1.$$

In these expressions, L always refers to the horizontal dimension and W to the vertical dimension. The Gr is defined as $g \beta \Delta T W^3/\nu^2$.

For L > 2 W, these become

$$\hat{u} = \frac{16}{3\sqrt{3}}\frac{\hat{\Psi}}{W};\quad \hat{v} = \frac{8\hat{\Psi}}{3\sqrt{3}}\frac{1}{\delta_{eff}} = \frac{8}{3\sqrt{3}}\frac{\hat{\Psi}}{W}\left(\frac{32}{27\sqrt{3}}\frac{\hat{\Psi}}{\kappa}+1\right) \tag{1.118}$$

where

$$\frac{\hat{\Psi}}{\kappa}\left[\left(\frac{16}{27\sqrt{3}}\frac{\hat{\Psi}}{\kappa}\right)^3+\left(\frac{1}{2}\right)^3\right]+\frac{\hat{\Psi}}{\kappa}\frac{L}{W} = \frac{GrPr}{384} \qquad \text{for Pr} > 1$$

$$\frac{\hat{\Psi}}{\kappa}\left[\left(\frac{16}{27\sqrt{3}}\frac{\hat{\Psi}}{\kappa}\right)+\left(\frac{1}{2}\right)\right]^3+\frac{\hat{\Psi}}{\kappa}\frac{L}{W} = \frac{GrPr}{384} \qquad \text{for Pr} < 1.$$

Note that for large Gr Pr, these reduce to

$$\hat{\Psi} = \frac{9}{32}\left(6\sqrt{3}\right)^{1/4}(GrPr)^{1/4}\kappa = 0.5049\left(6\sqrt{3}\right)^{1/4}(GrPr)^{1/4}\kappa \tag{1.119}$$

$$\hat{u} = \frac{3}{16}\left(\frac{2\sqrt{3}}{3}GrPr\right)^{1/4}\frac{\kappa}{W} = 0.1943\left(\frac{Gr}{Pr^3}\right)^{1/4}\frac{\nu}{W} \tag{1.120}$$

$$\hat{v} = \frac{\left(6\sqrt{3}\right)^{1/2}}{12}(GrPr)^{1/2}\frac{\kappa}{W} = 0.2686\left(\frac{Gr}{Pr}\right)^{1/2}\frac{\nu}{W}. \tag{1.121}$$

This last equation has the form of the scaling law suggested by Ostrach for Gr >1, Pr >1, but should apply also for Pr <1 provided Gr Pr >>1. The scaling laws proposed by Ostrach, Eq. (1.2) and (1.3), actually apply to flow in the vicinity of a vertical heated wall in a semi-infinite fluid which is different from the case of flow in a box with differentially heated end walls in which the streamlines are closed. An approximate solution to the vertical heated wall was obtained by Goldstein [12]and can be written as

$$\hat{v} = \frac{5.17}{3}\left(\frac{Gr}{Pr+20/21}\right)^{1/2}\frac{\nu}{W} \tag{1.122}$$

which would scale as Eq. (1.2) in the limit of small Pr. That this scaling does not apply to the flow in a completely filled box is seen in Fig. 1.16 which plots log of Re^2 vs. log of Pr for constant Gr. Although the data for small Pr do not exactly fall
on the 1/Pr slope or on the line predicted by Eq. (1.53), they certainly do not scale as 1/(Pr+20/21).

For Gr Pr < O(10^2), these reduce to

$$\hat{\Psi} = \frac{1}{384}\left(\frac{W/L}{1+(W/L)^4}\right)GrPr\kappa \qquad W/2 \le L \le 2\,W \tag{1.123}$$

$$\hat{u} = \frac{16}{3\sqrt{3}}\frac{\hat{\Psi}}{W} = \frac{GrPr}{72\sqrt{3}}\frac{\kappa}{L}\left(\frac{1}{1+W^4/L^4}\right) = \frac{Gr}{72\sqrt{3}}\frac{\nu}{L}\left(\frac{1}{1+W^4/L^4}\right) \tag{1.124}$$

$$\hat{v} = \frac{16}{3\sqrt{3}}\frac{\hat{\Psi}}{L} = \frac{GrPr}{72\sqrt{3}}\frac{\kappa}{L}\left(\frac{W/L}{1+W^4/L^4}\right) = \frac{Gr}{72\sqrt{3}}\frac{\nu}{L}\left(\frac{W/L}{1+W^4/L^4}\right) \tag{1.125}$$

and for L > 2 W they become

$$\hat{\Psi} = \frac{GrPr\kappa}{384}\left(\frac{W/L}{1+W/8L}\right) \tag{1.126}$$

$$\hat{u} = \frac{16}{3\sqrt{3}}\frac{\hat{\Psi}}{W} = \frac{GrPr}{72\sqrt{3}}\frac{\kappa}{L}\left(\frac{1}{1+W/8L}\right) = \frac{Gr}{72\sqrt{3}}\frac{\nu}{L}\left(\frac{1}{1+W/8L}\right) \qquad (1.127)$$

$$\hat{v} = \frac{8}{3\sqrt{3}}\frac{\hat{\Psi}}{W} = \frac{GrPr}{144\sqrt{3}}\frac{\kappa}{L}\left(\frac{1}{1+W/8L}\right) = \frac{Gr}{144\sqrt{3}}\frac{\nu}{L}\left(\frac{1}{1+W/8L}\right). \qquad (1.128)$$

Note that these equations are slightly different from those derived earlier for the case of small Ra (Eq. (1.30) and (1.34)). This is because in the previous derivation the peak value of the stream function given by Eq. (1.25) was seen to give satisfactory results for all values of W/L and its shape was modified to account for the turning points being nearer the end for L > 2 W. The stream function used in the above set of equations was derived from the integral theorem by equating the viscous drag around the system to the driving force. The difference is small, however; amounting to a maximum of only 3% for L = 3 W. In both cases, the $\hat{u}$ converges to the value obtained for maximum flow in a one-dimensional horizontal slot as L >> W.

Robertson and Spradley [6] numerically computed the maximum velocity generated by a horizontal temperature gradient in 2-dimensional chambers having a variety of shapes. They expressed their results in terms of a dimensionless velocity v* defined as

$$v^* = \hat{v}\frac{128\nu}{g\beta\Delta T d^2}$$

where d is the diameter of a circle of equivalent area. For a vertical slot, L = W/2 and Ra = 1000, they obtain v* = 0.39. This would correspond to

$$\hat{v} = 0.39\frac{g\beta\Delta T}{128\nu}\frac{4}{\pi}\frac{W^2}{2} = \frac{g\beta\Delta T W^2}{515.54\nu}.$$

Eq. (1.125) gives

$$\hat{v} = \frac{Gr\nu}{72\sqrt{3}}\frac{2}{W}\frac{2}{17} = \frac{g\beta\Delta T W^2}{530.01\nu}.$$

For a horizontal slot, L = 2 W and Ra = 1000, they obtain v* = 0.18. This would correspond to

$$\hat{v} = 0.19\frac{g\beta\Delta T}{128\nu}\frac{4}{\pi}2W^2 = \frac{g\beta\Delta T W^2}{264.55\nu}.$$

Eq. (1.124) gives

$$\hat{u} = \frac{Gr}{72\sqrt{3}} \frac{\nu}{L} \frac{1}{(1+1/16)} = \frac{g\beta\Delta T W^2}{265.00\nu}.$$

An upper limit for the time constant for transient flows was obtained by integrating around the streamline corresponding to the maximum steady state flow (Eq. (1.39)). For the case of small Ra, this becomes

$$\tau = \frac{W^2}{36\nu}\left[\frac{1+(W/L)^2}{1+(W/L)^4}\right] = \frac{L^2}{36\nu}\left[\frac{1+(L/W)^2}{1+(L/W)^4}\right]. \qquad (1.129)$$

Note that this function is symmetric with the exchange of L and W. The function reduces to $W^2/36\ \nu$ for L = W and for L >> W and has a maximum value of 1.2 $W^2/36\ \nu$ for L = 1.6 W. The behavior is the same for L < W with the role of L and W exchanged.

Robertson and Spradley also computed the response times for their various configurations which they expressed as a dimensionless time $\tau^* = t\ \nu/ R^2$, R being the radius of a circle of equivalent area. They obtain τ^* =.04 for the horizontal slot with L = 2 W, and τ^* =.03 for the vertical slot with W = 2 L. These would correspond to

$$\tau = \frac{L^2}{52.36\nu}; \quad W = 2L$$

and

$$\tau = \frac{W^2}{39.27\nu}; \quad L = 2W.$$

These compare favorably with Eq. (1.129) which yields

$$\tau = \frac{W^2}{30.6\nu} = \frac{L^2}{30.6\nu}; \quad L = 2W \text{ and } W = 2L.$$

Eq. (1.129) assumed the maximum velocity was always at $\xi = 1/3^{1/2}$, as was discussed previously. Taking a more realistic value of ξ to account for the fact that the maximum velocity occurs closer to x ξ = 1 would improve the agreement. The fact that the model fails to predict a difference between the time constants for the horizontal and vertical slot is probably due to the assumption made in deriving Eq. (1.39) that the positions of maximum flow, L' and W', stood in the same ratio as L and W. Even so, Eq. (1.129) is accurate to within a factor of 2, which should be sufficiently accurate for order of magnitude estimates of the time constants.

The response to periodic accelerations may be approximated by rewriting Eq. (1.18) as

$$|\tilde{v}| = \bar{v}\left|\frac{1}{(1+i\omega\tau)}\right| = \bar{v}\frac{1}{(1+\omega^2\tau^2)^{1/2}} \tag{1.130}$$

where $|\tilde{v}|$ is the amplitude of the velocity fluctuations produced by a periodic acceleration whose magnitude would produce a steady state velocity $\bar{v}$. The accuracy of this expression is also limited by the accuracy of τ, but should be within a factor of 2.

The effects of stabilizing and destabilizing axial gradients were considered. It was shown that the effect of such gradients on the flows induced by transverse accelerations could be represented empirically by

$$\frac{\hat{u}(Ra(x))}{\hat{u}_0} = \frac{500}{500+Ra(x)} \tag{1.131}$$

where $\hat{u}(Ra(x))$ is the maximum flow velocity with the stabilizing (or destabilizing) axial gradient, and $\hat{u}_0$ is the maximum velocity without the axial gradient. The Raleigh number here is defined as

$$Ra(x) = \frac{g_x \beta \Delta T a^4}{\kappa \nu \lambda}$$

for dilute systems stabilized by thermal gradients, and

$$Ra(x) = \frac{g_x (\Delta\rho/\rho) a^4}{D \nu \lambda}$$

for non-dilute systems stabilized by solutal gradients. In these definitions, λ refers to the e-folding length of the axial gradient and Ra >0 is taken to be a stabilizing gradient. From this, it is seen that microgravity experiments involving low Pr fluids are relatively insensitive to the effects of axial gradients since |Ra| will generally be << 500. Non-dilute systems, especially those with large Sc, could benefit from a stabilizing gradient, and, consequentially, could be seriously affected by a destabilizing gradient.

Finally, the effects of magnetic fields was assessed. It was shown that the application of a magnetic field can dramatically lower the convective flow velocity, even in a microgravity experiment where the flows are already extremely low. Axial fields are less effective than transverse fields for reducing flows, but have the advantage of being symmetric and also tend to keep the axial flows further from the solidification interface which lessens the radial segregation. The maximum horizontal flow velocity in a horizontal channel with a linear axial

temperature gradient in the presence of a strong axial magnetic field (Ha >> 1) is given by

$$\hat{u} = \frac{Gr}{6\sqrt{3}\,Ha^2}\frac{L}{W}\frac{\nu}{W} = \frac{2\rho_0 g\beta\Delta T}{3\sqrt{3}\,\sigma B^2}\left(\frac{L}{W}\right). \tag{1.132}$$

Note that the flow velocity is independent of length scale. The ratio of velocities with and without the magnetic field can be written as

$$\frac{\hat{u}_B}{\hat{u}_0} = \frac{\left(\frac{Gr}{6\sqrt{3}\,Ha^2}\frac{L}{W}\frac{\nu}{W}\right)}{\frac{Gr}{72\sqrt{3}}\frac{\nu}{L}} = \frac{12}{Ha^2}\left(\frac{L}{W}\right)^2; \quad Ha^2 >> 1 \tag{1.133}$$

Having obtained the flow is only half the battle for most applications. There is still the question of the transport. As stated previously, the heat and mass transport can be characterized by the thermal and solutal Peclet numbers which are useful to estimate whether transport is dominated by convection or conduction, but there is no simple way to directly relate, for example, the solutal Peclet number to the degree of radial segregation in a solidifying ingot to the solutal Peclet number because of the complex interplay of a number of length scales including the diffusion length, the ampoule radius, and the turning point of the flow. This problem is the subject of the next two parts of this report.

1.9 REFERENCES

1. S. Ostrach, Ann. Rev. Fluid Mech. 14 (1982) 313-345
2. D. Langbein and C. Tiby, Allowable g-levels for Microgravity Payloads, Final Report for ESA, Contract No.5.504/83/F/FS(SC), Battelle Frankfurt, September 1984
3. The author is indebted to Dr. Glen Roberts of Roberts Associates, Arlington, VA for suggesting this formal proof.
4. R. B. Bird, W.E. Stewart, and E. N. Lightfoot, Transport Phenomena, John Wiley and Sons, New York, 1960, pp 297-300
5. R. F. Dressler, J. Crystal Growth 54 (1981) 523-533
6. S. J. Robertson and L. W. Spradley, Acta Astronautica,13 (1986) 727-733
7. D. E. Cormack, L. G. Leal and J. Imberger, J. Fluid Mech. 65 (1974) 209-231
8. D. E. Cormack, L. G. Leal and J. H Seinfeld, J. Fluid Mech. 65 (1974) 231-246
9. J. Imberger, J. Fluid Mech. 65 (1974) 2247-260
10. A. Bejan and C. L. Tien, Int. J. Heat Mass Transfer, 21 (1978)701-708
11. G. K. Batchelor, Quarterly Appl. Math. XII (1954) 209-233

SECTION 2

RADIAL SEGREGATION IN BRIDGMAN GROWTH FROM LOW-LEVEL AXIAL ACCELERATIONS

2.1 INTRODUCTION

The importance of being able to control buoyancy-driven convective flows in order to grow compositionally homogeneous crystals from the melt has been recognized for some time and has motivated a number of experiments using the reduced environment of orbiting spacecraft to minimize such flows [1]. However, it has been found that even the reduction of the effective acceleration of gravity by some 4 to 6 orders of magnitude is not necessarily sufficient to eliminate compositional inhomogeneities in the growth of such crystals and the very slow flows driven by the residual accelerations inherent in a low Earth orbit spacecraft can be significant in crystal growth.

A number of attempts have been made to estimate the magnitude and effects of such flows by scaling analysis. Camel and Favier identified various convective regimes based on the relative magnitudes of the growth Peclet number versus the product of the Grashoff and Schmidt numbers [2]. Langbein and Tiby developed criteria for allowable accelerations for a number of fluid and solidification processes based on scaling analyses [3]. Alexander and Rosenberger compare the results of the various scaling analyses to numerical simulations and find that such scaling arguments can at best only provide a rough order of magnitude estimate because of their neglect of the multi-dimensionality of the physical growth process [4].

Chang and Brown were the first to actually compute the buoyancy-driven convective flows in vertical Bridgman crystal growth of a dilute binary system and predict their effect on melt interface shape and dopant distribution [5]. Since then a number of researchers have utilized various computational fluid dynamics (CFD) techniques to extend this work to non-dilute systems, to non-axisymmetric systems, and even to systems subjected to time-varying accelerations [6-9]. These studies have provided much useful information on the role convection plays in such growth processes, and have been particularly valuable in the planning of experiments to be conducted in the reduced gravity environment of an orbiting spacecraft in order to control or eliminate some of the unwanted effects of buoyancy-driven convection. Perhaps the most surprising result of these studies is the extent that one must reduce the effective acceleration level in order to actually achieve diffusion limited growth, even for systems of modest dimensions.

One difficulty with the CFD approach is that a calculation only addresses a particular case and gives little insight into the role of the various parameters involved such as growth rate, the thermal profile, and the thermophysical properties of the candidate materials. An approximate analytical solution that is a function of these parameters would also be desirable to elucidate the complex

interplay of the multiple length scales involved and to allow various sensitivity analyses to be performed without the expenditure of large amounts of computer time.

In this section approximate analytical solutions are sought that capture the essential elements of the more definitive CFD models, but still remain mathematically tractable. In this first attempt, the analysis will be restricted to plane-front solidification of a dilute system in the vertical, thermally stable configuration (acceleration vector aligned along the furnace axis antiparallel to the thermal gradient) [10]. These approximate solutions may be compared with the CFD solutions at specific points in parameter space in order to determine the validity of some of the approximate methods that were required to obtain the solutions. They then may be used to extend the modelling over a much broader range of parameter space than could be reasonably carried out using CFD techniques.

2.2 ANALYSIS

The full set of coupled partial differential equations that govern the fluid flow, heat transport, and mass transport in even the simplest Bridgman crystal growth system indeed presents a formidable challenge. However, for many problems of practical interest it is possible to make a number of simplifying assumptions that allow closed form approximate solutions that are accurate to well within an order of magnitude that can provide insight to the roles of the various parameters.

For example, since many of the materials of interest have low Prandtl numbers, heat is transported by conduction for low to modest convective flows in research scale growth systems. For dilute systems, the concentration field does not directly influence the flow field. This decoupling allows the flows to be estimated from an invariant thermal field, and the concentration field to be computed from the resulting flow field. Furthermore, since in Bridgman growth, the growth ampoule usually has a large aspect (length to diameter) ratio, a good estimate of the axial component of the convective flows can be made using a one-dimensional model which has a simple closed form solution.

The solution of the mass transport equation is more difficult in that it is necessary to solve this partial differential equation in two dimensions in order to obtain the radial dopant distribution. For weak convective flows, however, it is possible to use perturbation theory to simplify the mass transport equation so that a solution can be obtained by separation of variables. Also, this analysis will be restricted to plane-front solidification to simplify the boundary conditions at the melt-solid interface. As was shown by Corriel and Sekerka [11], it is essential to arrange the thermal profile to achieve nearly a flat interface if radial segregation is to be minimized.

In order to estimate the flows in a vertical Bridgman crystal growth system, consider the one-dimensional flow in a vertical cylindrical ampoule with a radial temperature distribution given by

$$T(r) = T_0 + \langle \Delta T \rangle \ (r/a)^2 \tag{2.1}$$

where T_0 is the temperature at r = 0 and $\langle \Delta T \rangle$ is the average radial temperature difference.

The momentum equation is

$$\rho \frac{\partial \vec{v}}{\partial t} + \rho(\vec{v} \cdot \nabla)\vec{v} = -\nabla p + \mu \nabla^2 \vec{v} + \rho \vec{g} \ . \tag{2.2}$$

In cylindrical coordinates the Laplacian operator for the z-component is

$$\nabla^2 \vec{v} = \frac{1}{r} \frac{\partial w}{\partial r} + \frac{\partial^2 w}{\partial r^2} \ .$$

Following the example given in [13], the inertial term, which is second order for the small velocities considered here, is neglected, the density is expanded about some reference temperature T_1, i.e.,

$$\rho = \rho_1 + \frac{\partial \rho}{\partial T}(T - T_1) = \rho_1 - \rho_1 \beta \left[(T_0 - T_1) + \langle \Delta T \rangle (r/a)^2 \right] \tag{2.3}$$

where β the thermal expansion coefficient, and the pressure gradient is assumed to be due solely to the weight of the fluid, ie. $\nabla p = - g \rho_1$ where g is taken as positive downward. For steady acceleration, eq. (2.2) becomes

$$\frac{\partial^2 w}{\partial r^2} + \frac{1}{r} \frac{\partial w}{\partial r} + \frac{g \beta \langle \Delta T \rangle}{\nu} \left[(r/a)^2 + \frac{(T_0 - T_1)}{\langle \Delta T \rangle} \right] = 0 \ . \tag{2.4}$$

The boundary conditions are:

$$w(a) = 0 \quad \text{(no slip at the walls)},$$

$$\int_0^a w(r)\, r\, dr = 0 \quad \text{(no net flow)},$$

and symmetry about r = 0. The conservation of flow boundary condition requires the quantity

$$\frac{(T_0 - T_1)}{\langle \Delta T \rangle} = -\frac{1}{3}$$

and the steady state solution becomes

$$w(r) = -\frac{g\,\beta\langle \Delta T \rangle\, a^2}{48\,\nu}\left[1 - 4(r/a)^2 + 3(r/a)^4\right] . \tag{2.5}$$

From this solution it may be seen that the maximum convective velocity will occur at r = 0 and may be written

$$\hat{w} = -\frac{g\,\beta\langle \Delta T \rangle\, a^2}{48\,\nu} . \tag{2.6}$$

This could also be written as Re = Gr/48, from which it may be seen that simple scaling based on dimensional analysis over-predicts the maximum velocity by considerably more than an order of magnitude.

Let us now consider the effect of the buoyancy-driven flows on the radial segregation in the sample. The mass transport is governed by,

$$u\frac{\partial C}{\partial r} + (w - v_g)\frac{\partial C}{\partial z} = D\frac{1}{r}\frac{\partial}{\partial r}\left(r\frac{\partial C}{\partial r}\right) + D\frac{\partial^2 C}{\partial z^2} \tag{2.7}$$

where v_g is the growth velocity and u and w are the buoyancy-driven velocities in the reference system moving with the growth velocity.

For plane-front solidification, the boundary conditions are given by

$$C(r,\infty) = C_\infty \quad \text{for all } r$$

and

$$D\left(\frac{\partial C}{\partial z}\right)_{z=0} + v_g(1 - k)C(r,0) = 0 \quad \text{for all } r.$$

In the absence of buoyancy-driven convective flows, the solution becomes

$$C_z = \left[(1 - k)e^{-z/\delta} + k\right]\frac{C_\infty}{k} \quad \text{where} \quad \delta = D/v_g . \tag{2.8}$$

Now consider the case of convective flows characterized by a velocity $\hat{w} << v_g$. A solutal Peclet number may be defined as $P_e = \hat{w}\,\delta/D$ where δ is the diffusion

length of the solute boundary layer at the growth interface. Since $\delta = D/v_g$, the Peclet number becomes just the ratio of the characteristic convective velocity to the growth velocity, or $P_e = \hat{w} / v_g$. The velocities u and w can be expressed as

$$u = v_g P_e \tilde{u}(x,r) \tag{2.9}$$

and

$$w = v_g P_e \tilde{w}(r,z) \tag{2.10}$$

where $\tilde{u}$ and $\tilde{w}$ denote the dimensionless convective velocity components that have been scaled by the Peclet number. Also let the concentration field be given by

$$C(r,z) = C_z + P_e \tilde{C}(r,z) . \tag{2.11}$$

Putting these back into eq. (2.7) yields

$$P_e^2 v_g \tilde{u} \frac{\partial \tilde{C}}{\partial r} - v_g \frac{\partial C_z}{\partial z} - P_e v_g \frac{\partial \tilde{C}}{\partial z} + P_e v_g \tilde{w} \frac{\partial C_z}{\partial z} + P_e^2 v_g \tilde{w} \frac{\partial \tilde{C}}{\partial z} =$$

$$= P_e \frac{D}{r} \frac{\partial \tilde{C}}{\partial r} + P_e D \frac{\partial^2 \tilde{C}}{\partial r^2} + D \frac{\partial^2 C_z}{\partial z^2} + P_e D \frac{\partial^2 \tilde{C}}{\partial z^2} \tag{2.12}$$

and the boundary condition becomes

$$D \left(\frac{\partial C_z}{\partial z}\right)_{z=0} + P_e D \left(\frac{\partial \tilde{C}}{\partial z}\right)_{z=0} + v_g (1 - k) C_z(o) + P_e v_g (1 - k) \tilde{C}(r,0) = 0 \quad \text{for all r.}$$

The zeroth order terms in P_e in eq. (2.12) are the terms in the unperturbed equation that is satisfied by C_z. Dropping the terms of second order in P_e, the first order perturbation in composition, $\tilde{C}$ must satisfy

$$v_g \frac{\partial \tilde{C}}{\partial z} - v_g \tilde{w} \frac{\partial C_z}{\partial z} + \frac{D}{r} \frac{\partial \tilde{C}}{\partial r} + D \frac{\partial^2 \tilde{C}}{\partial r^2} + D \frac{\partial^2 \tilde{C}}{\partial z^2} = 0 \tag{2.13}$$

with the boundary condition

$$D \left(\frac{\partial \tilde{C}}{\partial z}\right)_{z=0} + v_g (1 - k) \tilde{C}(r,0) = 0 \quad \text{for all r.}$$

Dividing through by v_g and identifying $\delta = D / v_g$,

$$\frac{\partial \tilde{C}}{\partial z} - \tilde{w}\frac{\partial C_z}{\partial z} + \frac{\delta}{r}\frac{\partial \tilde{C}}{\partial r} + \delta\frac{\partial^2 \tilde{C}}{\partial r^2} + \delta\frac{\partial^2 \tilde{C}}{\partial z^2} = 0 \ . \qquad (2.14)$$

Let us write

$$\tilde{w} = \tilde{w}_r \tilde{w}_z \qquad (2.15)$$

where $\tilde{w}_r$ and $\tilde{w}_z$ are respectively functions of r and z only. Let us also assume $\tilde{C}$ can be written as

$$\tilde{C}(r,z) = \tilde{w}_r \ f(z) \ e^{-z/\delta}. \qquad (2.16)$$

The derivatives are

$$\frac{\partial \tilde{C}(r,z)}{\partial z} = \tilde{w}_r \left(f'(z) - \frac{f(z)}{\delta}\right) e^{-z/\delta} \ , \quad \frac{\partial^2 \tilde{C}(r,z)}{\partial z^2} = \tilde{w}_r \left(f''(z) - \frac{2\ f'(z)}{\delta} + \frac{f(z)}{\delta^2}\right) e^{-z/\delta} \ .$$

Putting these back into eq. (14) and dividing through by $\tilde{w}_r$ f(z) exp(-z/d),

$$\frac{1}{f(z)}\left(f'(z) - \frac{f(z)}{\delta}\right) + \frac{\tilde{w}_z}{f(z)}\frac{(1-k)}{\delta}\frac{C_\infty}{k} + \frac{\delta}{f(z)}\left(f''(z) - \frac{2\ f'(z)}{\delta} + \frac{f(z)}{\delta^2}\right) +$$

$$+ \frac{\delta}{\tilde{w}_r}\left(\frac{1}{r}\frac{d\tilde{w}_r}{dr} + \frac{d^2\tilde{w}_r}{dr^2}\right) = 0. \qquad (2.17)$$

We see that the variables separate provided

$$+ \frac{1}{\tilde{w}_r}\left(\frac{1}{r}\frac{d\tilde{w}_r}{dr} + \frac{d^2\tilde{w}_r}{dr^2}\right) = - s^2 \qquad (2.18)$$

where s is the separation constant.

Eq. (18), can be written

$$r^2\frac{d^2\tilde{w}_r}{dr^2} + r\frac{d\tilde{w}_r}{dr} + r^2 s^2 \tilde{w}_r = 0 \ . \qquad (2.19)$$

This is a form of Bessel's equation whose solution is

$$\tilde{w}_r = E\ J_0(r\,s) + F\ Y_0(r\,s) \ . \qquad (2.20)$$

Since Y_0 blows up at the origin, F must be set to zero. It is necessary to introduce a series solution to represent the velocity function, $\tilde{w}_r$ given by eq. (5),

$$\tilde{w}_r = \sum_{n=1}^{\infty} E_n J_0(r s_n) = \left[1 - 4 (r/a)^2 + 3 (r/a)^4\right] \qquad (2.21)$$

where the coefficients E_n are computed using the orthogonality properties of the Bessel functions, i.e.,

$$E_n = \frac{2}{a^2 J_1^2(a s_n)} \int_0^a r \left(1 - 4 (r/a)^2 + 3 (r/a)^4\right) J_0(r s_n)\, dr$$

which after performing the integration becomes

$$E_n = - \frac{64}{J_1(a s_n)} \left[\frac{1}{(a s_n)^3} - \frac{6}{(a s_n)^5}\right] . \qquad (2.22)$$

The separation constants s_n are the zeros of J_0 divided by the radius of the ampoule, ie. $s_1 = 2.405/a$, $s_2 = 5.520/a$, $s_3 = 8.654/a$, $s_4 = 11.792/a$, etc. It was found that 4 terms were sufficient to give a reasonable representation of $\tilde{w}_r$. The coefficients are $E_1 = 0.332$, $E_2 = 0.898$, $E_3 = -0.335$, and $E_4 = 0.161$.

Now f(z) can be found by solving the ordinary differential equation,

$$f_n''(z) - \frac{f_n'(z)}{\delta} - s_n^2 f(z) = - \frac{(1-k)}{\delta^2} \frac{C_\infty}{k} \tilde{w}_z \quad . \qquad (2.23)$$

In order to proceed, we must somehow specify $\tilde{w}_z$ which, of course, could not be determined from the 1-D solution of the velocity field. There are several conditions that this function must satisfy in order to represent the actual flow field. For example, $\tilde{w}_z$ should be zero at z = 0, peak at unity at some specified distance from the growth interface, and then eventually die out for large z. The behavior of $\tilde{w}_z$ at large z does not significantly influence the solution near the interface which is the region of interest. The distance at which $\tilde{w}_z$ peaks is the point at which the axial flows begin to be turned by the pressure gradient resulting from the flow encountering the growth interface and will generally be near the point of maximum radial thermal gradient. Further, since u must be zero at z = 0 for all r, from the equation of continuity,

$$\frac{1}{r}\frac{\partial(r\tilde{u})}{\partial r} + \frac{\partial \tilde{w}}{\partial z} = 0 \ ,$$

it is seen that the derivative of $\tilde{w}_z$ as well $\tilde{w}_z$ must vanish at z = 0. Lacking a solution to the two-dimensional momentum equation a function with these properties will be arbitrarily assumed, ie.

$$\tilde{w}_z = \frac{e^2}{4}\left(\frac{z}{\lambda}\right)^2 e^{-z/\lambda} \ . \tag{2.24}$$

Here λ represents the boundary layer thickness of the horizontal or radial flow across the growth interface [14]. The coefficient of eq. (24) is chosen to normalize the expression to unity at 2λ where it achieves its maximum value. This will generally occur where the point at which the radial temperature gradient reaches its maximum value.

For convenience, we write eq. (2.23) as

$$f_n''(z) - \alpha f_n'(z) - s_n^2 f(z) = G z^2 e^{-\beta z}$$

where $a = 1/\delta$, $b = 1/\lambda$, and

$$G = -(1-k)\alpha^2 \beta^2 \frac{e^2}{4}\frac{C_\infty}{k} . \tag{2.25}$$

This ordinary differential equation has a solution given by

$$f_n(z) = A_n z^2 e^{-\beta z} + B_n z e^{-\beta z} + C_n e^{-\beta z} + D_n e^{r_n z} \tag{2.26}$$

where

$$A_n = \frac{G}{\beta^2 + \alpha\beta - s_n^2} \ , \quad B_n = \frac{2G(2\beta+\alpha)}{(\beta^2 + \alpha\beta - s_n^2)^2} \ , \quad C_n = \frac{2G(3\beta^2 + 3\alpha\beta + \alpha^2 + s_n^2)}{(\beta^2 + \alpha\beta - s_n^2)^3}$$

and

$$r_n = \frac{\alpha}{2}\left(1 - \sqrt{1 + 4\, s_n^2/\alpha^2}\right) \ . \tag{2.27}$$

The coefficients D_n are arbitrary constants to be determined from the boundary conditions. (Since the perturbation must die out for large z, the other arbitrary set of arbitrary constants, i.e. the coefficients of the exponential of the positive values of r_n, must be set to zero.)

The perturbed solution can now be written as

$$\tilde{C}(r,z) = \sum_{n=1}^{4} E_n J_0(r\, s_n)\left[(A_n z^2 + B_n z + C_n)\, e^{-z/\lambda} + D_n\, e^{r_n z}\right] e^{-z/\delta} \quad . \qquad (2.28$$

The arbitrary constants are found from the boundary condition at z = 0, ie.,

$$D\left(\frac{\partial \tilde{C}}{\partial z}\right)_{z=0} + v_g(1 - k)\tilde{C}(r,0) = 0 \quad \text{for all r.} \qquad (2.29)$$

Dividing through by D $\tilde{w}_r$ and identifying $D/v_g = \delta = 1/\alpha$, this becomes

$$\sum_{n=1}^{4} E_n J_0(r\, s_n)\left[B_n - (\beta + \alpha)C_n + (r_n - \alpha)D_n\right] + \alpha(1-k)\sum_{n=1}^{4} E_n J_0(r\, s_n)(C_n + D_n) = 0 \, .$$

Collecting terms,

$$\sum_{n=1}^{4} E_n J_0(r\, s_n)\left[B_n - \beta C_n + r_n D_n - k\,\alpha(C_n + D_n)\right] = 0 \, . \qquad (2.30)$$

In order for this to hold for all r, the bracket term must vanish for each n. This requires

$$D_n = \frac{-B_n + (\beta + k\,\alpha)C_n}{r_n - k\,\alpha} \quad . \qquad (2.31)$$

We can now calculate $\tilde{C}(r,z)$ from eq. (16) and in turn determine the concentration field using eq. (11).

2.3 DISCUSSION

Having obtained an analytic solution, even with a restricted range of applicability, it is now possible to make a number of general conclusions about the interplay of the various materials and processing parameters and their effect on radial segregation.

To begin, since the maximum or characteristic convective velocity depends directly on the acceleration in the range over which the first order perturbation theory is valid, the perturbation to the concentration field, and hence the degree of radial segregation, is linearly related to the applied acceleration.

The magnitude of the perturbation at the growth interface depends on the value of the functions $f_n(z)$ evaluated at $z = 0$. From eq. (26)

$$f_n(0) = C_n + D_n \tag{2.32}$$

which can be written using eq. (2.27) and (2.31)

$$f_n(0) = \frac{2\,G}{r_n - k\alpha}\left[\frac{\beta^3 + r_n\left(3\,\beta^2 + 3\,\alpha\,\beta + \alpha^2 + s_n^2\right) + s_n^2\left(3\,\beta + \alpha\right)}{\left(\beta^2 + \alpha\,\beta - s_n^2\right)^3}\right] \cdot \tag{2.33}$$

This rather complicated expression involves the interplay of the three inverse length scales, ie. α, the inverse of the diffusion length; β, the inverse of the boundary layer of the horizontal flow across the growth interface, and s_n, the nth zero of J_0 divided by the radius of the sample. To gain some insight into the roles of these various length scales, it is instructive to consider several limiting cases. If $\alpha << s_n$, $r_n \approx -s_n$ and eq. (2.33) becomes

$$f_n(0) \approx -\frac{2\,G}{s_n}\left[\frac{\beta^3 - s_n^3 + s_n^2\left(3\,\beta + \alpha\right) - s_n\left(3\,\beta^2 + 3\,\alpha\,\beta + \alpha^2\right)}{\left(\beta^2 + \alpha\,\beta - s_n^2\right)^3}\right] \cdot \tag{2.34}$$

Recall from eq. (2.25) that G is given by

$$G = -\left(1 - k\right)\alpha^2\,\beta^2\,\frac{e^2}{4}\,\frac{C_\infty}{k}\,.$$

Using this, eq. (2.34) becomes in the limit of small a (small diameter ampoules in which the diffusion length $\delta >> a$),

$$f_n(0) \approx \frac{C_\infty\,e^2}{2\,k}\left(1 - k\right)\frac{\alpha^2\,\beta^2}{s_n}\left(\frac{\beta - s_n}{\beta^2 - s_n^2}\right)^3, \quad \alpha << s_n\,. \tag{2.35}$$

If β is large compared to s_n,

$$f_n(0) \approx \frac{C_\infty\,e^2}{2\,k}\left(1 - k\right)\frac{\alpha^2}{\beta\,s_n} \quad \text{or} \quad f_n(0) \sim \frac{a\,\lambda}{\delta^2}\,, \quad \alpha << s_n \text{ and } \beta >> s_n\,.$$

If β is comparable to s_n, this becomes

$$f_n(0) \approx \frac{C_\infty e^2}{2k}(1 - k)\frac{\alpha^2 \beta^2}{8 s_n^4} \quad \text{or} \quad f_n(0) \sim \frac{a^4}{\delta^2 \lambda^2}, \quad \alpha << s_n \text{ and } \beta \approx s_n .$$

In the limit of small α and β,

$$f_n(0) \approx \frac{C_\infty e^2}{2k}(1 - k)\frac{\alpha^2 \beta^2}{s_n^4} \quad \text{or} \quad f_n(0) \sim \frac{a^4}{\delta^2 \lambda^2}, \quad \alpha << s_n \text{ and } \beta << s_n .$$

At the other extreme, if $\alpha >> s_n$,

$$f_n(0) \approx -\frac{2G}{k\alpha}\left[\frac{\beta^3 - 3s_n^2 \beta^2/\alpha}{(\beta^2 + \alpha\beta - s_n^2)^3}\right] . \tag{2.36}$$

If β is comparable to or less than s_n, which will generally be the case, this becomes

$$f_n(0) \approx \frac{C_\infty e^2}{2k}(1 - k)\frac{\beta^2}{k\alpha^2} \quad \text{or} \quad f_n(0) \sim \frac{\delta^2}{k\lambda^2} . \tag{2.37}$$

However, if $\beta >> \alpha$,

$$f_n(0) \approx \frac{C_\infty e^2}{2k}(1 - k)\frac{\alpha}{k\beta} \quad \text{or} \quad f_n(0) \sim \frac{\lambda}{k\delta}, \quad \alpha >> s_n \text{ and } \beta >> \alpha .$$

From this analysis several conclusions can be drawn. For slow growth velocities in very small diameter ampoules, the diffusion length can be substantially greater than the ampoule radius, hence $\alpha < s_n$. The n =1 term will then dominate because s_n gets progressively larger with n. If the thermal profile is such that the radial gradients attain their maximum values at a distance comparable to or greater than a, the $f_n(0)$ term will go as the fourth power of the diameter and will be inversely proportional to both the square of the diffusion length and the square of the boundary layer thickness of the radial flow. Physically, this has the effect of lessening the radial concentration gradient by moving the radial flow farther from the solidification interface. Also in the limit of small diameters, the radial back-diffusion terms in eq. (2.14) become more effective in reducing the compositional perturbation driven by $\hat{w}$. Under these circumstances, the perturbation can be reduced by lowering the growth velocity. Even though this increases the Peclet number which multiplies $f_n(0)$, the function $f_n(0)$ goes as the inverse square of d which in turn is inversely proportional to the growth velocity. The net result is that

the radial segregation is directly proportional to growth velocity in this regime. The perturbation may also be reduced by moving the point at which the vertical flow becomes maximum farther from the growth interface, i.e. increase λ. This can be accomplished by lengthening the adiabatic zone between the hot and cold zones of the Bridgman Stockbarger furnace. This also tends to flatten the isotherms in the vicinity of the growth interface and reduces the overall radial thermal gradient which drives the convective flows.

For faster growth systems in larger diameter ampoules, the diffusion length may be small compared to the radius, hence $\alpha >> s_n$. Thermal considerations generally require that the point of maximum radial gradient is comparable to or greater than the radius, thus $\lambda >> \delta$ or $\alpha >> \beta$. Now as seen in eq. (2.37), the $f_n(0)$ no longer depends on the ampoule radius and each term will have the same magnitude. (The series is truncated in this case by the E_n coefficients.) Also the magnitude of the perturbation is increased by the additional factor k in the denominator (assuming k<1). The $f_n(0)$ term will then be proportional to the square of the diffusion length δ and inversely proportional to the square of the horizontal flow boundary layer thickness λ. Physically, this may be understood from the consideration that if $\delta << \lambda$, only a small portion of the concentration build-up at the solidification interface extends into the radial flow field. The perturbation may be lessened by further reducing the diffusion length by increasing the growth velocity, or by moving moving the radial flow field farther from the solidification interface by increasing the length of the adiabatic zone. Since the perturbation term is multiplied by the Peclet number, which is inversely proportional to the growth velocity, the radial segregation will now be proportional to the inverse cube of the growth velocity. It should also be remembered that even though the perturbation term is independent of a, the characteristic convective velocity, hence the Peclet number, and therefore the radial segregation, is proportional to the square of the radius.

2.4 COMPARISON WITH CHANG AND BROWN'S RESULTS

The very simple 1-D calculation for the velocity profile and the first-order perturbation calculation for the resulting concentrations may be checked against the detailed CFD computations carried out by Chang and Brown (C&B) for the flows associated with a dilute alloy system (Ga-doped Ge) in a vertical Bridgman configuration. Chang and Brown characterize their computations in terms of a Rayleigh number defined by

$$Ra = \frac{g\,\beta(T_H - T_C)\,L^3}{\alpha_T\,\nu} \qquad (2.38)$$

where the length of the ampoule L = 2 cm, the radius a = 0.5 cm, the thermal diffusivity α_T = 0.078 cm^2/sec, the kinematic viscosity ν = 0.0013 cm^2/sec, and the

thermal expansivity $\beta = 0.00025$ /K. Values for g and $T_H - T_C$ were not specified, but can be related to the Rayleigh number by inserting these values into eq. (2.38),

$$g\,(T_H - T_C) = 0.0507\ Ra\ \ (cm\ K/sec^2). \qquad (2.39)$$

In the growth of systems such as Ga-doped Ge a typical temperature difference of 200 K is needed between the hot and cold zone to provide sufficient thermal gradient to stabilize the growth interface. Hence a Rayleigh number of 10 would correspond to an acceleration of 2.5 micro-gs.

The quantity needed to evaluate eq. (2.6) is not the maximum temperature difference, but some form of average radial difference $\langle \Delta T \rangle$. It may be seen from the isotherms computed by C&B that the wall temperatures rise from T_C to T_H in a nearly uniform manner over the length of the adiabatic zone, L_a; whereas the temperature along r = 0 rises from T_C to T_H over roughly twice the length of the adiabatic zone. With these observations, a very rough estimate can be made of the average radial temperature gradients by

$$\langle \Delta T \rangle = \frac{1}{2\,L_a} \int_0^{2\,L_a} [T(a,z) - T(0,z)]\,dz = \frac{T_H - T_C}{8}\ . \qquad (2.40)$$

C&B present their flow calculations in terms of stream function. The stream function y is defined such that the velocity vector can be obtained from

$$w = -\frac{1}{r}\frac{\partial \psi}{\partial r} \quad \text{and} \quad u = \frac{1}{r}\frac{\partial \psi}{\partial z}\ . \qquad (2.41)$$

The stream functions obtained by C&B were fit by even order polynomials to assure symmetry about r = 0 and the velocities were determined by differentiation, i.e.,

$$w(r) = 2\,a_2 + 4\,a_4\,r^2 + 6\,a_6\,r^4 \ldots + j\,a_j\,r^{j-2} \qquad (2.42)$$

where a_2, a_4, ... a_j are the coefficients of the j^{th} order terms in the polynomial fit for ψ. Chang and Brown state they used a value of 16 μm/sec for their growth velocity v_g; however, this value seems inconsistent with both the stream function plots and the concentration fields they obtained. For the case of no convection, the growth or translational velocity will contribute $v_g r^2/2$ to the stream function. The maximum dimensionless stream function obtained for this case (taken from their Fig. 2.4) was 0.0003. They scaled length by L and velocity by α_T/L; therefore, their maximum dimensional stream function for this case would be 0.000047 cm^3/sec. At r = 0.5 cm, this would correspond to a translational velocity of 4 μm/sec.

Chang and Brown chose a value of 0.00013 cm^2/sec for their diffusion coefficient. For their stated value of 16 μm/sec for v_g, the diffusion length d would be 0.08 cm. However, their concentration profiles indicate a diffusion length of approximately 0.2 cm which would correspond to a growth velocity of 6.5 μm/sec.

Because of these inconsistencies, it is difficult to make a direct comparison of flow velocities computed from eq. (2.5) with those corresponding to the stream functions presented by C&B. One approach would be to eliminate the scale factor by computing the ratio of convective velocities to translational velocity v_g and then assume various translational velocities in making the comparisons. Table 2.1 shows the comparisons for the maximum convective flow velocities (downward flow at r = 0) after subtracting the translational velocity for the three values of v_g in question.

Table 2.1

Ra	Eq.(5) w(0) (cm/sec)	C&B v_g=4 μm/sec w(0) (cm/sec)	C&B v_g=6.5 μm/sec w(0) (cm/sec)	C&B v_g=16 μm/sec w(0) (cm/sec)
100	-0.00063	-0.0005	-0.0009	-0.002
1000	-0.0063	-0.005	-0.009	-0.02
10000	-0.063	-0.05	-0.09	-0.2
1000000	-6.3	-1.1	-1.79	-4.4

The velocities estimated from eq. (2.5) fall between those computed from C&B's stream function for v_g = 4 μm/sec and 6.5 μm/sec for Rayleigh numbers up to about 10^4. For materials with low Prandtl numbers the heat is transported primarily by conduction at low flow velocities. As the Rayleigh number increases, the isotherms eventually become distorted by the convective flows and at Rayleigh numbers between 10^4 and 10^5 the heat begins to be transported more by convection. At around this point, the velocity will begin to increase as the square root of Ra, as can be seen by the departure of C&B's results from a linear relation with Rayleigh number at Ra = 10^6, and the simple analytical approach used here is no longer valid .

In order to compare the estimates of the radial segregation, the values for the segregation coefficient k, the diffusion coefficient D, and the growth velocity v_g were chosen to match those used in Chang and Brown's calculation. C&B took k = 0.1, D = 0.00013 cm^2/sec, and v_g = 16 μm/sec for However, as stated previously, this value for v_g leads to an inconsistency in the diffusion length in the concentration profiles presented by C&B. Therefore calculations to be used in the comparison were performed with values of v_g = 6.5 μm/sec as well as 16

μm/sec.

The only other parameter needed for the first-order perturbation calculation is the distance 2λ from the interface at which the axial convective velocity attains its maximum value This will occur at the point where the radial temperature gradients are the largest, which usually occurs just above the adiabatic zone. In C&B's work the length of the adiabatic zone was taken to be 0.5 cm and the interface was approximately in the center of the adiabatic zone, hence the adiabatic zone length extended 0.25 cm into the melt. The length 2λ was taken to be 20% above this point or 0.3 cm, thus $\lambda = 0.15$ cm.

With these inputs, the calculated parameters for Ra = 100 and k = 0.1 are given in Table II along with the radial segregation ζ defined as the difference between the maximum and minimum concentration at the interface divided by the unperturbed interfacial concentration.

Table 2.2

	$v_{g.}$ =6.5 μm/sec	$v_{g.}$ =16 μm/sec
vc (μm/sec)	-6.348	-6.348
Pe	-0.977	-0.397
δ (cm)	0.200	0.081
$f_1(0)$	0.3479	0.8828
$f_2(0)$	0.0461	0.1579
$f_3(0)$	-0.0042	-0.0184
$f_4(0)$	0.00077	0.0036
$\tilde{C}(0,0)/C_\infty$	0.1536	0.4365
$C(0,0)/C_\infty$	8.50	8.26
ζ	15.0%	17.3%

The perturbed concentration profile at the interface is shown in Fig. 2.1 and compared with the result obtained by C&B. Notice that the concentration profiles are quite similar except for the shift along the z-axis. Inherent in the first order perturbation approach is the assumption that the perturbation in concentration $\tilde{C}$ could be written

$$\tilde{C}(r,z) = w_r\ f(z)\ e^{-z/\delta}.$$

Since w_r must be zero at r = a (no slip condition), the perturbation must vanish at the wall.

The terms containing the radial velocity which transport the melt from the center of the ampoule to near the wall in the vicinity of the growth interface are second

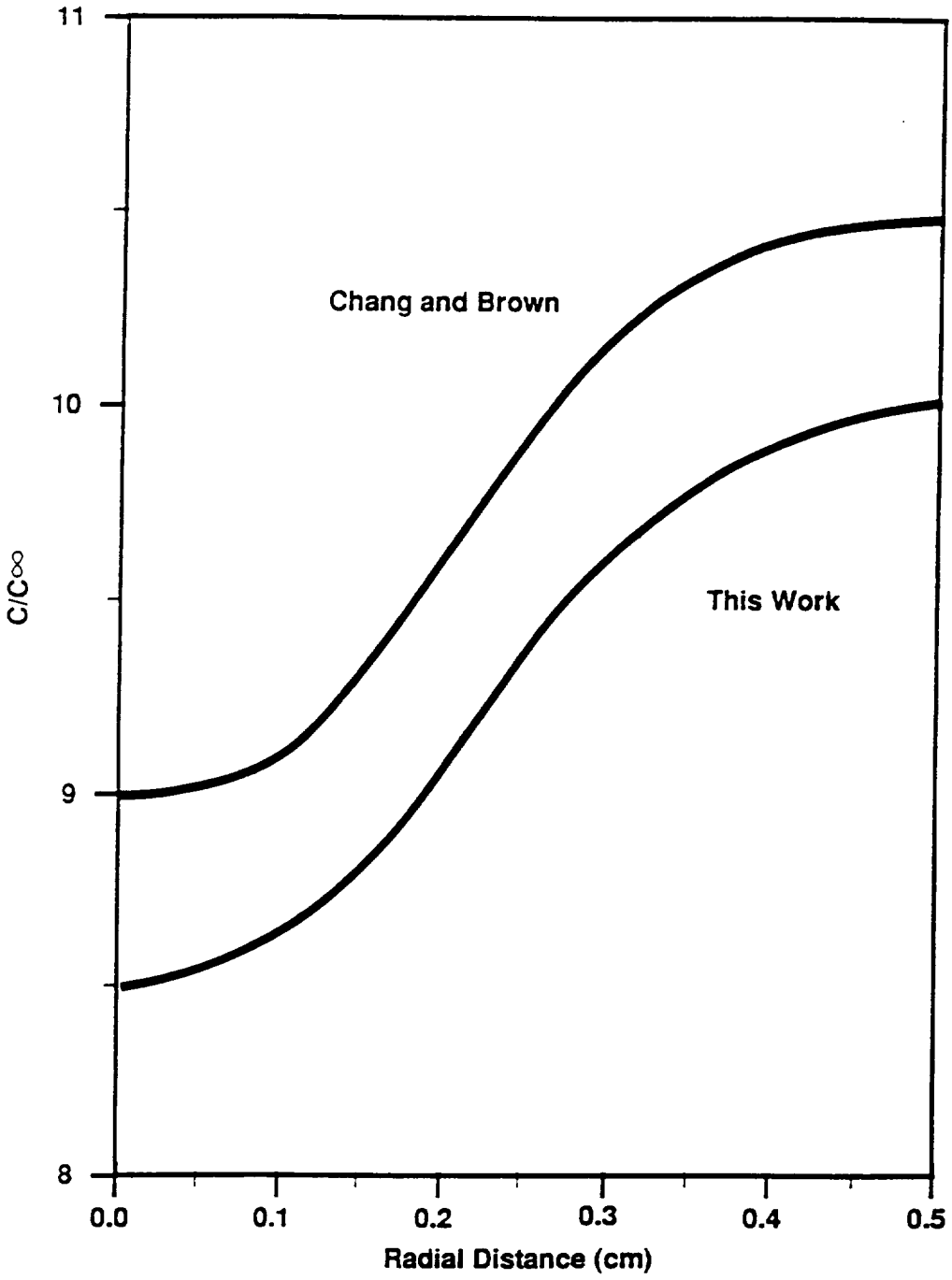

Figure 1. Comparison of the concentration profiles at the solidification interface computed from the analytical mode with those computed numerically by Chang and Brown. The shapes are quite similar; however, the results from the analytical model are displaced. This is the result of the neglect of the second order radial convective transport term in the first order perturbation calculation.

order and were therefore neglected in the first order calculation; thus allowing the variables to be separated. As may be seen in Fig. 2.2, these terms would have had the effect of removing some of the solute-poor melt from the center and transporting it radially to dilute the solute-rich melt near the wall, thus shifting the isoconcentration curves upward along the z-axis.

The error caused by neglecting these terms is not serious for small values of Pe, but for the above case in which the Pe is nearly unity, the first-order perturbation model has clearly exceeded its range of applicability. However, the predicted values of radial segregation from the first order calculation, (15.0%, and 17.3% for the two growth velocities considered) are remarkably close to the value of 14.6% estimated from Fig. 9 in Chang and Brown's work. The reason the first-order calculation continues to give reasonable results is that the radial segregation is computed from the difference between the highest and lowest concentration at the interface, hence would not be significantly affected by a shift of the concentration profiles along the z-axis.

Comparisons were also made with Chang and Brown's calculations of the effects of varying some of the material and processing parameters. In the following examples, the reference case is Rayleigh number Ra = 100, segregation coefficient k = 0.1, Schmidt number Sc = 10, sample radius a = 0.5 cm, and adiabatic zone length L_a = 0.5 cm. The effects of varying the segregation coefficient k are shown in Table III.

Table 2.3

k	$\zeta_{C\&B}$	$\zeta_{(6.5\mu m/sec)}$	$\zeta_{(16\mu m/sec)}$
0.1	17%	15.0%	17.3%
0.3	10%	9.4%	8.2%
0.5	7%	5.6%	4.3%
0.7	3%	2.9%	2.0%
0.9	2%	0.9%	0.6%

The Schmidt number was varied by varying the diffusion coefficient. The results are shown in Table I2.4.

Table 2.4

Sc	$\zeta_{C\&B}$	$\zeta_{(6.5\mu m/sec)}$	$\zeta_{(16\mu m/sec)}$
30	36%	47.4%	18.4%
20	32%	36.2%	19.9%
10	16%	15.0%	17.3%
5	4%	4.6%	8.3%

The effect of varying the length of the adiabatic zone was also investigated and the results are shown in Table 2.5.

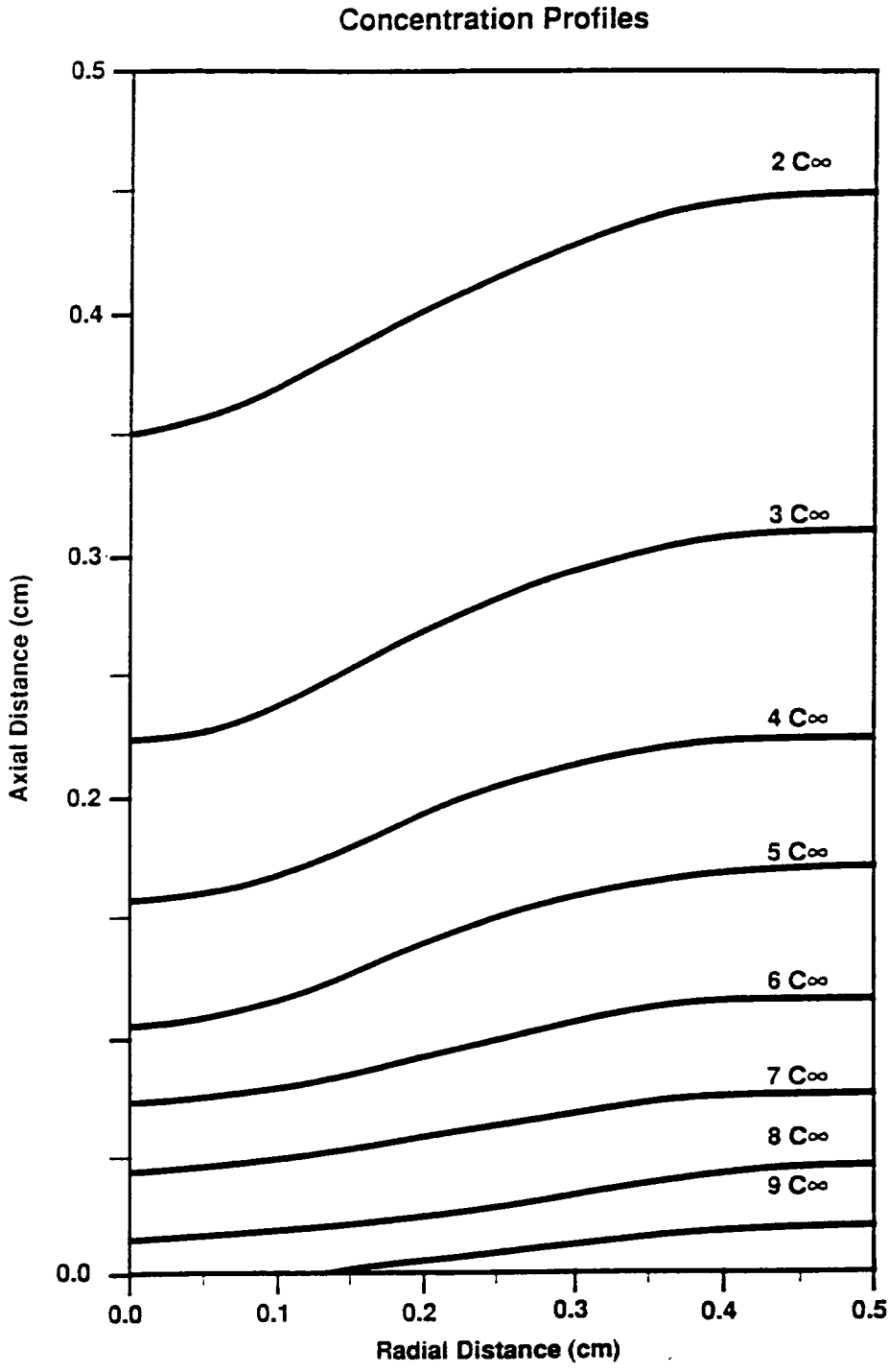

Figure 2. Concentration profiles throughout the melt in the case considered by Chang and Brown.

C-2

Table 2.5

$La_{(cm)}$	$2\lambda_{(cm)}$	$\zeta_{C\&B}$	$\zeta_{(6.5\mu m/sec)}$	$\zeta_{(16\mu m/sec)}$
0.5	0.6	20%	15.0%	17.3%
1.0	1.2	6%	8.7%	7.7%
1.5	1.8	2%	4.6%	3.2%
2.0	2.4	<1%	3.0%	2.3%

The stated Chang and Brown results were scaled from the figures in their paper and are probably not accurate to better than a few percent. Also, lengthening the adiabatic zone alters the thermal profile, reducing the average radial thermal gradient which drives the flows, resulting in smaller convective velocities. This was not taken into account in the above calculations which could account for the increasing discrepancies between this model and the results of the Chang and Brown model as the adiabatic zone is increased.

2.5 COMPARISON WITH ALEXANDER, OUAZZANI, AND ROSENBERGER'S RESULTS

A more extensive numerical study of the effects of low level residual acceleration on various microgravity experiments was recently completed by Alexander, Ouazzani, and Rosenberger (A.O.R.). Since they were more interested in non-axisymmetric cases as well as in time dependent cases, they solved the flow and mass transport equations in a two-dimensional rectangular geometry in order to simplify the problem and to keep the computer time within reasonable bounds. Several static three-dimensional cases were solved numerically as checks on the use of the two-dimensional model and the differences for the most cases were not found to be significant. They chose the same growth system as Chang and Brown and calculated the radial segregation for a variety of applied accelerations as well as for different sizes, temperature fields, and growth velocities.

A comparison of the perturbation model with their results for cases in which the acceleration is perpendicular to the growth interface is shown in Table 2.6. Since A.O.R. assumed the the same thermal field as Chang and Brown, the same expression relating average radial temperature gradient to the hot zone and melting point temperatures, eq. (2.40), was also used in computing these comparisons. The other parameters were identical to those used in the Chang and Brown model.

The agreement between the first order perturbation model and the results obtained by Alexander, Ouazzani, and Rosenberger is extremely close (within a few percent) for small Peclet numbers where the assumptions made in the first-order perturbation theory are strictly valid. For Peclet numbers approaching and even exceeding unity the differences are within a factor of two.. It is

interesting to note that the disagreement between the first-order analytical model and the computational results becomes more severe if the Peclet number is increased because of increasing g-level, which increases the actual convective velocity, rather than by decreasing growth velocity (e.g., compare the 10^{-4} g case for v_g = 6.5 μm/sec with the 10^{-5} g case with v_g = 0.65 μm/sec). This is a result of the fact that the error introduced by dropping the radial convective transport term in the first-order model becomes more serious as the convective velocity increases. At the very low convective velocities, this transport would be reduced by the radial back-diffusion term.

TABLE 2.6

		A.O.R.'s results			This work	
g/g_0	T_H(K)	v_g(μm/sec)	a(cm)	ζ	Pe	ζ
10^{-5}	1331	6.5	0.5	6.4%	-0.377	5.8%
10^{-5}	1331	0.65	0.5	0.95%	-3.77	0.80%
$5x10^{-6}$	1331	6.5	0.5	3.2%	-0.188	2.9%
10^{-4}	1346	6.5	0.5	36%	-4.34	66%
10^{-5}	1346	6.5	0.5	7.5%	-0.434	6.6%
$1.4x10^{-6}$	1346	6.5	0.5	2.0%	-0.0607	0.93%
10^{-6}	1346	6.5	0.5	0.7%	-0.0434	0.66%
10^{-5}	1346	3.25	0.5	4.6%	-0.868	4.1%
10^{-5}	1346	0.65	0.5	0.7%	-4.34	0.93%
10^{-6}	1346	3.25	0.5	0.4%	-0.087	0.41%
10^{-6}	1346	0.65	0.5	0.0%	-.434	0.09%
10^{-6}	1346	6.5	1.0	3.8%	-.174	6.4%

It is particularly gratifying to observe that the perturbation model responds to variations in the growth velocity in the same manner as the numerical model. On the one hand decreasing the growth velocity increases the Peclet number which increases the perturbation to the composition field. However, this also reduces the gradient in the diffusion field in front of the interface which lessens the compositional variations, thus offsetting the increase due to the larger Peclet number. The perturbation model appears to have correctly captured this feature.

For the last case, in which the size was doubled, it was assumed that the entire system was scaled in proportion. This has the result of doubling the length of the adiabatic zone, hence λ. However it is not clear whether this scaling actually preserved the thermal profile used in the the A. O. R. computations. This might account for the apparent difference between the two models which is larger than might be expected given the small value of the Peclet number.

2.6 RESPONSE TO TRANSIENT AND PERIODIC ACCELERATIONS

The time-dependent equation for the z-component of velocity, eq. (2.4) may be written

$$\frac{\partial w}{\partial t} = \frac{\partial^2 w}{\partial r^2} + \frac{1}{r}\frac{\partial w}{\partial r} + \frac{g\,\beta\langle\Delta T\rangle}{\nu}\left[(r/a)^2 - \frac{1}{3}\right] \tag{2.43}$$

where the inertial term has been neglected, the pressure gradient was assumed to equal the rg term, and the $(T_0 - T_1)/\langle\Delta T\rangle$ term has been set to 1/3 to adjust the buoyancy term to provide no net flow.

For a transient acceleration applied to a system initially at rest, ie. g is "switched on" at t = 0, the solution may be written

$$w(r,t) = w(r) + \hat{w}\sum_{n=1}^{\infty} E_n\, J_0(s_n\, r)\, e^{-s_n^2\, \nu\, t} \tag{2.44}$$

where w(r) is given by eq. 2.5.

Notice that the time constant is given by

$$\tau_n = \frac{1}{s_n^2\,\nu} \quad . \tag{2.45}$$

The most persistent term is n = 1. The time constant associated with this term is

$$\tau_n = \frac{a^2}{2.4048^2\,\nu} = \frac{a^2}{5.78\,\nu}$$

which for a = 0.5 cm and $\nu = 0.0013$ cm^2/sec, τ = 33 sec. However, the initial response is much faster because of the higher order terms. As may be seen in Figure 3, the time required for the fluid to reach 1/e of its final velocity calculated from eq. (2.44) for the above case is only 12 sec. For comparison, the time constant estimated by Langbein and Tiby [4] was a^2/n which would give 192 sec.

Griffin and Motakef (G&M) analyzed numerically the response of the melt in a Bridgman growth system to both transient and periodic accelerations [15]. For small Rayleigh numbers, they find the time required for the upper convective roll to reach 99% of its steady state value was 0.17 a^2/ν, which for the case at hand would correspond to 33.7 seconds (the 1/e time was not specified). Eq. (2.44)

would predict 117 sec to reach 99% of the steady state velocity. Since the flows in the upper convective roll closely correspond to the flows predicted from the one-dimensional model (G&M state that these flows are exclusively controlled by melt radius and kinematic viscosity and, to the first order, are independent of the longitudinal extent of the the convective cells), it is difficult to understand why the time response time could be significantly shorter than that predicted by the one-dimensional analytical model.

For periodic accelerations, assume $g(t) = \hat{g}\, e^{i\omega t}$ where $\hat{g}$ is the amplitude of the acceleration. After the initial transient dies out, the velocity will be given by $w(r,t) = \Delta w(r)\, e^{i\omega t}$ where $\Delta w(r)$ is the the complex amplitude of the velocity. Now eq. (2.43) becomes

$$\frac{d^2 \Delta w}{dr^2} + \frac{1}{r}\frac{d \Delta w}{dr} - \frac{i\,\omega\, \Delta w}{\nu} + \frac{\hat{g}\,\beta\,\langle \Delta T \rangle}{\nu}\left[\left(\frac{r}{a}\right)^2 - \frac{1}{3}\right] = 0 . \qquad (2.46)$$

It is convenient to express the solution as a Fourier-Bessel series

$$\Delta w(r) = \hat{w} \sum_{n=1}^{\infty} E_n' J_0(s_n r) \qquad (2.47)$$

where $\hat{w}$ is the maximum steady state velocity given by eq (2.6) that would result from an acceleration amplitude $\hat{g}$, and E_n' are the new complex Fourier-Bessel coefficients. This choice of representation of the solution automatically satisfies the "no-slip" boundary conditions at the walls. Taking derivatives, putting them back into eq. (2.46), and multiplying by a^2, we get

$$\sum_{n=1}^{\infty} \left[\xi_n^2 + i\,\Omega\right] E_n' J_0(s_n r) = 48\left[\left(\frac{r}{a}\right)^2 - \frac{1}{3}\right] \qquad (2.48)$$

where the dimensionless frequency Ω is $w\, a^2/\nu$,and ξ_n are the zeros of J_0.

Using the orthogonality properties of J_0, we can multiply by $J_0(s_m r)$ and extract the Fourier-Bessel coefficients;

$$E_m' = \frac{-64}{J_1(\xi_m)}\left[\frac{1}{\xi_m^3} - \frac{6}{\xi_m^5}\right]\left(\frac{1 - i\Omega/\xi_m^2}{1 + \Omega^2/\xi_m^4}\right) . \qquad (2.49)$$

Note that $\Omega/\xi_m^2 = \omega\tau_m$ where τ_m was the time constant for the m^{th} term in the transient solution. It may also be seen that for $\Omega = 0$ the solution becomes the steady state solution given by eq. (2.22) as E_m' reduces to E_m.

The amplitude of the velocity is

$$\Delta w(r) = \hat{w} \left\{ \sum \left[\mathrm{Re}(E_m') J_0(s_m r) \right]^2 + \sum \left[\mathrm{Im}(E_m') J_0(s_m r) \right]^2 \right\}^{1/2} \quad . \quad (2.50)$$

The velocity amplitude at r = 0 is given by

$$\Delta w(0) = \hat{w} \left\{ \sum \left[\frac{E_m}{1+\Omega^2/\xi_m^4} \right]^2 + \sum \left[\frac{E_m \Omega}{\xi_m^2 \left(1+\Omega^2/\xi_m^4\right)} \right]^2 \right\}^{1/2} \quad . \quad (2.51)$$

If $\Omega >> \xi_m^2$, the imaginary contributions will dominate (eventually $\xi_m^2 > \Omega$, but by them the E_m terms will no longer be significant) and the velocity amplitude at r = 0 becomes

$$\Delta w(0) \rightarrow \hat{w} \sum_{m=1}^{\infty} \frac{E_m \xi_m^2}{\Omega} \quad , \quad \Omega >> \xi_m^2 \quad . \quad (2.52)$$

If we set $\Omega = 0$ in eq (2.48) for r = 0, we see that

$$\sum E_m \xi_m^2 = -16$$

Therefore, for the higher frequency disturbances, the velocity amplitude at r = 0 becomes using eq. (6)

$$\Delta w(0) \approx \hat{w} \frac{16}{\Omega} = \hat{w} \frac{16 \nu}{\omega a^2} = \frac{\hat{g} \beta \langle \Delta T \rangle}{3 \omega} \quad , \quad \Omega >> \xi_1^2 \quad . \quad (2.53)$$

Figure 2.4 shows how the velocity amplitude starts to diminish at around 0.01 rad/sec and becomes inversely proportional to w at 10 rad/sec. For comparison, G&M find that for $\omega >> a^2/\nu$,

$$\Delta w = \frac{\hat{w} \nu}{0.17 \omega a^2} = \frac{5.9 \hat{w} \nu}{\omega a^2} \quad .$$

This has the same functional form as eq. 2.53, but differs by a factor of 2.7. One possible reason for this discrepancy is that G&M compared the amplitude of the fluctuating stream function with the value for steady accelerations, whereas this work compares the velocity amplitude at r = 0 with its value for steady accelerations. Even though the buoyancy driven convective velocity is maximum at r = 0 for steady accelerations, this is not necessarily the case for higher frequencies. Even so, the one-dimensional model seems to give close enough agreement to be useful for the purpose intended.

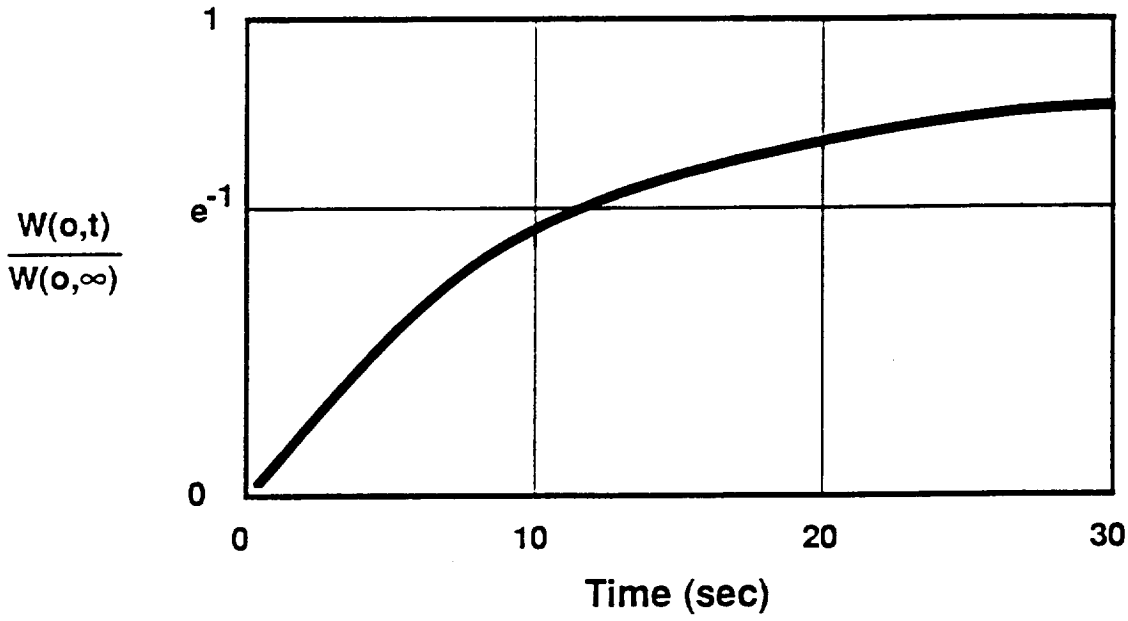

Fig. 2.3. Build up of convective flow at r = 0 from a steady acceleration that is suddenly "turned-on" at t = 0. Even though the time constant for the dominant (most persistent) term is 33 sec, only 12 sec is required to reach 1/e of the final steady state value.

2.7 EFFECT OF PERIODIC ACCELERATIONS ON MASS TRANSFER

The time dependent mass transfer equation is

$$\frac{\partial C}{\partial t} + (u - v_g)\frac{\partial C}{\partial r} + w\frac{\partial C}{\partial z} = D\left[\frac{1}{r}\frac{\partial c}{\partial r} + \frac{\partial^2 C}{\partial r^2} + \frac{\partial^2 C}{\partial z^2}\right] . \qquad (2.54)$$

Using the perturbation approach as before, the u and v velocity components are expanded in terms of the Peclet number as before, except now the Peclet number is assumed to be

$$P_e = \Delta P_e\, e^{i\omega t} = \frac{\Delta w(0)\, e^{i\omega t}}{v_g} \qquad (2.55)$$

and the concentration is assumed to be expressed by

$$C(r,z,t) = C_z(z) + \Delta P_e\ \tilde{C}(r,z)\ e^{i\omega t} \quad . \qquad (2.56)$$

Putting this back into the partial differential equation and dropping all but first order terms in ΔPe as before, we obtain

$$-i\,\omega\,\tilde{C} + v_g\frac{\partial \tilde{C}}{\partial z} - v_g\,\tilde{w}\frac{\partial C_z}{\partial z} + \frac{D}{r}\frac{\partial \tilde{C}}{\partial r} + D\frac{\partial^2 \tilde{C}}{\partial r^2} + D\frac{\partial^2 \tilde{C}}{\partial z^2} = 0 \quad . \qquad (2.57)$$

The variables separate as before but eq. (2.23), the second order ordinary differential equation that must be solved for $f_n(z)$, now has an extra term, vis

$$f_n''(z) - \frac{f_n'(z)}{\delta} - \left(s_n^2 + \frac{i\,\omega}{D}\right) f_n(z) = -\frac{(1-k)}{\delta^2}\frac{C_\infty}{k}\,\tilde{w}_z \quad . \qquad (2.58)$$

The solution for $f_n(z)$ will still given by eq. (26) if the s_n^2 terms in A_n, B_n, C_n, D_n and r_n are replaced by $s_n^2+i\omega/D$.

The perturbed concentration field is then given by

$$\Delta P_e\,\tilde{C}(r,z) = \frac{\hat{w}}{v_g}\sum E_n'\, J_0(s_n\, r)\, f_n(z) \qquad (2.59)$$

where E_n' is given by eq. (2.49) above.

The fall-off of the perturbed concentration field at the interface with frequency is also shown in Figure 2.4. The controlling factor is the relative magnitude of s_n^2 and w/D. If $\omega/D \gtrsim s_n^2$ (or $\omega\, a^2/D \gtrsim \xi_1$), then the concentration field cannot cannot change as rapidly as the applied acceleration and the amplitude of the oscillation will be diminished. As may seen this begins to occur at around 10^{-4} Hz which corresponds to a value of $\omega\, a^2/D = 1.28$. The fall-off becomes more rapid with increasing frequency, and when the velocity amplitude also begins to fall-off with increasing frequency, the concentration perturbation fall as the inverse cube of frequency.

This behavior may be understood by examining the various coefficients that make up the fn terms by replacing each s_n^2 term with ω/D. This yields

$$B_n \to \frac{-2\,G\,D^2(2\,\beta+\alpha)}{\omega^2},\quad C_n \to \frac{2\,G\,D^2}{\omega^2},\quad r_n \to \frac{-\sqrt{2\,\omega}\,(1+i)}{2\sqrt{D}}$$

$$D_n \to \frac{-\sqrt{2}\,G\,D^{5/2}(3\,\beta+(1+k)\,\alpha)(1-i)}{\omega^{5/2}}$$

$$f_n(0) \to \frac{2\,G\,D^2}{\omega^2} + \frac{i\sqrt{2}\,G\,D^{5/2}\,(3\,\beta+(1+k)\,\alpha)}{\omega^{5/2}}$$

In the limit of large ω, the amplitude of the perturbed concentration field at $r = 0$ on the interface becomes

$$\Delta P_e\,\tilde{C}(0,0) = \frac{\hat{w}}{v_g}\sum E_n'\,f_n(0) \to \frac{-2\,i\,G\,D^2\,\hat{w}}{\omega^2\,\Omega\,v_g}\sum E_n\,\xi_n^{\,2}\,. \qquad (2.60)$$

Using the definition of Ω and the previously determined value for the sum, this may be written

$$\Delta P_e\,\tilde{C}(0,0) \to \frac{32\,i\,G\,D^2\,\nu\,\hat{w}}{\omega^3\,a^2\,v_g} \qquad (2.61)$$

where G is given by eq. 2.25.

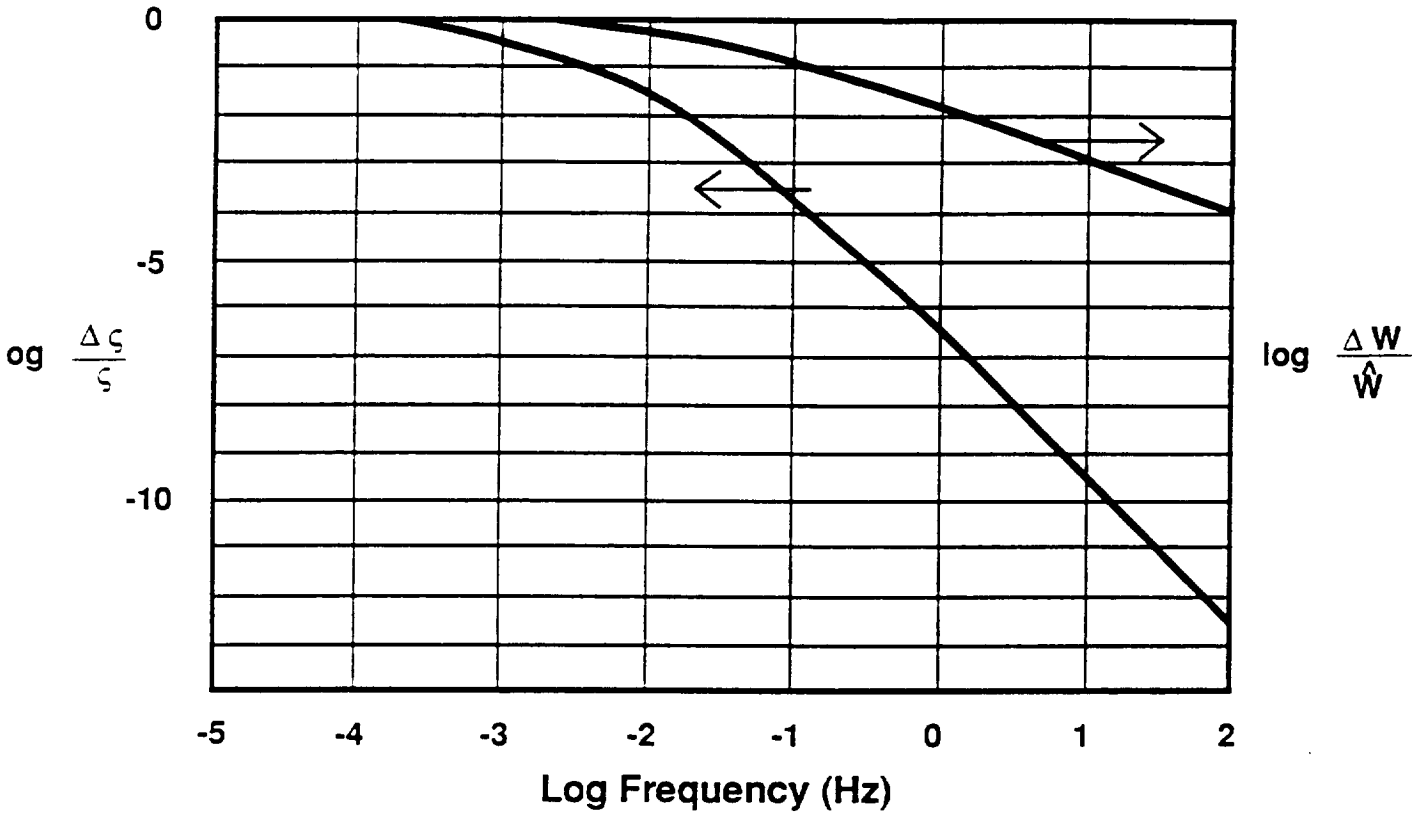

Fig. 4. Response of the velocity and of the concentration at the interface to periodic accelerations. For very low frequencies (< 10^{-4} Hz) the flow and concentration fields retain their steady state values. The velocity field will start to diminish at around 0.01 Hz and falls off as the inverse of frequency beyond 0.1 Hz. The perturbation to the concentration field starts to diminish at around 10^{-4} Hz and falls off as the inverse cube of frequency above 0.1 Hz

The composition at the interface will fluctuate with a frequency w and the relative variation at r = 0, which in this case would be the radial segregation, is given by

$$\zeta = \frac{\left|\Delta P_e \tilde{C}(0,0)\right|}{C_z(0)} \approx \frac{8\, e^2 (1-k) D^2 \nu\, \hat{w}}{\delta^2 \lambda^2 \omega^3 a^2 v_g} \quad . \tag{2.62}$$

Using the definition for d and eq. (2.6) for the maximum convective velocity, this may be written

$$\zeta \approx \frac{e^2 (1-k) \beta \langle \Delta T \rangle \hat{g} v_g}{6 \lambda^2 \omega^3} \quad , \quad \omega >> \xi_1^2 D/a^2 \quad \text{and} \quad \omega >> \xi_1^2 \nu/a^2 \tag{2.63}$$

Note that this is independent of material parameters (except for expansion coefficient) and the only size parameter that appears is the length of the adiabatic zone. This is somewhat different from the order of magnitude analysis of Langbein and Tiby who estimated

$$\frac{\delta C}{C} = \frac{\hat{g}\, \Delta\rho/\rho}{L\, \omega^2} \quad \text{which corresponds to} \quad \zeta = \frac{\hat{g}\, \beta \langle \Delta T \rangle}{L\, \omega^2}$$

where L is some length scale.

2.8 CONCLUSIONS

It has been shown that a simple one-dimensional flow model can be used to obtain a reasonably accurate estimate of the maximum buoyancy-driven convective velocity of a dilute binary melt in a vertical Bridgman crystal growth system. Using this estimate, a first-order perturbation solution to the mass transport equation was obtained for convective flows that are small compared to the growth velocity. The radial segregation computed by this combined analytical model compares quite favorably with the numerical models developed by Chang and Brown and by Alexander, Ouazzani, and Rosenberger indicating that the essential physics has been captured by this model. This means that the model can be used with some confidence to predict the effects of varying material and/or processing parameters for experiments subject to small convective flows such as those produced by the residual acceleration on an orbiting spacecraft. It has also been found that even though the first order perturbation calculation of the concentration profiles is no longer valid as the convective velocities approach the growth velocity, the model continues to give reasonable values for radial segregation since the primary effect of the higher order terms is to shift these profiles along the vertical axis, thus the difference between their maximum and minimum value is not greatly affected until the convective flows exceed the growth velocities and circulation

patterns form in the melt.

The approximate analytical solution can also provide considerable insight into the roles of the various processing parameters from which some general conclusions may be drawn:

1. Axial segregation is diffusion controlled and radial segregation is directly proportional to the applied acceleration as long as the maximum buoyancy-driven flows are less than the growth velocity.

2. The mixing between the radial flow and the diffusion boundary layer is the greatest when the diffusion length and the radial flow boundary layer thickness are comparable which results in the maximum radial segregation. The radial segregation becomes vanishingly small as either parameter becomes very small or very large.

3. If the diffusion length is much larger than the ampoule radius, the radial segregation will be proportional to the growth velocity. If the ampoule is much larger than the diffusion length, radial segregation will be lessened by increasing growth velocity.

4. If the diffusion length is much larger than the ampoule radius, the radial segregation will be a strong function of the ampoule radius, both because of the dependence of flows on the ampoule radius as well as the influence of sample size on mass transport. If the ampoule radius is much larger than the diffusion length, radial segregation will be influenced by sample radius only through the increased convective velocity.

5. If the ampoule radius is much smaller than the diffusion length, the percent radial segregation is proportional to (1-k). If the ampoule is much larger than the diffusion length, the percent radial segregation is proportional to (1-k)/k.

6. For periodic accelerations, the velocity amplitude is inversely proportional to the frequency for frequencies larger than 2.5 ν/a^2 Hz. The perturbation in composition at Hz the interface becomes proportional to the inverse square of the frequency for frequencies larger than 0.2 D/a^2·Hz, and proportional to the inverse cube of the frequency for frequencies larger than 2.5 ν/a^2 Hz (assuming Schmidt number >1).

7. Since the approximations for the governing equations used in this analysis were all all linear equations, any linear combination of solutions is also a solution. Therefore, the response to multiple frequencies, or to a combination of a steady acceleration and a number of applied frequencies can be found by simply adding the solutions for each individual case.

Although some of these conclusions may be self-evident or could have been drawn from the number of numerical computations that have been reported in the literature, it is useful and somewhat more assuring to be able to examine directly the interplay of the various parameters in the functional relationships that govern the process.

2.9 REFERENCES

1. S. M. Pimputkar and S. Ostrach, J. Crystal Growth 55 (1981) 614-646
2. D. Camel and J.J. Favier, J. Crystal Growth 61 (1983) 125
3. D. Langbein and C. Tiby, Allowable g-levels for Microgravity Payloads, Final Report for ESA, Contract No.5.504/83/F/FS(SC), Battelle Frankfurt, September 1984
4. J. I. D. Alexander and F. Rosenberger, in Low Gravity Fluid Dynamics and Transport Phenomena (Ed. J. N. Koster and R. L. Sani), Progress in Astronautics and Aeronautics, Vol. 130, American Institute of Aeronautics and Astronautics, Washington, DC (1990) 87-116
5. C.J. Chang and R.A. Brown, J. Crystal Growth, 82 (1983) 327
6. P.M. Adornato and R. A. Brown, J. Crystal Growth 80 (1987) 155
7. D. H. Kim and R. A. Brown, J. Crystal Growth 96 (1989) 609-627
8. J. I. D. Alexander, J. Ouazzani and F. Rosenberger, J. Crystal Growth, 97 (1989) 285.
9. J. I. D. Alexander, S. Amiroudine, J. Ouazzani and F. Rosenberger, J. Crystal Growth (in press)
10. It is recognized that low-level lateral accelerations acting on the larger axial density gradients will produce stronger convective flows than the axisymmetric case considered in this paper. However, care is now being taken in the present generation of space experiments to align the furnace axis as closely as possible with the steady component of the residual acceleration vector. This is possible if the vehicle flies in a fixed orientation relative to Earth.
11. Coriell, S. R. and R. F. Sekerka, J. Crystal Growth 46 (1979) 479.
12. R. B. Bird, W.E. Stewart, and E. N. Lightfoot, Transport Phenomena, John Wiley and Sons, New York, 1960, pp 297-300
13. An equation for the radial velocity component may be constructed from Eq.(24) and the continuity equation, vis.

$$u(r,z) = \hat{w}\,\frac{e^2}{8}\,\frac{a}{\lambda}\left[\frac{r}{a} - 2\left(\frac{r}{a}\right)^3 + \left(\frac{r}{a}\right)^5\right]\left[2\,\frac{z}{\lambda} - \left(\frac{z}{\lambda}\right)^2\right] e^{-z/\lambda} \quad .$$

From this it may be seen that u peaks at $r = 0.586\,\lambda$, reverses at $r = 2\lambda$, and that the bulk of the radial flow is contained between r = 0 and l. Therefore, λ may reasonably be considered as the thickness of the horizontal flow boundary.
14. P. R. Griffin and S. Motakef, Appl. Microgravity Tech. II (1989) 3 121-132

SECTION 3

SOLUTE REDISTRIBUTION IN BRIDGMAN GROWTH WITH TRANSVERSE ACCELERATIONS

3.1 INTRODUCTION

The problem of obtaining compositional homogeneity in bulk crystals grown from the melt has received considerable attention in recent years. For example, Chang and Brown showed that even in vertical Bridgman growth with a stabilizing thermal gradient, buoyancy-driven convective flows resulting from radial temperature gradients will cause considerable radial segregation [1]. Application of strong magnetic fields are somewhat, but not completely, effective in controlling these flows in Earth's gravity [2]. The problem is even more difficult when solutal gradients oppose the thermal gradient as was shown by Coriell, et al [3]. A number of attempts have been made to reduce these flows by taking advantage of various space flight opportunities to grow crystals in a microgravity environment. Witt and Gatos were able to eliminate dopant striations in their early experiments, but did not achieve uniform doping in a dilute system [4-5] . Fripp and Crouch observed almost complete mixing in their attempt to grow a non-dilute alloy-type system [6].

As a result of these early experiments, investigators began to realize that simply reducing gravity by 5 to 6 orders of magnitude may not be sufficient to eliminate solute redistribution due to residual convective flows. Chang and Brown's computations did indicate that 5 to 6 orders of magnitude reduction in gravity should be sufficient to virtually eliminate radial segregation in dilute systems up to approximately 1 cm in diameter, but their model only addressed steady longitudinal accelerations (g-vector along the furnace axis). More recently, Alexander, et al developed numerical models to treat transverse accelerations [7] and time dependent accelerations [8]. As might be expected, they showed that significant segregation could occur in dilute systems for transverse accelerations less than 1 micro-g. Because of this realization, an attempt was made to fly the first United States Microgravity Laboratory (USML-1) Spacelab mission so that the axis of the Crystal Growth Furnace (CGF) was aligned with the residual acceleration vector to minimize transverse accelerations.

All of the models cited above utilize computational fluid dynamic (CFD) techniques to solve the coupled set of partial differential equations that describe the flow and compositional fields. While much can be learned from these computations, they provide data only at selected points in the multi-dimension parameter space involved in the process. Thus it is difficult to gain insight into how the systems would behave under different processing conditions or to extrapolate the results to other systems. Several previous attempts at developing scaling laws [9-10] using a single length scale to characterize the process were not particularly successful because of the complicated interplay of the various length scales that have to be considered. This was demonstrated by Naumann and Baugher who succeeded in developing an approximate analytical

model for dilute systems under steady and time-varying longitudinal accelerations which gave some insight into the complexities involved in scaling even a fairly simple system [11]. Garandet [12] used an impirical model similar to that used by Batchelor [13] to describe the flow in a 2-dimensional slot. He then used an order-of-magnitude scaling analysis to determine the lateral compositional variations as a function of the Peclet number, which he defines as the ratio of slot width to the diffusion length. Having obtained the functional dependence in the limits of high and low Peclet numbers, he used computational results to refine his order-of magnitude estimates and obtained an interpolation equation that gives quite good agreement with the computational results over the entire range of Peclet numbers.

In this section an approximate analytical model is developed to describe the flow field and its effect on the concentration field in a Bridgman configuration subjected to very small steady transverse accelerations so that departures from diffusion limited behavior can be studied. Unlike the model developed by Garandet, which assumes a constant temperature gradient along the axis of the ampoule, a more realistic exponential density gradient will be assumed. This will allow non-dilute systems whose solutal fields decay exponentially along the axis to be considered also. The resulting equations also provide valuable insight into how the various parameters interact and should provide useful scaling laws that can be applied in general to different growth systems. Such scaling laws will serve as useful guides for developing future experiments and will allow more efficient use to be made of the numerical models.

3.2. ASSUMPTIONS

To keep the mathematics tractable, several simplifying assumptions must be made that limit the applicability of the model. First, the flow equations are solved independently of the mass and heat transport equations on the assumption that the flows are small enough that they do not significantly alter the density field. This is a good assumption for dilute systems where the density variations are primarily due to temperature differences since most materials of interest have low Prandtl numbers and heat transfer is predominantly by conduction for the flow regime of interest. For non-dilute systems, this assumption restricts the flow model to small perturbations in the concentration field. However, since the intent of the model is to examine the influence of convective flows near the diffusion-controlled regime, this is not a serious restriction. Having already limited the flow model to very small flow velocities, the non-linear inertial terms are second order and can be ignored which greatly simplifies the calculations.

Second, no longitudinal gravity field is assumed, thus eliminating any effects of a stabilizing or destabilizing density gradient. This also eliminates any effect from radial temperature gradients which had been studied previously [11]. Again, for the dilute case, in which it has already been assumed that the temperature field is unperturbed by the small flows, this is a good assumption. In fact, Alexander, et al investigated several cases in which the acceleration vector was applied downward at 45° to the furnace axis [7]. For small accelerations, where the

segregation is directly proportional to acceleration, these cases produced the same result as that of a pure lateral acceleration with the same horizontal component.

To avoid the complexities involved with non-axisymmetric cylindrical coordinates, the flow and mass transport analyses are carried out in a two-dimensional rectangular slot. Alexander, et al used this simplifying geometry for the bulk of their studies but also carried out a full three-dimensional computation for a few cases for comparison. They found that the two models generally agreed to within 20-25% of each other. Given the other simplifying assumptions that were necessary to make as well as the uncertainties in some of the thermophysical properties that go into such calculations, this accuracy appears adequate for the intended purposes of this model.

Finally, it is assumed that the crystal is growing with a flat interface at constant velocity under steady-state growth conditions; i. e. the diffusion field is fully developed and does not change with time. The density field is assumed to be one-dimensional and is represented by an exponential function that decays with some characteristic length scale. The growth ampoule is assumed to be long enough so that neither the flow field nor the concentration field is affected by the end away from the growth interface.

3.3 FLOW MODEL

In order to estimate the effects of small transverse accelerations on the redistribution of solute in directionally solidified melts, a model for the flow field must first be established. There have been a number of attempts to obtain analytical solutions to describe the two-dimensional flow fields in horizontal chambers with differentially heated ends walls. [13-18]. For large length to width ratios, all of the models describe the horizontal flow in the core region as a one-dimensional cubic function symmetric about the centerline. This core flow is then matched to a more complex flow in the end regions. Unfortunately, the resulting equations for the flow in the end regions are generally too complicated to be useful for this type of analysis. The impirical polynomial representation used by Garandet assumes a linear density profile and therefore is not applicable to the problem at hand.

The flow problem may be formulated by replacing u and v in the x- and y-momentum equations by $u = -\frac{\partial \psi}{\partial y}$ and $v = \frac{\partial \psi}{\partial x}$ to satisfy the continuity equation, cross differentiating, and subtracting to eliminate the pressure terms. The result is a single 4th-order partial differential equation for the stream function ψ. Neglecting the inertial terms, this equation becomes

$$\frac{\partial^4 \psi}{\partial x^4} + 2\frac{\partial^4 \psi}{\partial x^2 \partial y^2} + \frac{\partial^4 \psi}{\partial y^4} + \frac{g_y}{\mu}\frac{\partial \rho}{\partial x} - \frac{g_x}{\mu}\frac{\partial \rho}{\partial y} = 0 \qquad (3.1)$$

where g_x and g_y are the components of the gravity vector and $\rho(x,y)$ is the density of the fluid. It is assumed that the system is aligned such that the acceleration is predominately in the -y direction (horizontal Bridgman configuration) or that the density variations in the y direction are small enough that

$$\left|\frac{g_y}{\mu}\frac{\partial\rho}{\partial x}\right| >> \left|\frac{g_x}{\mu}\frac{\partial\rho}{\partial y}\right| \tag{3.2}$$

which could apply to a dilute system in a slightly misaligned vertical Bridgman configuration provided the thermal conductivity of the melt is high enough so that the isotherms are not affected by the resulting convective flows.

The boundary conditions require that ψ and its normal derivative vanish at each wall to enforce the no-slip condition.

An exponential function of the following form is chosen to represent the density,

$$\rho(x) = \frac{(\rho(0)-\rho(L))e^{-x/\lambda} - \rho(0)e^{-L/\lambda} + \rho(L)}{1-e^{-L/\lambda}} \tag{3.3}$$

where $x = 0$ is taken at the solidification interface and λ is the e-folding length. If L is finite, this function describes the density profile as a decaying exponential between $\rho(0)$ and $\rho(L)$ with a gradient given by

$$\frac{\partial\rho}{\partial x} = -\frac{\Delta\rho\, e^{-x/\lambda}}{\lambda}, \quad \Delta\rho = \frac{\rho(0)-\rho(L)}{1-e^{-L/\lambda}}. \tag{3.4}$$

Introducing dimensionless coordinates $\xi = x/a$, $\eta = y/a$, equation (3.1) can be written.

$$\frac{\partial^4\psi}{\partial\xi^4} + 2\frac{\partial^4\psi}{\partial\xi^2\partial\eta^2} + \frac{\partial^4\psi}{\partial\eta^4} = \frac{g[\rho(0)-\rho(\infty)]a^4 e^{-a\xi/\lambda}}{\rho_0\,\nu\lambda} = \mathrm{Gr}\,\nu\, e^{-a\xi/\lambda}. \tag{3.5}$$

where $\mathrm{Gr} = \dfrac{g\Delta\rho a^4}{\rho(L)\nu^2\lambda}$ and $\Delta\rho$ is given by eq. (3.4).

(Note that if $L >> \lambda$, $\mathrm{Gr} \rightarrow \dfrac{g[\rho(0)-(L)]a^4}{\rho(L)\nu^2\lambda}$, whereas if $L << \lambda$, $\mathrm{Gr} \rightarrow$ $\dfrac{g[\rho(0)-(L)]a^4}{\rho(L)\nu^2 L}$ and $\rho(x)$ becomes linear from 0 to L.)

Boundary conditions are:

$\psi = 0$ at $\xi = 0, \infty$ and $\eta = \pm 1$;

$$v = \frac{1}{a}\frac{\partial \psi}{\partial \xi} = 0 \text{ at } \xi = 0, \infty; \text{ and } u = -\frac{1}{a}\frac{\partial \psi}{\partial \eta} = 0 \text{ at } \eta = \pm 1.$$

These boundary conditions assume a semi-infinite ampoule. They could be enforced at some finite length, but at considerable complexity. However, since the region of interest is in the vicinity of $\xi = 0$, and since the comparison with computer modeling is good provided $L >> a$, the above formulation appears adequate for the intended purpose.

If the gradient were uniform over a distance $L>>h$, the equation would be dominated by the η-derivatives in the central regions away from the ends and the stream function behaves as a simple 4th deg. polynomial in η. We might therefore assume that the stream function preserves this form for all ξ and write an approximate solution in the form

$$\psi = \varphi(\xi)\left(\eta^4 - 2\eta^2 + 1\right), \quad 0 < \xi < L/a \tag{3.6}$$

where $\varphi(\xi)$ is a function of ξ only and represents the stream function along $\eta = 0$. Putting this back into eq. (3.5) and evaluating the η derivatives at $\eta = 0$, we obtain the 4th order ordinary differential equation

$$\frac{d^4\varphi}{d\xi^4} - 8\frac{d^2\varphi}{d\xi^2} + 24\varphi = Gr\, v e^{-a\xi/\lambda}. \tag{3.7}$$

This may be solved by Laplace transforms using the boundary conditions $\varphi(0) = \varphi'(0) = 0$ and $\varphi(\xi) = \varphi'(\xi) \to 0$ as $\xi \to \infty$ to obtain

$$\varphi(\xi) = Gr^* v \left\{e^{-a\xi/\lambda} - \left[\cos(\beta\xi) + \gamma \sin(\beta\xi)\right]e^{-\alpha\xi}\right\} \tag{3.8}$$

where

$$Gr^* = \frac{Gr}{\left(24 - 8a^2/\lambda^2 + a^4/\lambda^4\right)}, \quad \alpha^2 = 2 + \sqrt{6}\,, \quad \beta^2 = -2 + \sqrt{6},$$

$$\text{and } \gamma = \frac{(\alpha - a/\lambda)}{\beta}$$

The complete stream function is therefore,

$$\psi = Gr^* v \left\{e^{-a\xi/\lambda} - \left[\cos(\beta\xi) + \gamma \sin(\beta\xi)\right]e^{-\alpha\xi}\right\}\left(\eta^4 - 2\eta^2 + 1\right). \tag{3.9}$$

The horizontal velocity may be obtained by differentiating

$$u = -\frac{1}{a}\frac{\partial \psi}{\partial \eta} = -4\,Gr^{*}\left(\frac{\nu}{a}\right)\left\{e^{-a\xi/\lambda} - \left[\cos(\beta\xi) + \gamma\sin(\beta\xi)\right]e^{-\alpha\xi}\right\}\left(\eta^3 - \eta\right). \qquad (3.10)$$

Likewise the vertical velocity can be found from $v = \frac{1}{a}\frac{\partial \psi}{\partial \xi}$

$$v = Gr^{*}\left(\frac{\nu}{a}\right)\left\{-\frac{a}{\lambda}e^{-a\xi/\lambda} + \left[(\alpha - \beta\gamma)\cos(\beta\xi) + (\alpha\gamma + \beta)\sin(\beta\xi)\right]e^{-\alpha\xi}\right\}\left(\eta^4 - 2\eta + 1\right). \qquad (3.11)$$

3.4 COUPLING FLOW MODEL TO MASS TRANSPORT

In a reference frame that moves along the x-axis at the growth velocity v_g so that the growth interface remains stationary in the lab system, the concentration field C is given by the two-dimensional, steady state mass transport equation

$$(u - v_g)\frac{\partial C}{\partial x} + v\frac{\partial C}{\partial y} = D\left[\frac{\partial^2 C}{\partial x^2} + \frac{\partial^2 C}{\partial y^2}\right] \qquad (3.12)$$

where D is the diffusion coefficient.

Assuming a plane front growth interface, the boundary conditions are

$$D\frac{\partial C}{\partial x}\Big)_{x=0} + v_g(1-k)C(0,y) = 0, \quad C(\infty,y) = C_\infty \quad \text{for all y}$$

and

$$D\frac{\partial C}{\partial y}\Big)_{y=\pm a} = 0 \quad \text{for all x}$$

where k is the segregation coefficient.

The concentration field C can be written as

$$C(x,y) = C_\infty\,(C_x(x) + \tilde{C}(x,y)) \qquad (3.13)$$

where C_∞ is the bulk concentration of the melt, C_x is the solution to the steady state, purely diffusive mass transport equation, and $\tilde{C}(x,y)$ is the correction from convective flows in the melt.

An expression for the first order correction from the convective flows can be obtained by assuming that u, v, and $\tilde{C}$ are small so that the second order terms (products of u or v and derivatives of $\tilde{C}$) can be ignored. Dividing the mass transport equation by v_g, inserting eq. (3.13), and retaining only first order terms,

$$\frac{\partial \tilde{C}}{\partial \xi} - \tilde{u}\frac{\partial C_x}{\partial \xi} + \frac{\delta}{a}\left[\frac{\partial^2 \tilde{C}}{\partial \xi^2} + \frac{\partial^2 \tilde{C}}{\partial \eta^2}\right] = 0 \tag{3.14}$$

where $\delta = D/v_g$ and $\tilde{u} = u(x,y)/v_g$.

The $C_x(x)$ is given by

$$C_x(x) = (1/k - 1)\exp(-x/\delta) + 1. \tag{3.15}$$

Let

$$\tilde{u} = \tilde{u}_\xi(\xi)\,\tilde{u}_\eta(\eta) \tag{3.16}$$

and assume that $\tilde{C}(x,\eta)$ can be written as

$$\tilde{C}(\xi,\eta) = f(\xi)\exp(-a\xi/\delta)g(\eta) \tag{3.17}$$

where $f(\xi)$ and $g(\eta)$ are respectively functions of ξ and η only.

Taking derivatives of eq.(3.15) and eq. (3.17), putting them back into eq.(3.14) and rearranging terms, the equation can be written

$$\frac{\partial^2 f(\xi)}{\partial \xi^2} - \frac{a}{\delta}\frac{\partial f(\xi)}{\partial \xi} + (1/k - 1)\frac{a^2}{\delta^2}\frac{\tilde{u}_\xi(\xi)\tilde{u}_\eta(\eta)}{g(\eta)} + \frac{f(\xi)}{g(\eta)}\frac{\partial^2 g(\eta)}{\partial \eta^2} = 0. \tag{3.18}$$

If the $\tilde{u}_\eta(\eta)$ had the same functional form as $g(\eta)$, the variables would separate and $g(\eta)$ could be expressed as a Fourier series. However, the boundary conditions at $\eta = \pm 1$ require $\partial g/\partial \eta = 0$ whereas $\partial \tilde{u}/\partial \eta \neq 0$. Thus it is not possible to obtain a mathematically consistent solution by separation of variables. Guided by the numerical results, it would seem that the η-dependence of C could be reasonably represented by $g(\eta) = -\sin(\pi\eta/2)$. This satisfies the boundary conditions at $\eta = \pm 1$ and, like the $(\eta^3 - \eta)$ term in the expression for u, is antisymmetric with respect to $\eta = 0$. To obtain an approximate solution, the $\tilde{u}$ term in the mass transport equation will be represented by

$$\tilde{u} = -\frac{\pi}{8}\tilde{u}_\xi(\xi)\sin(\eta\pi/2) \tag{3.19}$$

in which the $(\eta^3 - \eta)$ term has been replaced by $-\pi/8\,\sin(\eta\pi/2)$. The coefficient $\pi/8$ was chosen to give the same integrated flow as before, i.e.

$$\int_0^1 (\eta^3 - \eta)d\eta = -\frac{\pi}{8}\int_0^1 \sin(\eta\pi/2)d\eta.$$

Since this flow acts only on the gradient of *Cx*, which is not a function of η, the artificial distortion introduced into the flow field for mathematical expediency should not produce a serious error.

The 2nd order partial differential equation can now be reduced to an ordinary second order differential equation which using eq. (3.10) can be written

$$f''(\xi) - \frac{a}{\delta}f'(\xi) - \frac{\pi^2}{4}f(\xi) = G\left\{e^{-a\xi/\lambda} - \left[\cos(\beta\xi) + \gamma\sin(\beta\xi)\right]e^{-\alpha\xi}\right\} \quad (3.20)$$

where $G = (1/k-1)\frac{a^2}{\delta^2}\frac{\pi}{2}\frac{Gr^*\nu/a}{v_g} = (1/k-1)\frac{\pi}{2}Gr^*Sc\frac{a}{\delta}$

and Sc is the Schmidt number (ν/D)

The solution has the form

$$f(\xi) = G\left\{A_1 e^{-a\xi/\lambda} + \left[A_2\sin(\beta\xi) + A_3\cos(\beta\xi)\right]e^{-\alpha\xi} + A_4 e^{r\xi}\right\} \quad (3.21)$$

where

$$A_1 = \frac{-1}{\frac{a^2}{\lambda^2} + \frac{a^2}{\lambda\delta} - \frac{\pi^2}{4}}, \quad A_2 = \frac{\gamma E - F}{E^2 + F^2}, \quad A_3 = \frac{\gamma F + E}{E^2 + F^2},$$

$$E = 4 + \alpha a/\delta - \pi^2/4, \quad F = \beta(2\alpha + a/\delta).$$

The quantity r is the negative root of the indicial equation, $r^2 - ra/\delta - \pi^2/4 = 0$ which is given by

$$r = \frac{a}{2\delta}\left(1 - \sqrt{1 + \pi^2\delta^2/a^2}\right). \quad (3.22)$$

(Since the perturbation must die out at large x, the second unspecified coefficient corresponding to the positive root of the indicial equation is set to zero.)

The remaining free coefficient, A_4, must be determined from the conservation of solute boundary condition at the interface, i.e.,

$$D\frac{\partial C}{\partial x}\Big)_{x=0} + v_g(1-k)C(0,y) = 0. \quad (3.23)$$

Inserting eq.(13) and eq.(17), this condition requires

3.5 COMPARISON WITH NUMERICAL COMPUTATIONS

The approximate analytical model was extensively tested against numerical computations. The results shown are from the following test case.

$g = 980 \times 10^{-6}$ cm/sec^2
$\beta \Delta T = 0.025$
$D = 0.00013$ cm^2/sec
$\nu = 0.0013$ cm^2/sec
L = 2.5 cm
a = 0.5 cm
$\lambda = 1.0$ cm
k = 0.1
vg = 6.5 μm/sec

The stream function was computed numerically from eq. (3.5) using an equally spaced 21x51 grid and a simple relaxation method. For this computation, the boundary conditions $\psi(\eta,L/a) = \psi'(\eta,L/a) = 0$ were imposed instead of allowing these functions to approach 0 as x goes to ∞ as was done for convenience in the analytical model. Comparison of the numerical results against the stream function calculated from eq. (3.9) is quite good as may be seen from Figure 3.1 which compares the stream function along y = 0 and from Fig. 3.2 which compares the stream lines. The amplitude and location of the peak agree to within a few percent, the slight difference apparently results from the different boundary condition imposed at x = L. The most critical aspect of the model is its ability to predict the horizontal velocity profile in the region of the interface. This it does extremely well as may be seen in Fig. 3.3 which compare the horizontal velocity profiles calculated from eq.(3.10) with the numerical result. Fig. 3.4 compares the maximum horizontal and vertical velicity profiles. Similar comparisons were made for different values of λ as shown in Fig. 3.5 and 3.6. As can be seen, the model improves with increasing λ. The agreement remains quite good for values of $a/\lambda < 1$ where the viscous terms in the core region are dominant, but the model starts to break down for $a/\lambda > 1$ because the assumption that the y-dependence of the stream function in the core region holds everywhere is apparently not valid near the corners. However, the model is still within a factor of 2 of the numerical result as a/λ get large.

The composition profile in the melt was also computed numerically using the same relaxation method. The isoconcentrates calculated by combining eq. (3.15) and eq. (3.26) using the coefficients defined in eq.(3.21) are compared with those computed numerically in Fig. 3.7. The y-dependence of the concentration at the interface is shown in Fig. 3.8. Again the results are virtually identical.

Having demonstrated that the analytical model can faithfully reproduce the essential effects of a small lateral acceleration, comparisons with the results of Alexander, Ouazzani, and Rosenberger (AOR) [7] were then attempted. A choice

$$\left.\frac{\partial f(\xi)}{\partial \xi}\right)_{\xi=0} - \frac{ak}{\delta} f(0) = 0. \tag{3.24}$$

A_4 may now be found using eq. (21)

$$A_4 = \frac{(ka/\delta + a/\lambda)A\neg 1 - \beta A_2 + (ka/\delta + \alpha)A_3}{r - ka/\delta}. \tag{3.25}$$

Finally, the perturbation to the concentration field is obtained by combining eq.(3.17), (3.19) and (3.21) to obtain

$$\frac{\tilde{C}(\xi,\eta)}{C_\infty} = G e^{-a\xi/\delta}\left\{A_1 e^{-a\xi/\lambda} + \left[A_2 \sin(\beta\xi) + A_3 \cos(\beta\xi)\right]e^{-\alpha\xi} + A_4 e^{r\xi}\right\}\sin(\eta\pi/2). \tag{3.26}$$

The concentration at the interface is then

$$\frac{C(0,\eta)}{C_\infty} = 1/k + G\,(A_1 + A_3 + A_4)\sin(\eta\pi/2). \tag{3.27}$$

The segregation along the growth interface is characterized by a segregation parameter ζ defined as the difference between the maximum and the minimum concentration divided by the average composition along $\xi = 0$. Since the maximum and minimum concentration will occur at η =+1 and -1 respectively, and the average concentration will be C_∞/k, we can write

$$\zeta = \left|\frac{C(0,+1) - C(0,-1)}{C_\infty / k}\right| = \left|2kG(A_1 + A_3 + A_4)\right| \tag{3.28}$$

Using the definition for G in eq. (20), this may be written as

$$\zeta = \left|\pi(1-k)\,\frac{Gr\,Sc\,(a/\delta)(A_1 + A_3 + A_4)}{24 - 8(a/\lambda)^2 + (a/\lambda)^4}\right|. \tag{3.29}$$

The quantity $A_1 + A_3 + A_4$ can also be written as

$$A_1 + A_3 + A_4 = \frac{(r + a/\lambda)A_1 - \beta A_2 + (r+\alpha)A_3}{r - k\alpha/\delta} \tag{3.30}$$

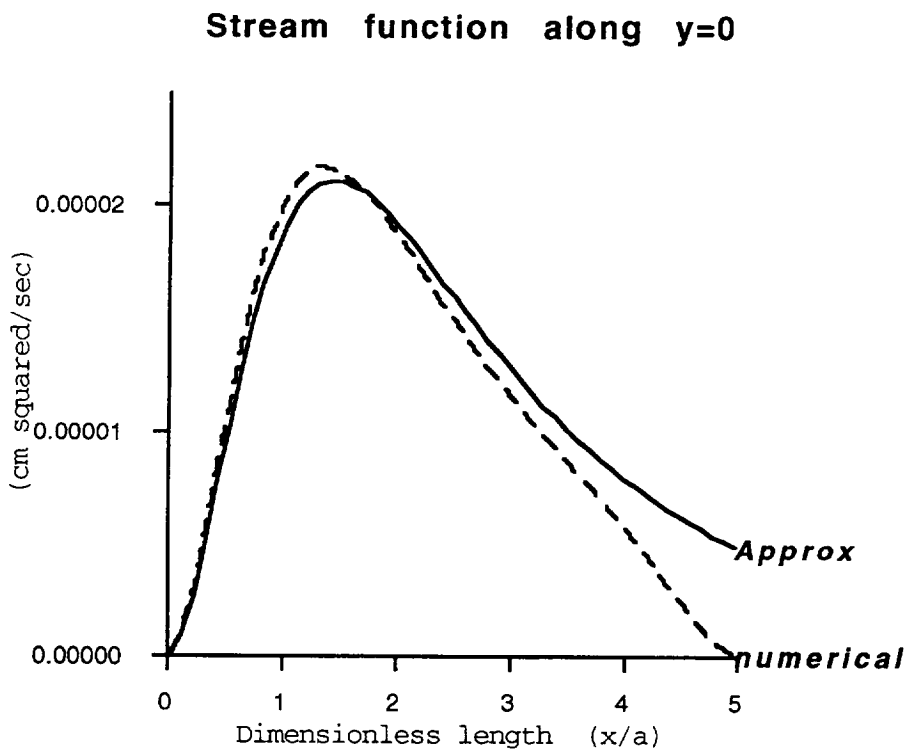

Figure 3.1. Comparison of the approximate solution for stream function along the x-axis with a numerical solution to the flow equations for the test case. The numerical computation was carried out for a finite (2.5 cm long) ampoule, whereas the approximate solution assumed an infinite ampoule. Note the magnitude and shape of the stream function are accurately captured by the analytical model; the major differences being in the boundary conditions at the end.

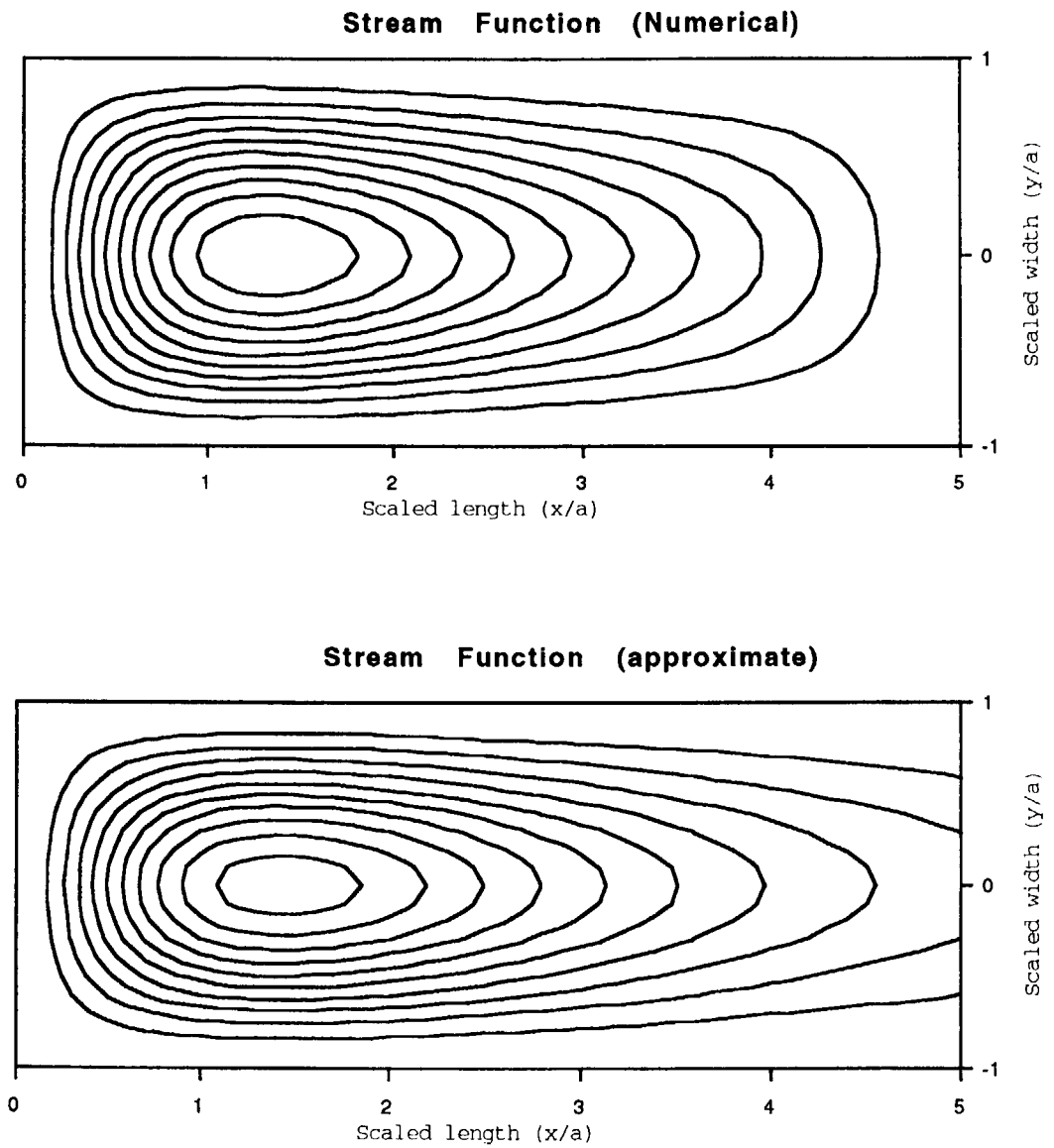

Figure 3.2. Comparison of the 2-dimensional stream function for the test case computed numerically (top) with the approximate analytical model. Contours are 2 x 10^{-6} cm^2/sec.

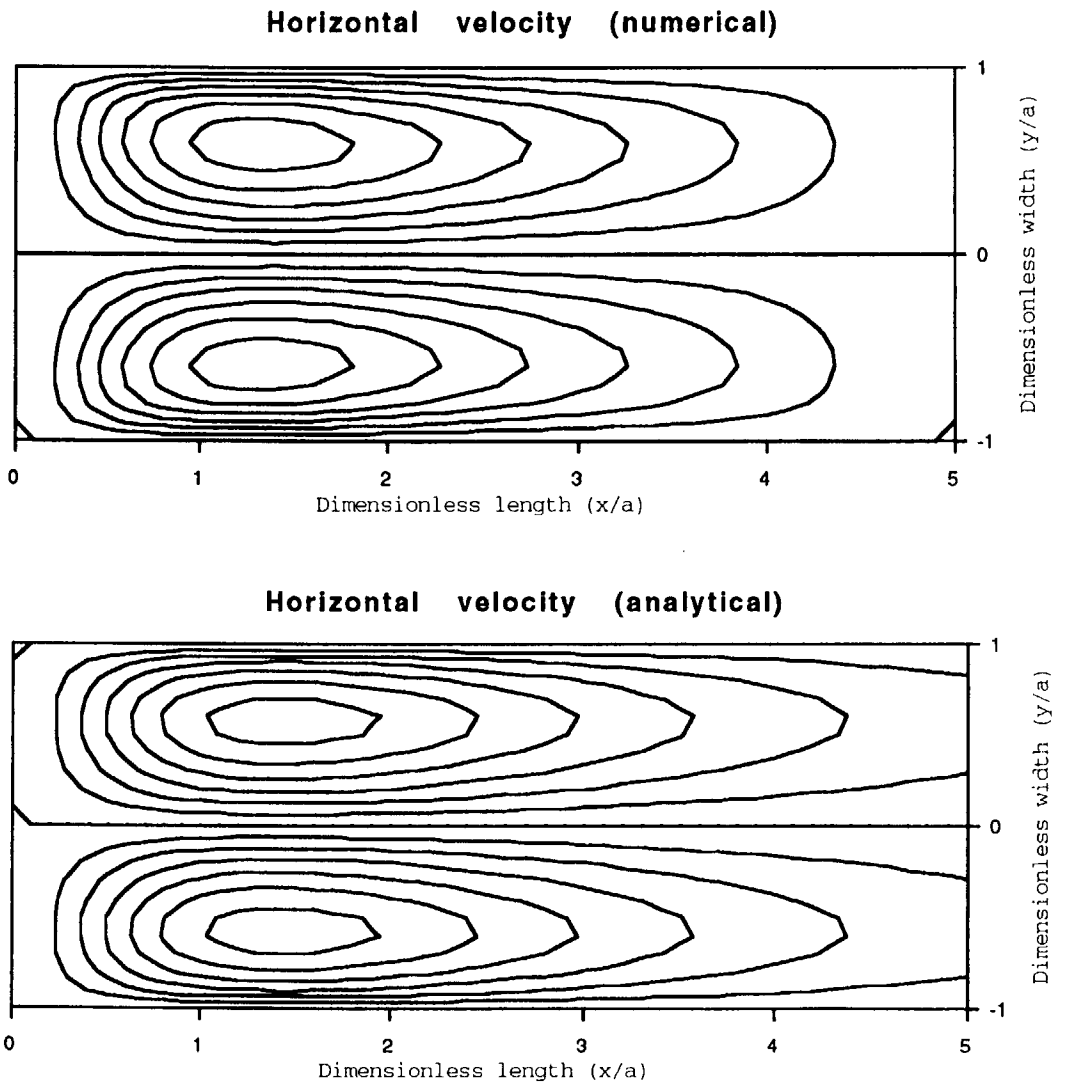

Figure 3.3. Comparison of horizontal velocity field for the test case computed numerically (top) with the approximate analytical model. Contours are 1 x 10^{-5} cm^2/sec.

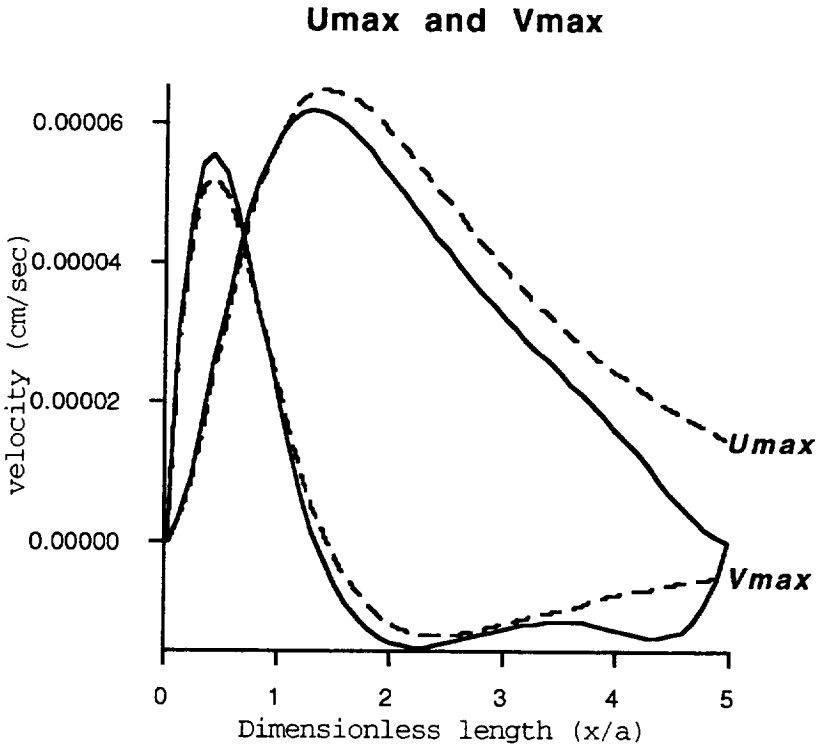

Figure 3.4. Comparison of the maximum horizontal and vertical velocities (dashed lines) calculated from the approximate analytical model with those computed numerically (solid lines).

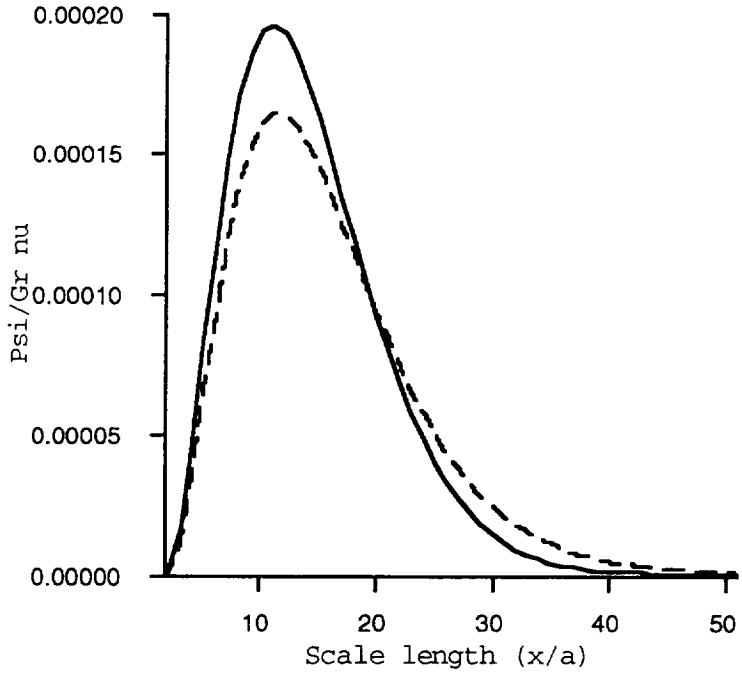

Figure 3.5. Comparison of stream function along $\eta = 0$ computed numerically (solid curve) with the approximate model (dashed curve) for $\lambda = 0.25$ cm, L= 2.5 cm, a = 0.5 cm.

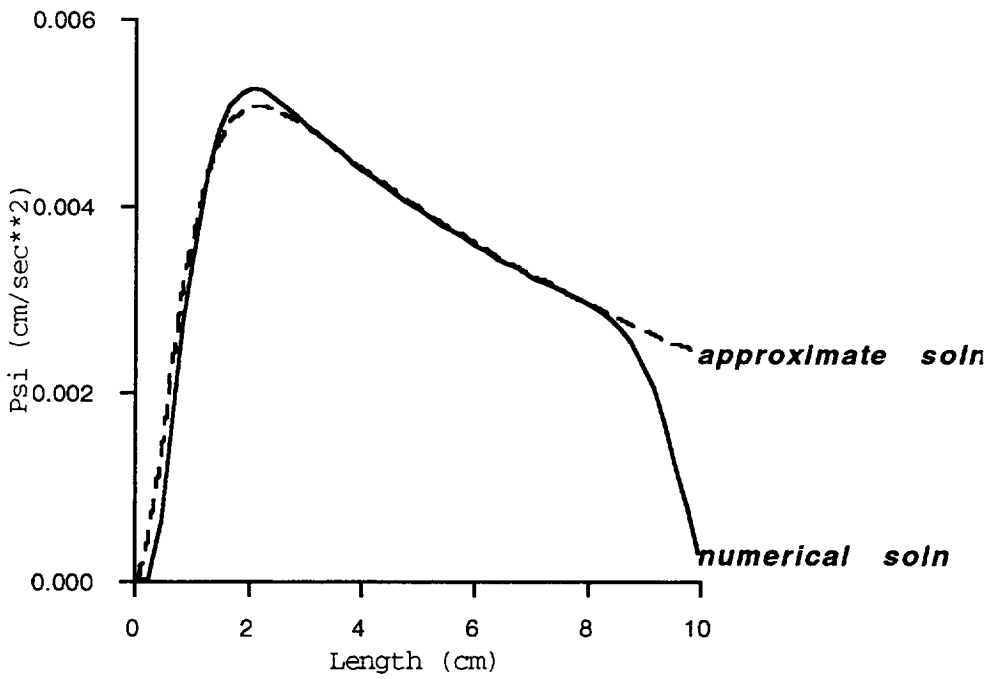

Figure 3.6. Comparison of stream function along $\eta = 0$ computed numerically (solid curve) with the approximate model (dashed curve) for $\lambda = 10$ cm, L= 10 cm, a = 1 cm , Gr ν = 1.582 cm^2/sec.

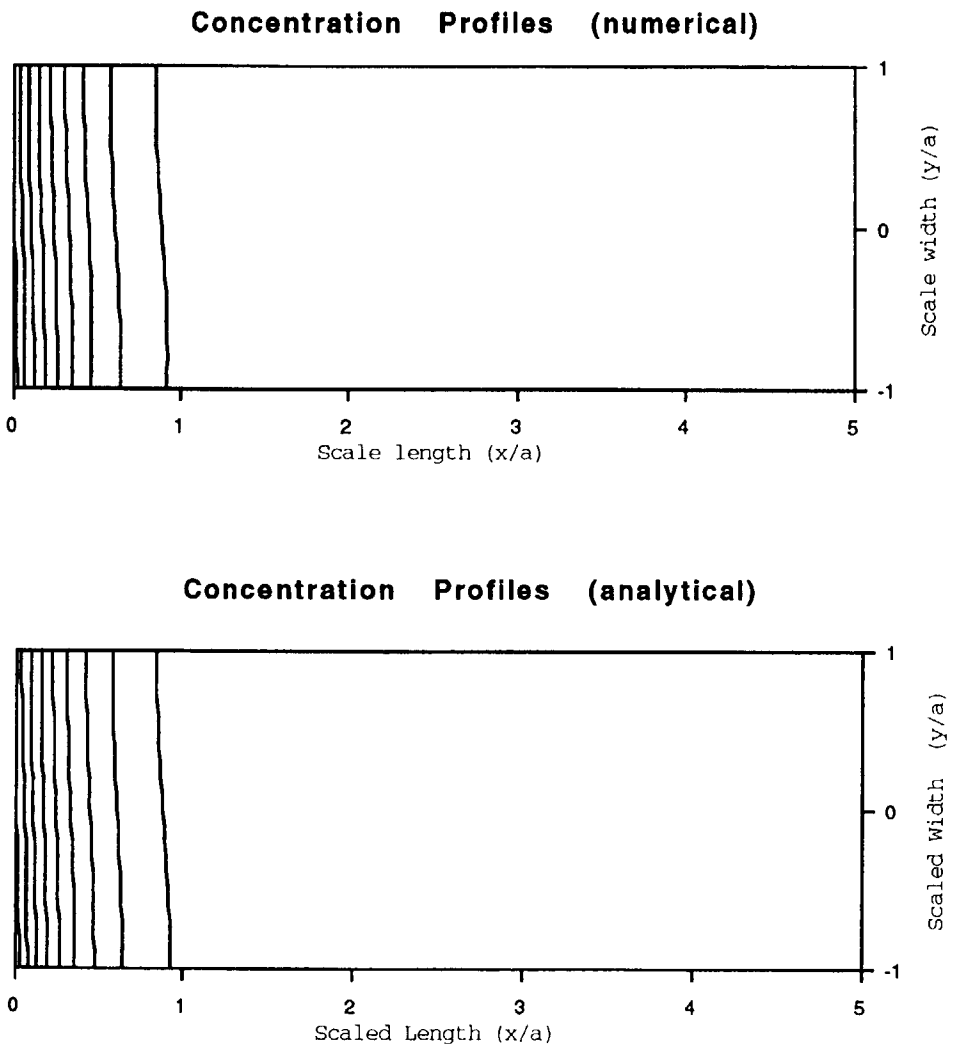

Figure 3.7. Comparison of concentration profiles in the melt for the test case computed numerically (top) with the approximate analytical model. Contours are 2, 3,....10 C_∞

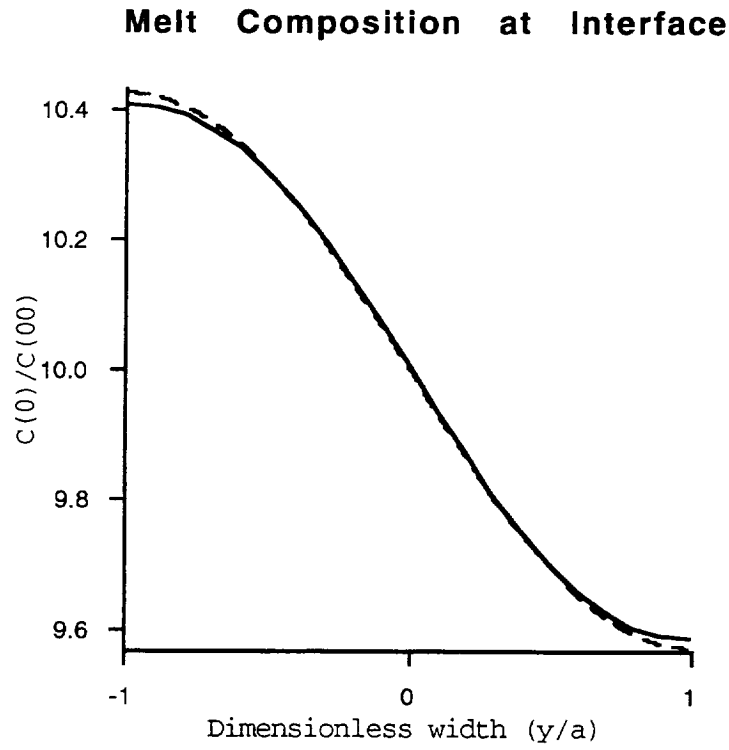

Figure 3.8. Comparison of the compositional profiles in melt at the growth interface for the test case. The solid curve was computed numerically and the dashed curve was calculated from the approximate analytical model.

of $a/\lambda = 2$ produced a density profile that was reasonably similar to that produced by the average axial temperature profile used in the AOR computations. As it turns out, the segregation is not particularly sensitive to the choice of a/λ in this regime as will be shown later.

As may be seen in Table 3.1, the agreement is quite good as long as the perturbation is small (i.e. $\zeta < 1$) which corresponds to Gr Sc less than ~100. Within this range the conditions required for the analytical model to be valid are generally met; i.e., the flows do not perturb the density field significantly and the second order terms in the mass transport equation are small enough to be safely ignored. (In fact, the agreement is quite good beyond this range, but since the perturbation is no longer small, this agreement must be considered fortuitous.) Hence, for Gr Sc < 100, the degree of segregation is directly proportional to the product of Gr Sc (for fixed a/δ). At first glance, this appears to contradict the findings of AOR who argue that the segregation does not depend linearly on Sc. It should be remembered that this model is restricted to small enough flows so that nonlinear effects have not yet manifested themselves. Also, AOR altered the Sc by varying the diffusion coefficient, keeping the growth rate constant. This of course would cause δ to change, thus altering the coefficients defined in eq. (3.21). Actually, for constant values of a/δ, the AOR results appear to scale linearly with Gr Sc up to ~360. Beyond this point the convective mixing becomes such that the segregation is reduced.

Table 3.1

g/g_0	a (cm)	v_g (μm/sec)	ΔT	Gr Sc	a/δ	ζ (AOR)	ζ ($\lambda = 2a$)
10^{-4}	0.50	6.50	100	3600	2.50	0.80	9.54
10^{-5}	0.50	6.50	100	360	2.50	0.927	0.954
10^{-5}	0.50	0.65	100	360	0.25	0.119	0.181
10^{-5}	0.25	6.50	100	45	1.25	0.120	0.089
5×10^{-5}	0.50	6.50	100	1800	2.50	0.542	4.77
10^{-6}	0.50	6.50	100	36	2.50	0.113	0.095
10^{-6}	0.50	0.65	100	36	0.25	0.02	0.018
1.41×10^{-5}	0.50	6.50	115	590	2.50	1.52	1.56
1.41×10^{-6}	0.50	6.50	115	59	2.50	0.215	0.156
1.41×10^{-6}	0.50	0.65	115	59	0.25	0.015	0.024
10^{-5}	0.50	6.50	20	72	2.50	0.226	0.191
10^{-5}	1.00	6.50	20	580	5.00	0.645	1.156
10^{-6}	0.50	6.50	20	7.2	2.50	0.023	0.019

3.6 COMPARISON WITH GARANDET'S RESULTS

Garandet considered the case of a linear thermal gradient which can be duplicated in this model by letting $\lambda \to \infty$. For small Peclet numbers, his order of magnitude analysis obtained a scaling law that estimates the variation in concentration across the interface ΔC to be given by

$$\Delta C = Pe' \frac{Gr' Sc}{768} \frac{(1-k)}{k} C_\infty , \qquad Pe' << 1 \tag{3.31}$$

where his Peclet number $Pe' = v_g H/D$ and Grashof number $Gr' = \beta_T g (\Delta T / L) H^4 / \nu^2$. Comparing this with computer analysis, he adjusted this scaling law by 1/2.3 to obtain agreement with the numerical results. Since ζ is defined as $k \Delta C / C_\infty$, Garandet's adjusted result can be written in terms of the Gr and Pe defined with length scale a instead of H as

$$\zeta = \frac{k \Delta C}{C_\infty} = \frac{Gr\, Sc (1-k)(H/a)^5}{(2.3)\, 768} Pe = 0.0181(1-k) Gr\ Sc\ Pe \tag{3.32}$$

For $\lambda \to \infty$, the segregation parameter given by eq.(29) and eq.(30) reduces to

$$\zeta = \pi (1-k) \frac{Gr\, Sc}{24} Pe \left[\frac{r A_1 - \beta A_2 + (r+\alpha) A_3}{r - k\, Pe} \right] \tag{3.33}$$

where $Pe = a/\delta$.

The coefficients A_1, A_2, and A_3 also simplify and can be written as polynomials of Pe. For small Pe, only the constant terms need be considered. Inserting the numerical values for $\alpha = \sqrt{2+\sqrt{6}}$ and $\beta = \sqrt{-2+\sqrt{6}}$, these coefficients are given by

$$A_1 = 4/\pi^2 = 0.405$$

$$A_2 = \frac{(\alpha/\beta)(4 - \pi^2/4) - 2\alpha\beta}{(4 - \pi^2/4)^2 + 4\alpha^2\beta^2} = 0.193$$

$$A_3 = \frac{2\alpha^2 + 4 - \pi^2/4}{(4 - \pi^2/4)^2 + 4\alpha^2\beta^2} = 1.008 \ .$$

Also for small values of Pe, the r in eq. (3.22) $\approx -\pi/2$ which is >> k Pe. Inserting these values into eq. (3.29) and (3.30), we obtain

$$\zeta = 0.019\ (1 - k)\ Gr\ Sc\ Pe\ , \qquad Pe << 1 \tag{3.34}$$

which is virtually identical with Garandet's result.

For large Pe, Garandet obtains a scaling law from his order of magnitude analysis that predicts

$$\Delta C = \frac{1}{Pe'^3}\frac{Gr'Sc}{48}\frac{(1-k)}{k^2}C_\infty, \qquad Pe' >> 1. \tag{3.35}$$

He finds that he must adjust this result by a factor of 12 to bring it into agreement with numerical results. With this adjustment, the segregation parameter predicted by his model can be written as

$$\zeta = \frac{k\Delta C}{C_\infty} = 12\frac{(1-k)}{k}\frac{GrSc(H/a)}{48}\frac{1}{Pe^3} = 0.500\frac{(1-k)}{k}GrSc\frac{1}{Pe^3}. \tag{3.36}$$

Expanding eq. (3.30) in terms of 1/Pe and inserting the numerical values for α and β, the 1/Pe and $1/Pe^2$ terms vanish leaving

$$A_1 + A_3 + A_4 = \frac{rA_1 - \beta A_2 + (r+\alpha)A_3}{r - kPe} = \frac{-4.883(1/Pe^3) + O(1/Pe^4)}{-kPe}. \tag{3.37}$$

Putting this into eq. (3.29), the segregation is given by

$$\zeta = \pi(1-k)\frac{GrSc}{24}Pe\left[\frac{-4.337(1/Pe^3) + O(1/Pe^4)}{-kPe}\right] \approx 0.639\frac{(1-k)}{k}GrSc\frac{1}{Pe^3}. \tag{3.38}$$

It may be seen that the present model not only gives the same scaling as obtained by Garandet for the case of $\lambda \to \infty$, but also gives very close agreement with his numerical results without any adjustments. This attests to the accuracy of the model.

3.7 EFFECT OF THE EXPONENTIAL GRADIENT

Since neither this model nor Garandet's model imposes boundary conditions on the fluid at the end of the ampoule away from the growth interface, the length L can represent a linear density profile in a semi-infinite ampoule. Figure 3.9 plots the ratio of the segregation resulting from an exponential density profile to that of a linear profile where the densities at 0 and L are the same. (L in this case was taken to be 5 a.) Increasing values of a/λ represent the steepening of the initial density gradient. The effect of the exponential density profile is to enhance the degree of segregation as the initial gradient steepens up to $\lambda \approx a$. The effect is more pronounced for larger values of Pe (smaller δ) because more of the diffusion field is in the steeper part of the gradient where the convective flow is stronger. As the initial gradient steepens beyond a certain point, however, the flow becomes

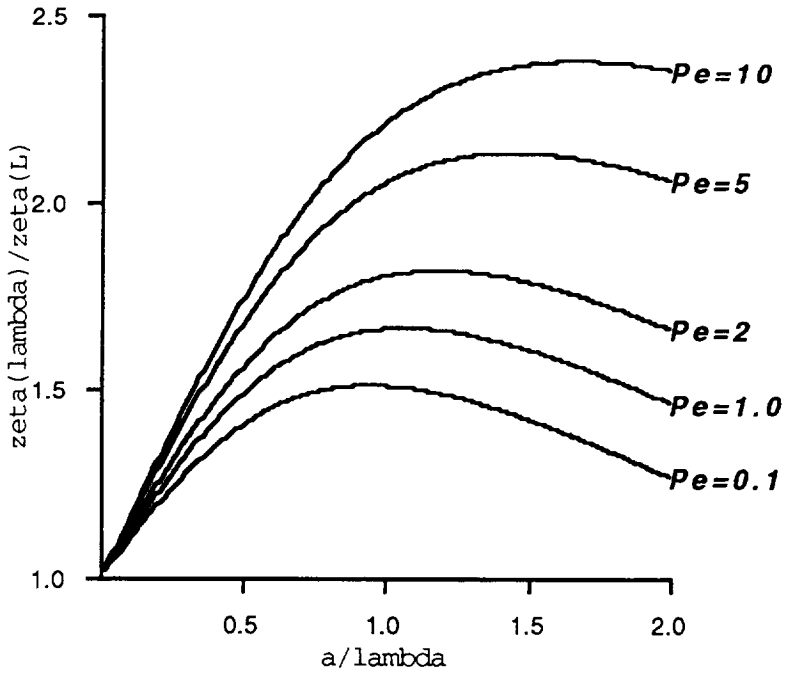

Fig. 3.9 Ratio of the segregation resulting from an exponential density profile to that resulting from a linear density over a distance L = 5 a for k = 0.1. The densities at 0 and L were taken to be the same. $a/\lambda = 1$ represents a linear gradient which steepens as a/λ increases. The $Pe = v_g a / D$ or the ratio of ampoule width to diffusion length.

more confined to the region of the solidification interface which causes the velocity to diminish because of the higher shear forces as may be seen in Fig. 3.10.

The interplay of the steepness of the gradient and the Peclet number can be seen in Figure 3.11. The contours represent the segregation ζ scaled by the product Gr Sc (λ/a). This effectively scales the segregation by a form of the Gr that does not involve λ (i.e. g ($\Delta\rho/\rho$) a^3 / ν^2) so that now as $a/\lambda \rightarrow 0$, the gradient vanishes. It can be seen that the segregation is maximized for Pe ~ 2 for all values of a/λ. The segregation increases with increasing a/λ up to $a/\lambda = 1.4$.

For non-dilute systems where the convective flows are driven primarily by the solutal gradient, $\lambda = \delta$ and a/λ = Pe. The interplay of Pe and k for this situation is shown in Fig. 3.12. Note that the Pe that produces the maximum segregation decreases from 2 for k = 0.1 to 0.8 for k = 10. The interplay of the streamlines and concentration gradient for these two cases under conditions of maximum coupling may be seen by comparing Fig. 3.13 and 3.14. A similar result is obtained for the non-dilute case in which a/λ is fixed.

3.8 SUMMARY AND CONCLUSIONS

In order to study effects of small sustained transverse accelerations on the flow and concentration fields in a Bridgman-Stockbarger crystal growth apparatus, the molten part of the system has been modeled as a fluid in a semi-infinite two-dimensional horizontal slot with a density field that falls off exponentially from one end. It is assumed that the flows are sufficiently weak that the density field is not affected by the flow, thus allowing the flow equation to be solved independently of the mass transport equation. The maximum flow velocity was found to be ~ $Gr\,(\nu/a)/9\sqrt{3}$. Therefore, for dilute systems, in order for the thermal Peclet number ($\nu\,\lambda / \kappa$) < 1, the thermal Rayleigh number g ($\Delta\rho/\rho$) $a^3 / \nu\,\kappa < 15$. Similarly, for non-dilute systems, the solutal Rayleigh number g ($\Delta\rho/\rho$) $a^3 / \nu\,D < 15$. Stabilizing or destabilizing effects of a longitudinal acceleration component have not been considered in this work, although such effects could be extremely important, especially for non-dilute systems.

A closed form approximate solution was obtained for the two-dimensional flow equation by assuming that the cubic y-dependence of the velocity field in the core region holds for all x. This allows the biharmonic partial differential equation for the stream function to be reduced to a fourth-order ordinary differential equation which was solved by the method of Laplace transforms. The resulting solution is a relatively simple expression which can be differentiated to obtain the horizontal and vertical velocity fields. Although this is only an approximate solution, excellent agreement with numerical solutions was obtained provided the gradient region was longer than the half-width of the chamber. This covers most of the region of interest for this application. Even for gradient lengths less than the chamber half-width, the model was within a factor of 2 of the numerical result.

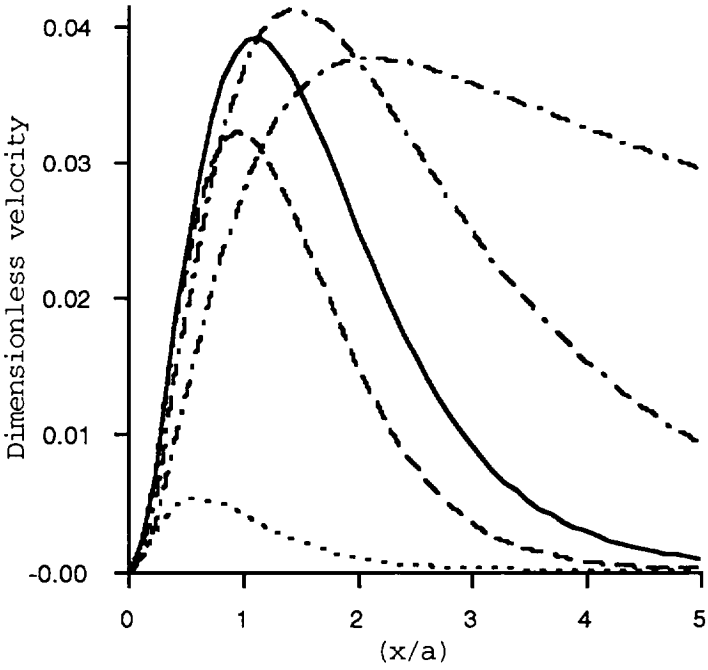

Figure 3.10. Maximum horizontal velocity profile for $\lambda = 0.1$ a (dotted line), $\lambda = 0.5$ a (dashed line), $\lambda = 0.8$ a (solid line), $\lambda = 2$ a (dash-dash-dot line), and $\lambda = 10$ (dot-dash line). The velocity is scaled by Gr (ν/a).

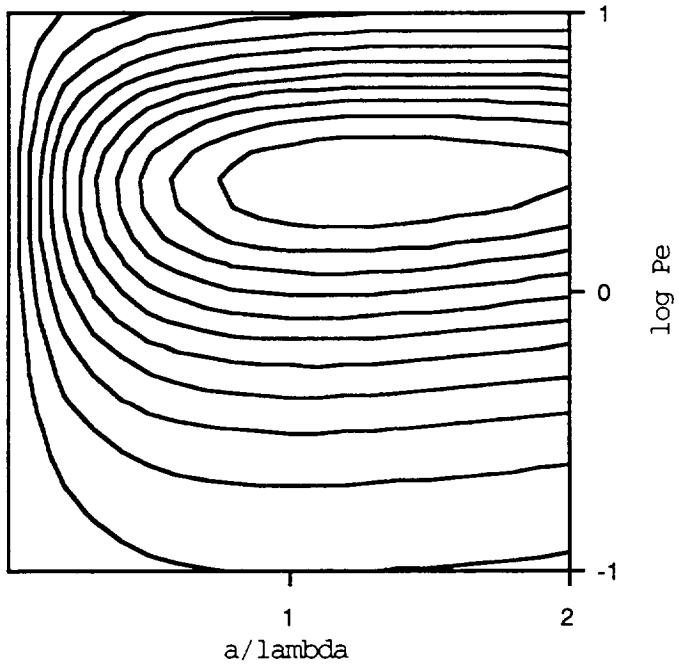

Fig. 3.11. Contour plot of segregation scaled by GrSc(λ/a) for k = 0.1. Peak value is 0.00566 at a/λ = 1.25 and log Pe = 0.3. Contours are spaced at intervals of 0.0005.

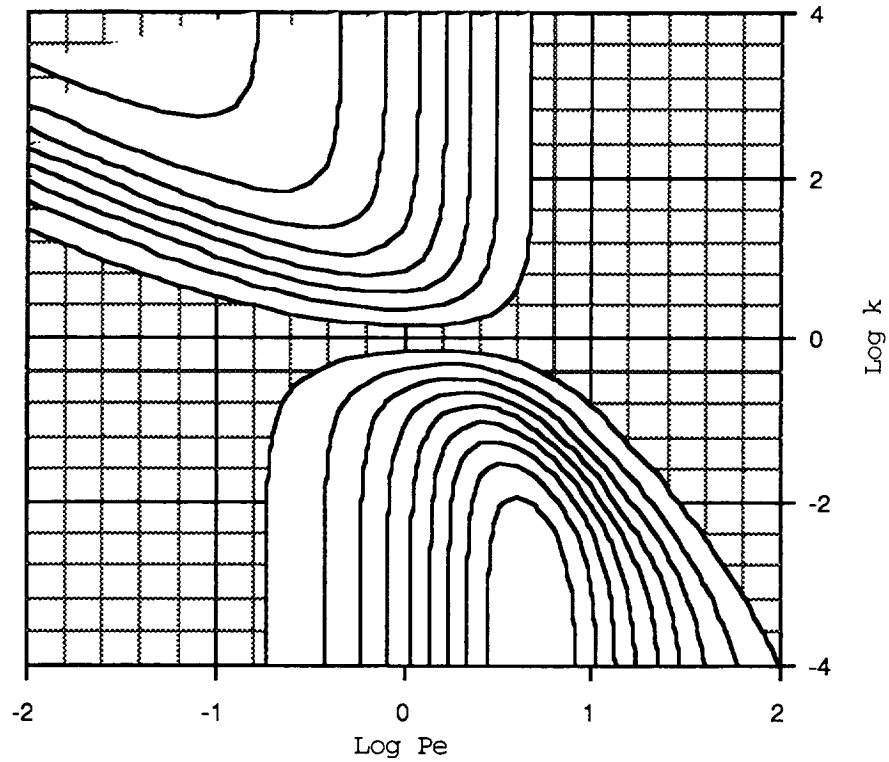

Fig. 3.12. Segregation scaled Gr Sc (λ/a) for the case of solutal-driven convection in which a/λ = Pe. Peak value is 0.096 and contour spacing is 0.001. Note the shift in the Pe that causes the maximum segregation as k goes from 0.1 to 10.

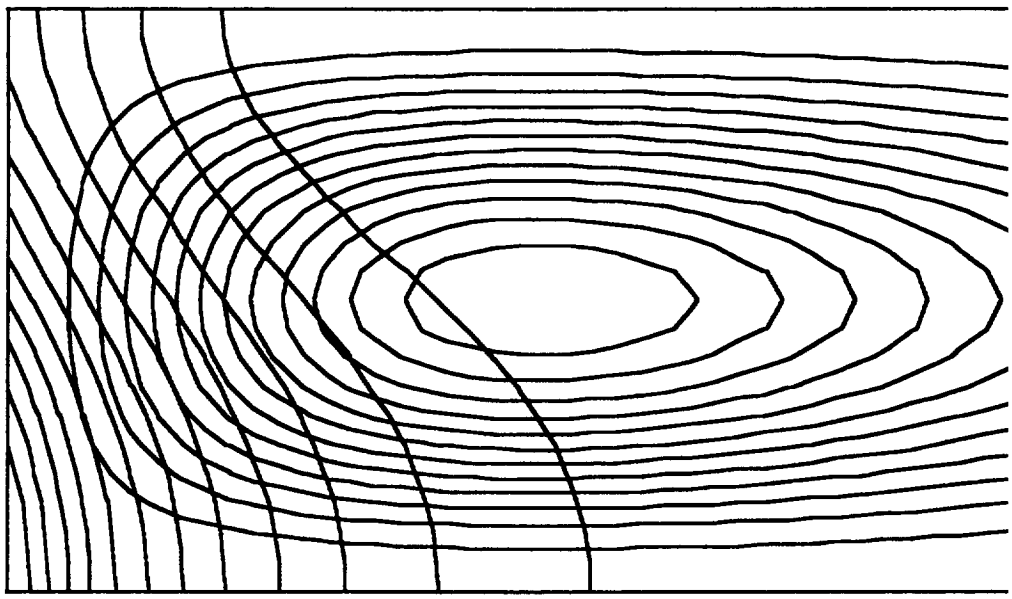

Figure 3.13. Concentration field overlaid on stream function for maximum coupling (Pe = 2.0) between the flow and the concentration gradient for k = 0.1. Isocontours of the concentration field represent 2,3....13 C_∞.

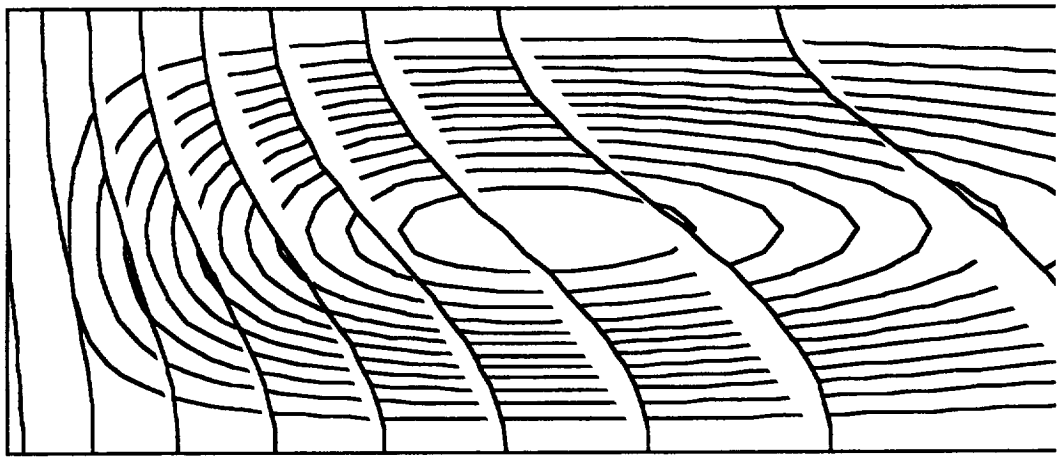

Figure 3.14. Streamlines and Isoconcentrates for maximum coupling (Pe = 0.8) between flow and solute field for non-dilute case with k = 10. Contours are (from the right hand side) 0.9,0.8,.... C_∞.

The resulting expression for the density-driven convective velocity field was then substituted into the mass transport equation and a first-order perturbation solution was obtained for the solute redistribution. This solution is valid so long as the second order terms (i.e. products of the convective velocity and gradients of the perturbed solute concentration field) can be ignored. Since first order terms involve products of the convective velocity and gradients of the unperturbed density field, this condition is met so long as the perturbation is small. This restriction is not serious since the primary purpose of the study was to examine the departures from diffusion-limited concentration fields caused by small transverse accelerations. Again the results from the perturbation solution were found to compare favorably with numerical computations.

With this analytical model, the radial segregation produced by small transverse accelerations could be analyzed as a function of chamber width a, the diffusion length δ, and the e-folding length of the exponential gradient λ. The model was compared with an earlier model developed by Garandet who assumed a linear density profile. In both models the degree of segregation scales as the product of Gr Sc Pe (1 - k) for $Pe = a / \delta << 1$ and as Gr Sc (1 - k)/ k Pe^3 for $Pe >> 1$. By setting λ to ∞ to obtain a linear density profile, the present model produced virtually the same results obtained by Garandet after he had adjusted his scaling analysis to agree with numerical computations. The effect of steepening the gradient (shortening λ) while keeping the density the same at $x = 0$ and at $x = L$ is to increase the degree of segregation by up to several fold, depending on the Pe.

For k = 0.1, the segregation parameter (maximum composition variation along the width of the sample divided by the average composition) can be as high as 0.00567 Gr Sc (λ/a) under conditions of maximum coupling between the flow field and the density field. If compositional variations are to be held to less than 1%, the product Gr Sc (λ/a) < 1.76. Since Sc numbers are generally O(10) for semiconductors, Gr (λ/a) = g ($\Delta\rho/\rho$) $a^3 / \nu^2 < 0.176$. For a typical system such as the Ga-doped Ge modeled by Alexander et al, ($\Delta\rho/\rho = 0.025$, $\nu = 0.0013$ cm^2/sec, a = 0.5 cm), the transverse acceleration must be less than 0.1 micro-g for conditions of maximum coupling. This illustrates the extreme sensitivity of such systems to sustained lateral accelerations.

The situation can be even more critical for non-dilute systems because of the greater density differences due to solutal gradients. Furthermore, many of the II-VI systems of interest (e.g. $Hg_{x-1}Cd_xTe$, $Hg_{x-1}Zn_xTe$, etc. have Sc numbers $O(10^2$-$10^3)$. To achieve compositional uniformity in such systems by simply reducing the effective gravitational acceleration without regard to direction of the steady or quasi-steady component of the residual acceleration, one would have to have residual accelerations considerably less than 0.1 micro-g to assure diffusion limited solute redistribution in any growth system of reasonable scale ($\approx$1 cm in diameter). By understanding the interplay of the various length scales, some relief can be obtained by de-tuning the experiment away from the most sensitive set of conditions. However, in a non-dilute system of given diameter, the only adjustable parameter is the growth velocity. Here, the experimenter has a limited range in

which to work since he must consider the time available to grow a usable amount of material if he wishes to grow at a slower rate, while faster growth would require a higher thermal gradient to stabilize the solidification interface which may not be desirable or achievable.

Therefore, it is clear that simply reducing the effective gravitation acceleration by 5-6 orders of magnitude cannot be expected to achieve diffusion limited growth conditions for the systems of interest. Extreme care must be exercised in controlling transverse accelerations by orienting the furnace axis along the residual acceleration vector. The possible benefits of maintaining a small continuous stabilizing acceleration should be explored as well as the application of a modest axial magnetic field to further damp the residual flows.

3.9 REFERENCES

1. C.J. Chang and R.A. Brown, J. Crystal Growth, 82 (1983) 327
2. D. H. Kim, P. M. Adornato, and R. A. Brown, J. Crystal Growth 89 (1988) 339-356
3. S. R. Coriell, M. R. Cordes, W. J. Boettinger, and R. F. Sekerka, J. Crystal Growth, 49 (1980) 13-28
4. A. F. Witt, H. C. Gatos, M. Lichtensteiger, M. C. Lavine and C. J. Herman, J. Electrochem Soc. 122 (1975) 276-283.
5. A. F. Witt, H. C. Gatos, M. Lichtensteiger, M. C. Lavine and C. J. Herman, J. Electrochem Soc. 125 (1978) 1832.-1840
6. R. K. Crouch, A. L. Fripp, W. J. Debnan, G. A. Woodell, and I. O. Clark, Results from a Compound Semiconductor Crystal Growth Experiment in a Low-Gravity Environment, Electronic Materials and Processing: Proceedings of the First International SAMPE Electronic Conference, Santa Clara CA, Jun 23-23, 1987 330-367
7. J. I. D. Alexander, J. Ouazzani, and F. Rosenberger, J. Crystal Growth, 97 (1989) 285-302
8. J. I. D. Alexander, S. Amiroudine, J. Ouazzani, and F. Rosenberger, J. Crystal Growth, 113 (1991) 21-38
9. D. Camel and J.J. Favier, J. Physique, 47 (1986) 1001-1014
10. J. I. D. Alexander, and F. Rosenberger, Bridgman growth in low gravity: a scaling analysis, in Low gravity Fluid Dynamics, (Ed. J. Koster and R. Sani) AIAA 1990
11. R. J. Naumann, and C. Baugher, J. Crystal Growth, 121 (1992) 751-768
12. J. P. Garandet, J. Crystal Growth, 125 (1992) 112-120
13. G. K. Batchelor, Quart. Appl. Phys., XII (1954) 209-233
14. A. Bejan and C. L. Tien, Int. J. Heat Mass Transfer, 21 (1978) 701-708
15. J. E. Hart, J. Atms. Sci. 29 (1972) 687-697
16. D. E. Cormack, L. G. Leal and J. Imberger, J. Fluid Mech. 65 (1974) 209-231
17. D. E. Cormack, L. G. Leal and J. H Seinfeld, J. Fluid Mech. 65 (1974) 231-246
18. J. Imberger, J. Fluid Mech. 65 (1974) 2247-260

SECTION 4

PREDICTIONS OF EFFECTS OF RESIDUAL ACCELERATIONS ON USML-1

The effects of residual accelerations on Bridgman growth of dilute systems can be estimated from the following:

For accelerations along the axis of the furnace, the maximum convective velocity is given by [1],

$$\hat{w} = -\frac{g\,\gamma(\Delta T)\,a^2}{48\,\nu} \quad . \tag{4.1}$$

The perturbation in the concentration field at the growth interface is

$$\tilde{C}(r,0) = Pe \sum_{n=1} E_n\, J_0(r\, s_n)\, f_n(0) \tag{4.2}$$

where the Peclet number $Pe = \hat{w} / v_g$,

$$E_n = -\frac{64}{J_1(a\, s_n)} \left[\frac{1}{(a\, s_n)^3} - \frac{6}{(a\, s_n)^5}\right],$$

and

$$f_n(0) = \frac{2\,G}{r_n - k\alpha} \left[\frac{\beta^3 + r_n\left(3\,\beta^2 + 3\,\alpha\,\beta + \alpha^2 + s_n^2\right) + s_n^2\,(3\,\beta + \alpha)}{\left(\beta^2 + \alpha\,\beta - s_n^2\right)^3}\right].$$

The parameters α, β, and s_n are reciprocal lengths given by

$$\alpha = D/v_g\,,\ \beta = 1/\lambda,\ \text{and}\ s_n = \xi_n \tag{4.3}$$

where ξ_n are the zeros of J_0 and λ is the thickness of the momentum boundary layer of the flow across the face of the growth interface. This is estimated to be half the distance to the point where the density difference is balanced. For thermally driven convection, it is assumed that the thermal profile is given by

$$T(z) = (T_\infty - T_{melt})(1 - e^{-z/\delta}) - T_{melt} \tag{4.4}$$

where the thermal length $\delta = (T_\infty - T_{melt})$ / the imposed thermal gradient. The λ is then given by $\lambda = \delta\, \ln(2)/2$.

The quantity r_n is given by

$$r_n = \frac{\alpha}{2}\left(1 - \sqrt{1+4\, s_n^2/\alpha^2}\right) \tag{4.5}$$

and G is

$$G = -\,(1-k)\,\alpha^2\,\beta^2\,\frac{e^2}{4}\,\frac{C_\infty}{k}. \tag{4.6}$$

The effects of lateral acceleration may be found using a modification of the procedure outlined in [1]. In this case the maximum velocity is given by

$$u_{max} = \frac{\gamma (T_{hot} - T_{melt})\, a^3\, g}{9\sqrt{3}\,(a+2\lambda)\,\nu}\,. \tag{4.7}$$

The maximum perturbation in the concentration field at the growth interface is given by

$$\tilde{C}(r,0) = Pe \sum_{n=1} F_n \sin(2\, n\, \pi\, r/a)\, f_n(0) \tag{4.8}$$

where

$$F_n = \frac{-18\sqrt{3}\,(-1)^n}{\pi^3\, a^3}.$$

4.1 Se-doped GaAs

For the growth of Se-doped GaAs (Dave Matthiesen's experiment) the following are assumed:

$a = 0.75$ cm
$\gamma = 5 \times 10^{-4}$ /K
$T_{hot} = 1255°C$
$T_{melt} = 1238°C$
grad $T)_0 = 10$ K/cm
$\langle \Delta T \rangle = 1.7$ K
$k = 0.1$
$\nu = 2.98 \times 10^{-3}$ cm^2/sec
$D = 1 \times 10^{-4}$ cm^2/sec
$v_g = 2.5 \times 10^{-4}$, 5×10^{-4} cm/sec.

From the thermal profile, the momentum boundary layer of the radial flow was estimated to be $\lambda = 0.589$ cm. The computed maximum convective velocity is 3.3 (g/g_0) cm/sec for acceleration along the furnace axis. For $v_g = 2.5 \times 10^{-4}$ cm/sec, the maximum perturbation is $\tilde{C} = 497(g/g_0)C_\infty / k$ which implies the radial segregation will be $\zeta = 497$ (g/g_0). **Therefore, if $\zeta < 1\%$, the maximum steady acceleration along the furnace axis must be < 20 micro-g's.**

For the second growth rate, $v_g = 5 \times 10^{-4}$ cm/sec, $\zeta = 577$ (g/g_0). **Therefore, the maximum steady acceleration along the furnace axis must be < 17 micro-g's.**

For transverse accelerations, the $u_{max} = 39$ (g/g_0) .For $v_g = 2.5 \times 10^{-4}$ cm/sec, the maximum perturbation amplitude is $\tilde{C} = 7000(g/g_0)C_\infty / k$. For this case the difference between the maximum and minimum composition is twice the perturbation amplitude. Thus the radial segregation will be $\zeta = 1.4 \times 10^4$ (g/g_0). **Therefore, for $\zeta < 1\%$, the transverse acceleration must be <0.7 micro-g.**

For the second growth rate, $v_g = 5 \times 10^{-4}$ cm/sec, $\zeta = 1.7 \times 10^4$ g/g_0. **Therefore, the maximum steady transverse acceleration must be < 0.6 micro-g's.**

Several of the physical properties that were needed in the calculation are not well known, e.g.. γ and D, and had to be estimated. It is believed, based on values for similar systems, that these estimates are probably within a factor of 2 of the correct value..

This experiment has fairly modest requirements for acceleration along the axis because of the low thermal gradients in the melt. Even so, the radial distribution is extremely sensitive to transverse accelerations owing to the fairly large diameter and small distribution coefficient. Since the melt is confined by a spring loaded plunger, there are no free surfaces and, as was shown in [1], the effect of periodic accelerations falls as the inverse cube of the frequency for frequencies greater than 10^{-4} Hz. **Therefore, this experiment will be virtually immune to crew-induced vibrations on the Shuttle.**

4.2 CdZnTe

For the $Cd_{.95}Zn_{.05}Te$ experiment (Dave Larson's experiment), the following parameters were assumed:

a = 0.75 cm
$\gamma = 5 \times 10^{-4}$ /K
T_{hot} = 1115°C
T_{melt} = 1095°C
grad $T)_0$ = 10 K/cm
$<\Delta T>$ = 2.0 K
k = 1.2
$\nu = 4.35 \times 10^{-3}$ cm^2/sec
$D = 1 \times 10^{-4}$ cm^2/sec
$v_g = 4.4 \times 10^{-5}$ cm/sec

The small mole fraction of the ZnTe component and the near unity distribution coefficient for this system allow it to be approximated as a dilute alloy in which buoyancy forces are dominated by thermal rather than solutal effects. From the thermal profile, the momentum boundary layer of the radial flow was estimated to be λ = 0.695 cm. For steady accelerations along the axis, the computed maximum convective velocity is $\hat{w} = 2.64(g/g_0)\,cm/sec$. The maximum perturbation is $\tilde{C} = 17(g/g_0)C_\infty / k$ which implies the radial segregation will be ζ = 17 (g/g_0). **Therefore, if ζ < 1%, the maximum steady acceleration along the furnace axis must be < 588 micro-g's.**

For transverse steady accelerations, the maximum convective velocity is estimated to be 28 (g/g_0) cm/sec which gives a maximum perturbation in the concentration field at the growth interface $\tilde{C} = 208(g/g_0)C_\infty / k$. The radial segregation is ζ = 416 (g/g_0). **Therefore, for ζ < 1%, the transverse acceleration must be <22 micro-g.**

The modest temperature gradients, low solute concentration, and near unity distribution coefficient (k value) for this experiment combine to require very modest acceleration requirements, especially along the furnace axis. There will be a small void in the melt to allow for thermal expansion will may make the system more susceptible to transient and periodic accelerations (g-jitter), but the relative insensitivity of the system to steady accelerations will serve to reduce such effects. Therefore, it is not expected that any effects from non-steady accelerations will be observed.

4.3 HgZnTe

This is a non-dilute system in which both thermal and solutal gradients drive significant convective flows. For the case of axial accelerations, the solutal gradient and the radial thermal gradient responsible for radial segregation are perpendicular to one another. This produces a coupling between the perturbed concentration field and thermally driven convection. Since the model [1] for radial segregation caused by accelerations along the furnace axis does not

consider this coupling, it is no longer valid. However, for transverse accelerations, the solutal and thermal gradient are in the same direction and for small flows the model can still be used with minor modifications.

For the $Hg_{.84}Zn_{.16}Te$ experiment (Alex Lehoczky's experiment), the following parameters were assumed:

$a = 0.4$ cm
$\gamma = 5 \times 10^{-4}$ /K
$T_{hot} = 800°C$
$T_{melt} = 695°C$
grad $T)_0 = 60$ K/cm
$<\Delta T> = 15$ K
$k = 4.35$
$\nu = 8.0 \times 10^{-3}$ cm^2/sec
$D = 6 \times 10^{-6}$ cm^2/sec
$v_g = 4.1 \times 10^{-6}$ cm/sec
$\rho_{HgTe} = 8.0$
$\rho_{ZnTe} = 5.35$

The formula for u_{max} must be modified by substituting the total $\Delta\rho/\rho$ for $\gamma(T_{hot} - T_{melt})$. The density profile along the axis is given by

$$\frac{\Delta\rho(z)}{\rho} = \gamma(T_{hot} - T_{melt})e^{-z/\delta_{Thermal}} + .16\,\frac{(\rho_{HgTe} - \rho_{ZnTe})}{\rho_{Hg_{.84}Zn_{.16}Te}}\left(\frac{k-1}{k}\right)e^{-z/\delta}$$

where it is assumed that the density of the alloy is the weighted average of the two components. The composition profile falls to its half-value at 1.03 cm, thus λ is taken to be 0.56 cm.

From these values, $u_{max} = 31.63\ (g/g_0)$ cm/sec, $\bar{C} = 1.28 \times 10^4\,(g/g_0)C_\infty / k$, and $\zeta = 2.6 \times 10^4\ (g/g_0)$. **Therefore, for $\zeta < 1\%$, the transverse acceleration must be <0.38 micro-g.**

4.4. Protein Crystal Growth

Protein crystals grown from solution will be accompanied by a convective growth plume that flows along the side of the growing crystal as solute is taken up leaving a lower density depletion boundary layer. The velocity of the plume and the width of the boundary layer (the distance away from the surface where the velocity is maximum) can be estimated [2] from the approximate solution of Goldstien to the classical problem of free convective flow along a vertical heated plate [3].

$$v_{max} = 0.776\left(\frac{Gr}{Sc}\right)^{1/2}\frac{\nu}{h}$$

$$\delta = 1.31\frac{h}{(Gr\,Sc)^{1/4}}$$

where h is the height of the crystal, Sc is the Schmidt number (ν/D), and the Grashoff number $Gr = g(\Delta\rho/\rho)h^3/\nu^2$. For a large protein crystal assume

h =0.1 cm
ν = 0.01 cm/sec^2
D = 10-6 cm/sec^2
$\Delta\rho/\rho$ = 0.01.

The Gr = 98 (g/g_0), the boundary layer thickness is $\delta = 42(g/g_0)^{-1/4}$ μm and v_{max} = 77 $(g/g_0)^{1/2}$ μm/sec. In order to have diffusion controlled transport, this boundary layer thickness must be >> the chemical diffusion length h/2 = 500 μm. This requires $(g/g_0) << (42/500)^4 = 5x10^{-5}$. **Therefore, in order to assure diffusive controlled growth of protein crystals, the continuous residual acceleration must be < 5 micro-g's.**

The constant attitude required for the CGF experiments may have an unwanted effect on protein crystal growth in that the crystals will continue to migrate in the same direction at their Stokes velocity given by

$$v_{Stokes} = \frac{2\,g(\Delta\rho/\rho)a^2}{9\nu}$$

For the above case, assuming a density difference between the crystal and the solution of 0.1 gm/cm^3, v_{Stokes} = 5 (g/g_0) cm/sec. **Even at a steady acceleration of 1 micro-g, the crystals will migrate 1 cm in slightly more than two days. This will cause them to grow against the container walls which is believed to be undesirable from the stand point of growth conditions. This has not been a problem on previous missions because the attitude was not held constant for long enough periods of time for this to occur.**

Since the response time to a diffusion process goes as a^2/ν for momentum diffusion and a^2/D for chemical diffusion, protein crystal growth may be more sensitive to the higher frequency accelerations because of the much shorter lengths scales involved. For growing crystals that are 100 μm in diameter, the response time for flow is only 2.5 milliseconds. Therefore, periodic disturbances with frequencies less than 64 Hz will produce flows approaching their steady state magnitude in the vicinity of the growing crystal. The chemical diffusion times are of course much slower, and the effects may not be felt with regard to diffusive transport. **However, if flows of a few 10's of microns/sec actually affect the attachment kinetics as some experiments have suggested [4,5],**

milli-g accelerations with frequencies in the 1-60 Hz range could have an effect on the growth of such crystals.

4.5 Marangoni Convection in Closed Containers

The Marangoni Convection in Closed Containers experiment consists of a partially filled cylindrical tube (length L = diameter) containing water or a fluorocarbon oil. A longitudinal thermal gradient is applied an the behavior of the fluid is to be observed. The buoyancy contribution to any flows that might be observed is given by

$$u_{max} = \frac{g(\Delta\rho / \rho)L^2}{144\sqrt{3}}$$

For L = 2.54 cm and $\Delta T = 20°C$, the $\Delta\rho/\rho$ for water is 0.0068. The u_{max} is 17.32 (g/g_0). At 1 micro-g the flow will be 0.17 microns/sec. In an observation time of 5 minutes, the marker particles will move only 52 microns - approximately half their diameter. **Therefore, the contribution from buoyancy driven flows will be undetectable in this experiment. 0**

4.6 References:

1. Naumann, R. J. and C. Baugher, Analytical Estimates Of Radial Segregation In Bridgman Growth From Low-Level Steady And Periodic Accelerations, Accepted for publication in J. Crystal Growth, March 1992

2. Naumann, R. J. "Unsolved Mysteries of Protein Crystal Growth," Opportunities and Challenges in Crystallization Research, Proceedings of a Workshop Sponsored by the National Science Foundation, E. I. du Pont de Nemours & Co., Eastman Chemical Company, and Hoffmann La Roche Inc., Iowa State University, Ames, Iowa, March 4-6, 1991, pp 265-287.

3 Goldstein, S. Modern Developments in Fluid Mechanics, Oxford: Clarendon Press (1938) p.642

20. Nyce, T. A., and F. Rosenberger, Growth of Protein Crystals Suspended in a Closed Loop Thermosyphon, J. Crystal Growth 110 (1991) 52-59

4. Pusey, M., W. K. Witherow, and R. J. Naumann, "Preliminary Investigations into Solutal Flow About Growing Tetragonal Lysozyme," J. Crystal. Growth, 90,105-111 (1988).

5. Nyce, T. A., and F. Rosenberger, Growth of Protein Crystals Suspended in a Closed Loop Thermosyphon, J. Crystal Growth 110 (1991) 52-59

SECTION 5

RESULTS AND RECOMMENDATIONS

5.1 USML-1 RESULTS

As stated previously, the estimates of the g-levels required to effectively eliminate radial segregation in the furnace experiments that were made prior to the launch of USML-1 were based of the best model available at that time. Since it was expected that the USML-1 would be flown such that the residual acceleration would be along the furnace axis, the major attention up to that point had been given to predicting radial segregation caused by accelerations in the axial direction. In the post mission analysis, it became clear that unexpected forces, thought to be associated with the operation of the flash evaporator system, produced significant transverse accelerations. This was first noticed when the direction of the ball motion in the passive accelerometer (PAS) did not coincide with the furnace axis [3]. The OARE accelerometer indicated a transverse acceleration of 0.5 - 1.0 micro-g which turned out to be somewhat larger than the axial acceleration due primarily to atmospheric drag [2]. This prompted the development of a more accurate model for the effects of transverse accelerations on Bridgman growth experiments which is described in Section 3. Using the results from this model, a new set of predictions for the melt growth experiments for calculated and are displayed in Table 5.1. As can be seen by comparing the prediction in Section 4 with Table 5.1, the more accurate model requires more stringent control of the transverse accelerations, particularly for the case of large Sc as in the case of Lehoczky's experiment.

5.1.1 Lehoczky's Experiment

Lehoczky's experiment was prematurely terminated shortly after the time at which steady state growth was achieved. However, the portion of the sample grown under steady state conditions strongly suggested the presence of an unanticipated transverse acceleration based on the interface shape, radial composition, and quenched-in dendrite structure. [3]. The radial segregation was measured to be 0.4 on one side and 0.18 on the other. The predicted value was 0.192 is of the right order of magnitude, but is somewhat less than observed. The primary difference is believed to be due to the fact that the model assumes a flat interface perpendicular to the growth ampoule; whereas, in the actual experiment, the interface was tilted due to the tendency of the denser rejected solute to slump to the side of the ampoule in the direction of the transverse acceleration.

5.1.2 Larson's Experiment

Larson's experiment is relatively insensitive to convective mixing because the k-value is close to 1 and, in fact, it is possible to achieve near diffusion control of solute distribution on the ground. Also, the melt did not completely fill the ampoule and, because of the unexpected transverse acceleration, the melt solidified along one side of the ampoule leaving a free surface along the other

Table 5.1

Sensitivity of USML-1 experiment to 1 micro-g transverse acceleration.

	Matthiesen Se:GaAs	Matthiesen Se:GaAs	Larson $Cd_{.95}Zn_{.05}Te$	Lehoczky $Hg_{.84}Zn_{.16}Te$
a (cm)	0.75	0.75	0.75	0.4
$\Delta\rho/\rho$	0.0085	0.0085	0.01	0.0956
λ (cm)	1.7	1.7	2.0	1.6
k	0.1	0.1	1.2	4.35
ν (cm^2/sec)	0.003	0.003	0.00435	0.008
D (cm^2/sec)	10^{-4}	10^{-4}	10^{-4}	6×10^{-6}
vg (cm/sec)	2.5×10^{-4}	5×10^{-4}	4.4×10^{-5}	4.1×10^{-6}
Gr	0.39	0.39	0.218	0.094
Sc	30	30	43.5	1333
δ(cm)	0.4	0.2	2.273	1.463
a/λ	0.441	0.441	0.375	0.249
a/δ	1.875	3.75	0.33	0.273
umax (cm/sec)	1.9×10^{-5}	1.9×10^{-5}	1.45×10^{-5}	1.75×10^{-5}
vmax (cm/sec)	1.5×10^{-5}	1.5×10^{-5}	1.1×10^{-5}	1.23×10^{-5}
ζ	0.047	0.042	0.002	0.192

side. This violates the thermal and fluid no-slip boundary conditions assumed in the model and allows the presence of Marangoni flow which could seriously affect the solute redistribution. Mention was made of the fact that radial segregation was disturbed by the asymmetric acceleration and thermal fields in the flight sample, but details have not yet been reported [4].

5.1.3 Matthiesen's Experiment

Matthiesen used a spring loaded PBN plunger to eliminate free surfaces in his experiment [5]. The axial dopant distribution in his first ingot indicated diffusion-controlled growth initially, but indicated complete mixing after the first rate change. The second ingot exhibited complete mixing throughout the entire growth regime. In both cases, large voids were found in the solid, apparently produced by gas bubbles in the melt. Radial segregation was reported to be from 0.3-0.5 in both the ground control as well as in the flight samples. This appeared to be primarily due to the large interface curvature imposed by the thermal profile.

It is difficult to understand how transverse accelerations of the order of 1 micro-g could produce flows greater than the translation velocity which would be required for complete mixing to occur. It is more likely that temperature gradients across the bubbles that formed produced Marangoni flows that could easily account for the complete mixing of the solute [6].

5.1.4 Other experiments

None of the other primary experiments on USML-1 offer the possibility of testing the models developed in this study. Vapor crystal growth experiments, such as performed by Wiedemeier, are relative immune to low level accelerations because of the high kinematic viscosity and low Schmidt numbers of vapors which greatly reduces the Gr Sc product. Estimates were made of the accelerations required to achieve diffusion controlled growth conditions in the protein crystal growth experiments of DeLucas et al. These were apparently achieved and some excellent crystals were grown, but since the influence of low level accelerations on the perfection of protein crystals growing from solution is not understood, these experiments offer no definitive test of the models. Similar statements apply to the zeolite crystal growth experiments.

The surface tension driven convection experiment of Ostrach was so completely dominated by surface tension forces that it would be virtually impossible to extract any buoyancy-driven effects. Small surface fluctuations were reported that appeared to correlate with the vernier thruster firings, but these did not affect the observed flows [7].

The drop physics experiments only required g-levels low enough to be neutralized by the acoustic positioning field which apparently was the case on USML-1.

For the most part, the Glovebox experiments were qualitative rather than quantitative in nature. The Passive Accelerometer System (PAS) did provide independent verification of the direction and magnitude of the quasi-steady residual acceleration using a model based on Stokes' law modified to account for wall effects [1].

An attempt to observe flows resulting from transient accelerations from thruster firings was made using the cell containing water in the Marangoni Convection in Closed Containers (MCCC) experiment [6]. (Water surfaces are so easily contaminated with surface active impurities that the Marangoni effect is not observed unless extreme precautions are taken.) This cell, which contained marker particles illuminated by a light sheet was to have been placed in the back of the glove box and observed with a video camera for a number of hours while other experiments were being performed in the glove box. Unfortunately, this data was apparently not recorded for reasons that are not clear.

Small crystals that were nucleated during the Nucleation of Crystals from Solution (NCS) experiments were observed to drift toward the chamber wall under the influence of microgravity [8], but no quantitative data were recorded.

Several abrupt shifts in the particle distribution were seen during the long (20 minute) runs of the Particle Dispersion Experiment (PDE) which were attributed to vernier thruster firings. These shifts did not affect the experiment, and, in fact, provided information in distinguishing which particles were free floating from those that were stuck to the wall [9].

5.2 SUMMARY

It has been shown for dilute systems grown by the Bridgman method that the radial segregation produced either by an axial and by a transverse low-level quasi-steady acceleration scales as (1-k) Gr Sc f(a/λ, a/δ, and k) where Gr is calculated with the radial thermal gradient in the case of axial acceleration, and with the axial thermal gradient in the case of transverse acceleration. (The function of (a/λ, a/δ, and k) is of course different for the two cases.) Since the axial gradients are generally greater than the radial gradient, transverse accelerations are considered more critical. The transverse result also applies to the case of a non-dilute system provided the Gr Sc is small.

For the case of a dilute system with a linear axial thermal gradient, Garandet [10] showed that the radial segregation caused by a steady transverse acceleration is given by

$$\zeta = \left| \frac{(1-k)\,Gr\,Sc\,Pe_g}{1766} \right|, \quad Pe_g << 1 \tag{5.1}$$

and

$$\zeta = \left| \frac{(1-k)}{k} \frac{Gr\,Sc}{4} \frac{1}{Pe_g^{\,3}} \right|, \quad Pe_g >> 1 \tag{5.2}$$

where $Gr = g\,\beta\,(\Delta T/L)\,W^4 / \nu^2$ and $Pe_g = v_g\,W / D = 2\,a / \delta$.

Similar results were obtained in Section 2 and it was also show that the effect of a gradient that falls off exponentially can produce several times the radial segregation as a linear gradient with the same temperature difference. For maximum coupling between the flow field and the diffusion field, it was found that

$$\zeta = \frac{Gr\,Sc}{1428}(1-k), \quad k < 1 \tag{5.3}$$

and

$$\zeta = \frac{Gr\,Sc}{1654}\frac{(1-k)}{k}, \quad k > 1 \tag{5.4}$$

where here $Gr = g\,\beta\,\Delta T\,W^3 / \nu^2$.

Comparing this to Eq. (1.5), we see that the Langbein and Tiby model over-predicts the variation in solute redistribution by more than three orders of magnitude if their length scale is taken as the ampoule width.

Even so, it may be seen that achieving diffusion limited transport in growth from the melt will be difficult since the Gr Sc must be held to O(10). For a dilute system such as Se:GaAs, $\delta\rho/\rho = 0.0085$, $\nu = 0.003$ cm^2/sec, Sc = 30, and k = 0.1. If W = 1.5 cm, Gr = 3187 g and ζ = 67 g. If the radial segregation is to be held to < 1%, g < 0.15 micro-g. This can be reduced somewhat by detuning the experiment away from the conditions of maximum coupling (as may be seen by comparing this result to the estimates for Matthiesen's experiment in Table 4.1), but the range over which this is possible is limited by practical considerations. On one hand, one wants the v_g as large as possible to minimize the growth transient and to be able to grow as much as possible in the time available. However, increasing the growth rate increases radial segregation as long as P_g < 1. One could lower the sensitivity to radial segregation by increasing $Pe_g >> 1$ to get on the back side of the curve where $\zeta \sim Pe_g^{-3}$; however, this is constrained by thermal gradient if one wants to prevent interfacial breakdown from constitutional undercooling. Using Tiller's constitutional supercooling criteria, this constrains the growth Peclet number by

$$Pe_g = \frac{v_g W}{D} = \frac{W}{\delta} < \frac{W \nabla T}{m C_\infty}\frac{(1-k)}{k} = \frac{W(\Delta T/\lambda)}{m C_\infty}\frac{(1-k)}{k} \tag{5.5}$$

where m is the slope of the liquidus.

Attempting to increase the allowable growth rate by increasing the thermal gradient increases the driving force for segregation, causes difficulty in controlling the interface shape, and produces more thermal stress in the newly solidified materials which promotes defect formation. Better quality crystals can be obtained by increasing λ and lowering the growth rate, but this increases the time and ampoule length required to growth a reasonable amount of material under steady state growth conditions.

The situation is even more demanding for the non-dilute II-VI alloy systems which can have $Sc = O(10^3)$. Here the $\lambda = \delta$ since the density gradient is determined by the diffusion field. Extremely slow growth rates are required because of the small values of D that are characteristic of some of these systems. Again, to grow a reasonable amount of material in the time available, the thermal gradient must be adjusted so that $Pe_g = W/\delta = O(1)$. For $Pe_g = 1$, the segregation can be expressed as

$$\zeta \approx \frac{Gr\,Sc(1-k)}{3200}, \quad k < 1 \tag{5.6}$$

and

$$\zeta \approx \frac{Gr\,Sc}{1778}\frac{(k-1)}{k}, \quad k > 1. \tag{5.7}$$

For $\Delta\rho/\rho = 0.0956$, $Sc = 1333$, and $\nu = 0.008$ cm^2/sec, $k = 4.35$, and $W = 0.8$ cm; $Gr = 764$ g and $\zeta = 441$ g. Now to attain < 1% segregation, the residual acceleration along the transverse axis would have to be 23 nano-g's! Again some relief can be obtained by reducing the growth rate to lower the Pe_g as may be seen in Fig. 3.12. The Pe_g in Lehoczky's experiment was 0.547 which accounts for the lower value in Table 5.1. However, to be able to grow any appreciable amount of material in a reasonable length of time, even using a pre-profiled solute distribution, this growth rate is approaching the lower practical limit.

5.3 RECOMMENDATIONS

For future low gravity experiments, it would be desirable to obtain some relief to this very stringent requirement for limiting the transverse accelerations. If this requirement applied to crystals grown on earth by the vertical Bridgman process, it would be necessary to maintain the furnace axis to better than 27 nanoradians in order to avoid assymmetric radial segregation. Obviously, the vertical density gradient seeks the local vertical which eliminates the tangential component. In the absence of any axial acceleration, which was assumed here, there is no stabilizing axial gradient.

5.3.1 Density Gradient Stabilization

Therefore, one possibility for reducing this transverse acceleration requirement is to purposely add a stabilizing axial acceleration. This possibility was analyzed in Section 1.6 where it was shown that the effect of an axial acceleration was to alter the maximum convective by the factor $|Ra_c|/(|Ra_c|+Ra(x))$. If we define $Ra(x)$ as $g_x\,(\Delta\rho/\rho)\,W^4 / (\nu\ \kappa\ L)$, then $|Ra_c| = 500.56$. Now for dilute systems, the segregation is proportional to

$$\zeta \sim Gr\,Sc\left(\frac{500}{500+Ra(x)}\right) \sim Gr\,Sc\left(\frac{500}{500+(g_x/g_y)(W/\lambda)Gr\,Pr}\right). \qquad (5.8)$$

Since Gr is small in a microgravity experiment, it is obvious that there is little benefit to be gained by applying an axial acceleration to stabilize the flow for systems with low Pr. However, for non-dilute systems in which the density gradient is predominantly due to solutal effects, the Pr in the above equation is replaced by Sc. For a non-dilute systems with $k > 1$ the maximum radial segregation from transverse accelerations can be written from Eq. (5.6) as

$$\zeta \approx \frac{Gr\,Sc}{1778}\frac{(k-1)}{k}\left(\frac{500}{500+Ra(x)}\right) = \frac{Gr\,Sc}{1778}\frac{(k-1)}{k}\left(\frac{500}{500+(g_x/g_y)(W/\delta)Gr\,Sc}\right). \qquad (5.9)$$

The stabilizing effects of axial acceleration at different gravity levels for Lehoczky's experiment can be seen in Figure 5.1. If the furnace axis is oriented within $\pm 5°$ of the residual g-vector for accelerations $< 10^{-7}\ g_0$, the primary effect will be just the reduction of the transverse acceleration by $\sin\theta$. Increasing the acceleration above this value increases the segregation, but at a much slower rate due to the stabilizing effect of the axial gradient. It is interesting to note that by changing the geometry in such a way as to increase both the Gr and Ra, (e.g. by doubling the width of the ampoule, one can actually reduce the radial segregation caused by buoyancy-driven flows resulting from axial density gradients at the higher g-levels. However, as the axial acceleration is increased, flows driven by radial density gradients will also increase and possibly negate this effect.

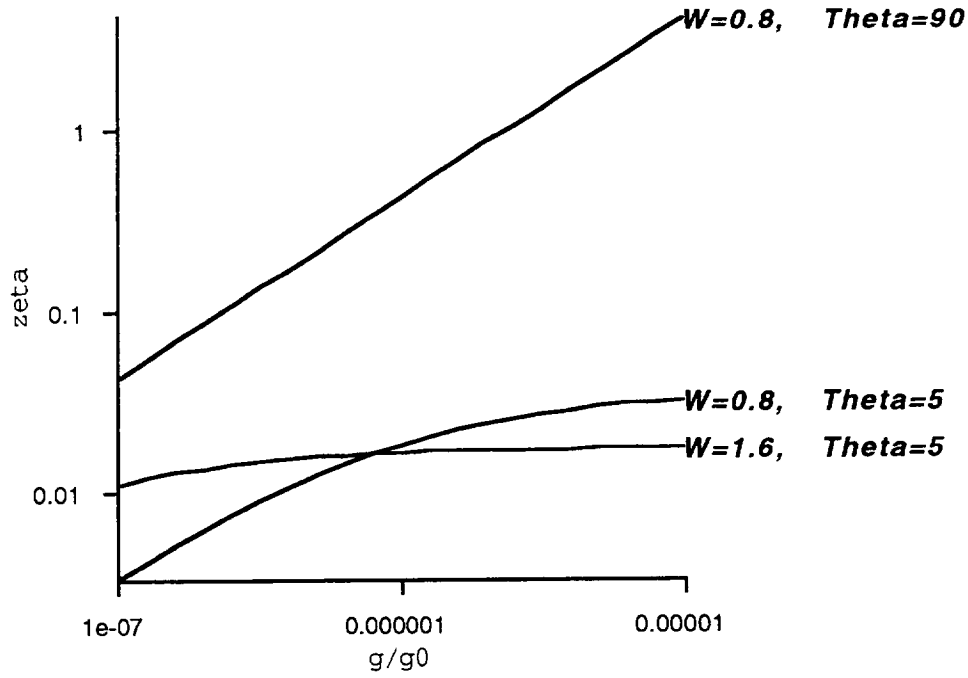

Fig. 5.1 Radial segregation (zeta) as a function of the magnitude of the residual acceleration vector for different orientations relative to the furnace axis (theta) and different ampoule widths (W). For W = 0.8 cm used in Lehoczky's experiment, orienting the furnace axis to within ± 5° of the residual acceleration produces approximately an order of magnitude reduction in segregation at 0.1 micro-g primarily because of the sin (theta) reduction of the transverse component of the acceleration. The reduction becomes more pronounced as the total acceleration is increased as the stabilizing effect of the axial gradient becomes more important; however, the segregation continues to increase with increasing rate, although at a lessor rate. Doubling the width of the ampoule increases both the Gr and the Ra which makes the stabilizing effect of the density gradient more effective at a lower acceleration and can actually result in less segregation as can be seen by the cross-over of the two curves at ~ 1 micro-g.

5.3.2 Magnetic Stabilization

The other possible way to stabilize such a system is the application of magnetic fields. This is illustrated in Fig. 5.2 which shows the maximum flow velocity in a vertical cell with width W and height 2 W with differentially heated side walls in unit gravity and in microgravity. The ΔT was taken as 10° C to roughly represent the radial gradient in a typical semiconductor melt using the vertical Bridgman system. The dotted diagonal lines represent Re = 2000, above which unsteady or turbulent flow develops; $Pe_{Thermal} = 1$, which marks the division between conductive and convective dominated heat transfer, and $Pe_{solutal} = 1$, which marks the division between conductive and convective dominated mass transfer.

The horizontal branches are the results of the application of a vertical magnetic field of strength B (Tesla) to a melt whose conductivity is σ (Siemens or mho/m). The value $\sigma B^2 = 3.6 \times 10^6$ represents an approximate upper limit to magnetic stabilization ($\sigma = 10^5$ S, B = 6 T) of semiconductor melts. With this amount of damping it is possible to avoid unsteady flows in even the largest melts in unit gravity and maintain conductive heat transfer, but convective mass transfer will still predominate unless the width is reduced to micron dimensions.

In microgravity, the magnetic damping is much more effective due to the lower driving force. However, it may be seen that for melts with $\sigma = O(10^5$ S), a field of > 0.1 T (1 KG) would be required to obtain a significant reduction in flows for widths = O(1 cm).

It was shown in Chapter 1.7 that if a strong magnetic field applied along the axis of a horizontal slot, the maximum flow along the walls was given by

$$\hat{u}_{mag} = \frac{Gr(W/L)}{6\sqrt{3}\ Ha^2}\left(\frac{L}{W}\right)^2 \frac{\nu}{W}, \qquad Ha >> 1. \tag{5.10}$$

The ratio of this to the maximum velocity in a horizontal slot with a gradient $\Delta T/L$ is

$$\frac{\hat{u}_{mag}}{\hat{u}} \approx \frac{12}{Ha^2}\left(\frac{L}{W}\right)^2; \quad Ha >> 1. \tag{5.11}$$

From this, it may be seen that to obtain a given reduction in flow from magnetic damping, the Ha ~ L/W. The reason for this behavior may be understood by examining Fig. 1.23. Since the field inhibits flow in the transverse direction, the flow field adjusts itself so that the transverse flow is spread as much as possible throughout the ampoule to minimize the transverse velocity. Thus lengthening the ampoule gives the flow more room to adjust and allows a higher maximum axial flow velocity. This does have an added beneficial effect in that the

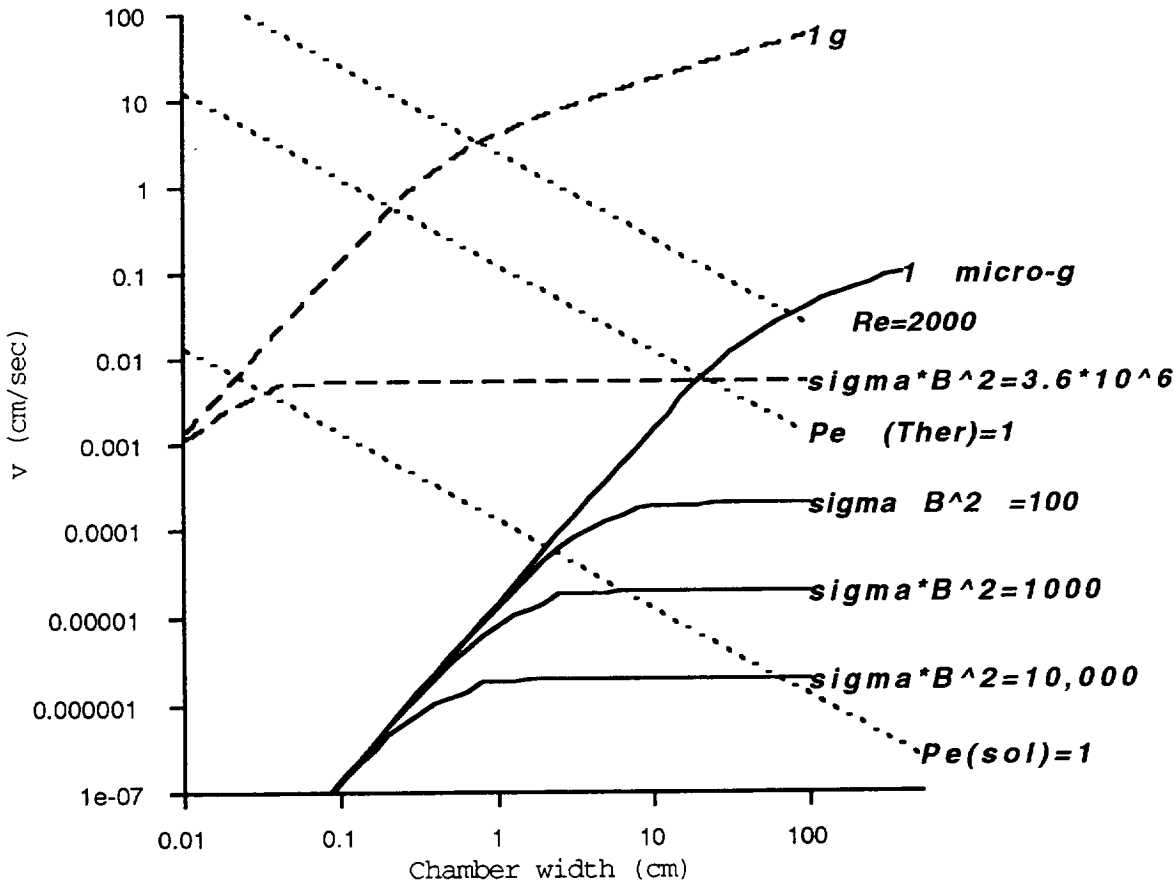

Fig. 5.2 Map of maximum velocity in a vertical chamber with a 2:1 aspect ratio and differentially heated side walls. The Pr is taken to be 0.01, ν = 0.0013 cm^2/sec, $\beta \Delta T = 2.5 \times 10^{-3}$. Also shown are lines representing Re = 2000, above which flow is expected to be turbulent; Pe(Ther) = 1, which marks the division between conductive and convective heat transport; and Pe(sol) = 1, which marks the division between diffusive and convective mass transport for Sc = 10. Horizontal lines indicate the velocity of a fluid with conductivity σ (Siemens) in the presence of a vertical magnetic field B (Tesla).

maximum axial flow is moved further from the growth interface, thus reducing the coupling between the flow field and the concentration gradient which will result in less solute redistribution.

Scaling from Table 5.1, we see that in order to attain $\zeta = 0.01$ in Lehoczky's experiment with 1 micro-g transverse acceleration, a reduction of 20 in Gr will be required. Using Eq. 5.11 to obtain a rough estimate of the required Ha, we find that Ha = 15.5 L/W. For L/W =5, $\rho = 5000$ Kg/m^3, $\nu = 8 \times 10^{-7}$ m^2/sec, a = 0.004 m, the σB^2 product would have to be 6×10^4 (L/W)^2 m.k.s. units. Estimating the conductivity of the melt to be 10^5 S, the required B is 0.775 (L/W)T or 38.75 KG. This may be an over-estimate because it assumes a linear gradient over the length of the melt and does not account for the reduced coupling between the flow field and the composition gradient near the interface. Therefore, a more detailed calculation is required to give a more definitive estimate. However, it seems clear that a very large magnetic field will be needed, probably requiring a superconducting magnet.

If the orientation of the transverse acceleration is known *a priori*, it may be possible to reduce the requirement on B by the ratio (L/W) by using as transverse magnetic field with B oriented perpendicularly to the acceleration vector since it is only necessary to control the flow in one plane. However, as may be seen in Fig. 1.26, this has the result holding the axial flow close to the walls of the ampoule until the region near the growth interface. Thus, some of the advantage may be lost by the increased coupling between the flow field and the composition gradient.

Magnetic damping coupled with microgravity would appear to have great promise in being able to extend diffusion control of less demanding (lower Sc) systems to larger diameters since Ha ~ width and the convective velocity becomes insensitive to size scale for Ha >> 1. The segregation behavior of a system whose density gradient falls exponentially in an axial magnetic field needs to analyzed in more detail such as was done in Section 3 in order to asses the effects of the reduced coupling between the flow field and the composition gradient.

5.4 CONCLUSIONS

Approximate analytical models for the flow fields in various geometries have been developed and verified against computational results. These allow the accurate prediction of velocities in a wide variety of microgravity experiments as well as in ground based experiments as long as the Reynolds numbers are low enough so that inertial terms can be neglected. Perturbation models for solute redistribution in Bridgman melt growth systems have been coupled to these flow models which allow the prediction of radial segregation due to axial as well as transverse accelerations. Again these have been verified by testing against computational results.

Unfortunately, experimental difficulties with the various crystal growth experiments using the Bridgman-type Crystal Growth Furnace (CF) did not allow a definitive experimental test of these models, but it was obvious that these experiments were affected by the unexpected transverse acceleration that ranged between 0.5 and 1 micro-g.

The ability to achieve diffusion controlled solute redistribution in non-dilute systems with large Sc remains a formidable challenge, even in a microgravity environment. Efforts to align the furnace axis with the local acceleration vector certainly help in reducing the transverse component of the acceleration, but effects such as diurnal variations in the atmosphere as well as uncontrolled leaks and vents place practical limitations on how well this may be accomplished. Density gradient stabilization the application of magnetic fields may help overcome this problem, but more research will be required to determine their effectiveness.

5.5 REFERENCES

1. I. Alexander, Passive Accelerometer System: Measurements on STS-50 (USML-1), Joint L+1 Year Science Review of USML-1 and USMP-1 with the Microgravity Measurement Group, NASA Conf. Publ. 3272 (MAY1994) 569-582
2. R. Blanchard, Preliminary OARE Absolute Acceleration Measurements on STS-50, ibid. 103-129
3. S. Lehoczky, Crystal Growth of Selected II-VI Semiconducting Alloys by Directional Solidification, ibid, 163-222
4. D. Larson, Orbital Processing of High Quality CdTe Compound Semiconductors, ibid. 129-162
5. D. Matthiesen, The Study of Dopant Segregation Behavior During the Growth of GaAs in Microgravity, ibid, 223-264
6. R. Naumann, Marangoni Convection in Closed Containers, ibid, 601-608
7. S. Ostrach, Surface Tension Driven Convection Experiment (STDCE), ibid, 271-300
8. R. Kroes, Nucleation of Crystals from Solution in Microgravity, ibid, 663-672
9. J. Marshall, Particle Dispersion Experiment(PDE): Preliminary Results from the USML-1 Glovebox, ibid, 717-732
10. J. P. Garandet, J. Crystal Growth, 125 (1992) 112-120

6.0 ACKNOWLEDGMENT

The author gratefully acknowledges the help of Dr. Glen Roberts of Roberts Associates, Arlington, VA who provided some of the numerical computations quoted in this work.